Combustion synthesis of tin dioxide nanocomposites for gas sensing applications

by

Smitesh Dhirajlal Bakrania

A dissertation submitted in partial fulfillment
of the requirements for the degree of
Doctor of Philosophy
(Mechanical Engineering)
in The University of Michigan
2008

Doctoral Committee:

Professor Margaret S. Wooldridge, Chair
Professor H. Scott Fogler
Professor Jyotirmoy Mazumder
Professor Ann Marie Sastry

To my wife Lopa.

ACKNOWLEDGEMENTS

My foremost appreciation goes to Professor Margaret Wooldridge for providing the invaluable guidance and support for this project. Her contagiously positive nature and critical insights made this journey a tremendously rewarding endeavor. I know I will be graduating with a lot more than what is documented in this dissertation.

I would also like to thank the rest of the dissertation committee members: Professor Fogler, Professor Mazumder and Professor Sastry, for serving the important role of providing useful feedback.

The financial support from the NSF grant for the sensor project is much appreciated, along with a number of Rackham and Combustion Institute travel grants that funded trips to conferences.

I am very grateful for endless inputs from my colleagues; few of whom I would like to acknowledge individually (in no particular order): Linda Chow, from Prof. Kurabayashi's group, for her advice on the microfabrication of the sensor platform; James Wiswall for all the very insightful conversations and taking the first plunge into LaTeX- which made writing this document less stressful; Stephen Walton for his technical inputs at various stages of my research; Bradley Zigler for bringing a very mature perspective to any situation; Carlos Perez for his help with the PIV and thermocouple measurements that were used in this study; Gurlovleen Rathore for her contributions to the gold acetate decomposition experiments; Dmitris Assanis and Travis Palmer for assisting in building components of the combustion synthesis and

gas sensor testing facilities; Paul Teini for being an excellent office mate and providing rewarding diversions; Tiffany Miller for the initial guidance on the combustion synthesis project and collaboration in writing a number of journal and conference papers; Melissa Chernovsky and Xin He for sharing their experiences and for having a positive work ethic.

There are numerous staff members who have provided much needed assistance along the way. These are: Carl Handerson from central campus EMAL; Staff members at the University of Michigan microfabrication facility; Steve Emanuel at the graduate student machine shop; Harold Eberhart for the glass-based apparatus related help and Dr. Antek Wong-Foy for the help with the thermogravimetric study.

My thanks also go to my family whose support throughout my education has been invaluable. I am also fortunate to have a family-in-law who is equally supportive. And finally, the next most significant contributor to my success, my wife Lopa, whose unfaltering dedication to her own thesis in organic chemistry kept me motivated. Her zeal for success is truly inspiring.

TABLE OF CONTENTS

LIST OF FIGURES

Figure

LIST OF TABLES

Table

LIST OF APPENDICES

Appendix

ABSTRACT

Combustion synthesis of tin dioxide nanocomposites for gas sensing applications

by

Smitesh Dhirajlal Bakrania

Chair: Margaret S. Wooldridge

The current work focuses on understanding the mechanisms controlling tin dioxide (SnO_2) nanoparticle morphology in combustion synthesis systems and how nanoarchitecture affects performance of solid-state gas sensors. A range of analytical methods (including transmission and scanning electron microscopy, x-ray diffraction, nitrogen absorption, and XEDS) were used to characterize the materials properties as a function of the combustion synthesis conditions. A novel method of generating tin dioxide materials was developed which provides a new degree of control over SnO_2 morphology; including spherical, nanorod and encapsulated particle architectures. A simplified model for particle formation based on characteristic times was developed to identify the physical and chemical processes affecting the morphologies observed using transmission electron microscope imaging. The SnO_2 nanoparticles evolve from primary particles sizes of 7 nm to 14 nm through the synthesis region, and the results indicate interparticle collision and sintering are the dominant mechanisms in determining particle size and morphology for the flame conditions studied.

Metal acetates were used to create metal/SnO_2 nanocomposite materials, and the processes controlling gold acetate decomposition in particular were explored. The results of the studies suggest a relationship between the precursor crystallite size and the product nanoparticles.

The well-characterized SnO_2 particles were evaluated as the active materials for gas-sensing. Sensor sensitivity and time response to carbon monoxide in dry air was used to investigate microstructure-performance links. Excellent sensitivity (3 7, based on the ratio of the resistance of the sensor in air to the resistance in the target gas) and time response (4 - 20 seconds) were demonstrated for the thin film gas sensors. Fabrication studies demonstrated the sensor performance was a strong function of the film deposition method. A novel method for manufacturing sensors with outstanding consistency and performance was developed. This method was used to explore the effects of microstructure and composition on sensor performance. Gold and palladium doped SnO_2 gas sensors indicated the introduction of dopants has potential to improve sensor performance; however, the effects are dependent on the additive distribution and location. The combustion synthesis and sensor fabrication methods that are the results of these studies will dramatically accelerate the design of new sensors and sensor optimization.

CHAPTER I

Introduction

Tin dioxide (SnO_2) is an important semi-conducting material with primary applications driven by its excellent optical and catalytic properties. SnO_2 belongs to a group of oxides that exhibit low electrical resistance with high optical transparency. SnO_2 has been used in glass coatings to produce low emissivity windows due to the transmission efficiencies for visible wavelengths, high mechanical hardness and good environmental stability [1]. Dye sensitized solar cells utilize nanosized tin dioxide particles as transparent conducting electrodes [2]. Tin dioxide coatings have also been used in optoelectronic devices [3].

However, gas detection is currently the most important application for tin dioxide. It was first proposed to be used as a gas sensing material in 1962 [4] and now it is widely used as a solid-state gas sensing material for detecting toxic and hazardous chemicals for domestic and industrial safety. The majority of carbon monoxide (CO) sensors that are commercially available utilize tin dioxide as the active sensing material. SnO_2 gas sensors with detectivity limits as low as a few parts-per-million (ppm) have been demonstrated [5, 6, 7]. Due to the sensitivity to combustible gases SnO_2 has potential for use in monitoring and detecting hydrogen over a wide range of conditions that may be required to establish a safe and effective infrastructure

for a future hydrogen economy [8]. Sensitivity to a wide range of chemicals makes SnO_2 gas sensors ideal for monitoring biological processes such as ripeness of fruits by monitoring ethylene [9], electronic nose application for food quality control [10] or diagnosis of illness through breath analysis [9, 11, 12]. With such wide ranging application as a chemical and gas sensing material, there is tremendous impetus to improve the properties of tin dioxide to further increase device performance and versatility. The next section provides some background on gas sensing and the limitations of tin dioxide gas sensors.

1.1 Gas sensing

There are various other methods for detecting gaseous species such as gas chromatography, Fourier-transform infrared spectroscopy, chemiluminescence detectors, mass spectrometers and others that may provide better sensing capabilities compared to semiconductor gas sensors. However, because semiconductor gas sensors do not require optics and sophisticated detectors they have an advantage over these detection techniques in terms of cost, mobility, size, reliability, durability, and power consumption. Other gas sensing semiconductors include ZnO, ZrO_2, WO_3, MoO_3, TiO_2, In_2O_3 and Fe_2O_3, to name a few. Of these materials, ZrO_2 is exclusively used as the oxygen sensing material in automotive engines for monitoring air to fuel ratio; commonly known as the lambda sensor. ZnO and SnO_2 are primarily developed and available as CO or hydrocarbon sensors. Both tin and zinc oxide display bulk electrical resistance changes in response to gases present in the environment. On the other hand, ZrO_2 depends on potentiometric response (e.m.f) of the material to the gases.

Tin dioxide (also called stannic or tin oxide) gas sensors typically come in three varieties that are distinguished by the characteristic dimensions of the active sensor material. For porous plug and sintered block sensors (Fig. 1.1), the SnO_2 layer is on the order of a few millimeters in thickness, while the SnO_2 layer in film sensors is typically in the nanometer to micron range [13]. Thin films span approximately 50 nm to 2 μm in film height, and thick films span approximately 2-10 μm. All tin dioxide gas sensors incorporate a heater to maintain the active material at a fixed operating temperature. Film sensors are often deposited on an aluminum oxide (alumina, Al_2O_3) ceramic substrate with gold or platinum interdigitated electrodes and heating serpentines printed on either side. The active sensing component is typically placed inside a sensor housing with a meshed opening.

1.1.1 Sensing performance

Generally gas-sensing performance can be defined based on four criteria: sensitivity, selectivity, stability and time response. Sensitivity is typically defined as the ratio of the resistance of the sensing element in air to that in the target gas, i.e. $S = R_a/R_g$. Sensitivity may also be defined using conductance measurements, i.e. $S = (G - G_o)/G_o$ where G is the conductance in the presence of the target gas while G_o is the conductance in air. Selectivity relates to the specificity of the gas sensor response to a target gas in the presence of a mixture of gases, hence playing a major role in gas identification. Stability is often given limited attention however the success of a sensor will be limited if the sensor performance is not demonstrated as repeatable and stable over long-term testing. Time response is another crucial criterion in determining the effectiveness of the sensor. Even with these four performance criteria that can be used to evaluate sensor response, absolute comparison of sensor

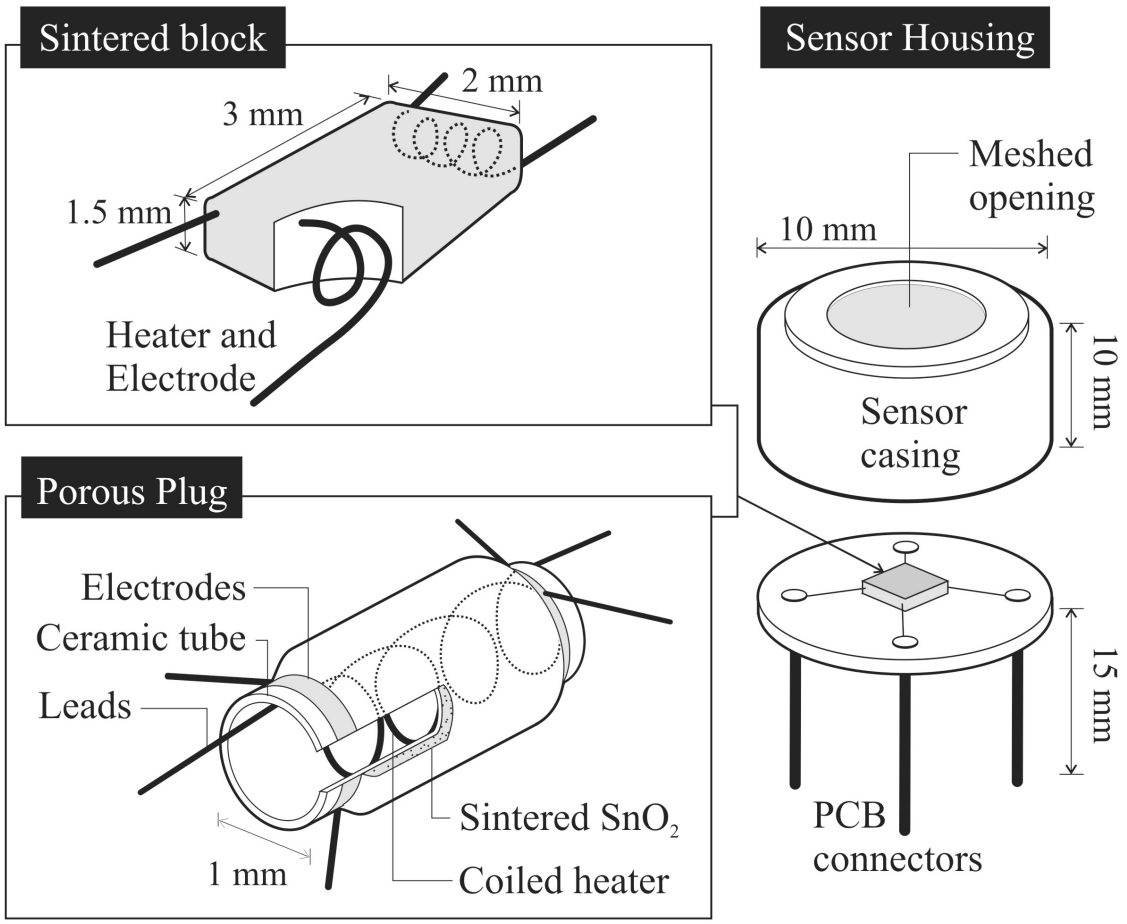

Figure 1.1: Schematics indicating sintered block sensor design (top left) and porous plug sensor design (bottom left) with sensor housing on the right. Typical dimensions are provided in the diagrams.

performances between different sensors is still challenging. Particularly because the criteria depend on testing conditions such as the particular target gas, concentration level, moisture level, and operating temperature. As a result there are other sensor characterization criteria suggested, such as analytical sensitivity that accounts for gas concentration with the corresponding sensitivity and reproducibility that more accurately compares individual sensors [14].

1.1.2 Sensing mechanism

The sensing mechanism for tin dioxide is a surface phenomenon where a slightly non-stoichiometric surface provides sites for chemisorption of oxygen at temperatures above 100 ^oC [15]. The electrons near the surface regions are transferred to the chemisorbed oxygen producing an electron-depleted region with low conductivity, also known as the space-charge layer or the depletion layer. Once the depletion layer is formed, an introduction of a reducing gas such as CO causes an oxidation reaction at the surface of tin dioxide to produce CO_2 releasing the electrons back to the SnO_2 particle leading to lowering of resistance. A reverse effect takes place in the presence of oxidizing gas such as NO_2, where the oxygen is chemisorbed on the surface yeilding NO causing increase in resistance. Figure 1.2 presents a schematic of the adsorption and the desorption processes that produce the sensing response. SnO_2 gas sensors have been successfully demonstrated for a host of gases such as H_2, H_2S, CO, NO, NO_2, etc and hydrocarbon compounds such as alkanols, alkanes, alkenes, and other volatile organic compounds (VOCs) [16].

1.1.3 Sensor microstructure properties

The sensor response depends largely on the microstructural and electrochemical properties of the material. Therefore a tremendous effort is made to understand the dependency and as a result improve sensing performance [16]. Pioneering work by Yamazoe et al. [17] has suggested that the two most effective methods for enhancing performance of SnO_2 gas sensors are reduction in primary particle sizes and/or introduction of metal dopants.

The sensitivity of a gas sensor, for instance, is highly dependent on the character-

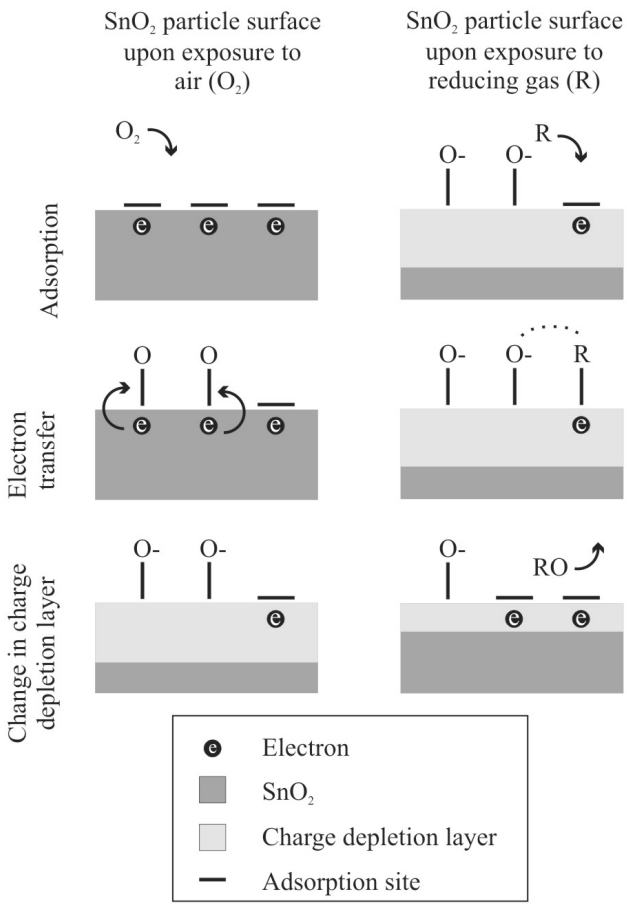

Figure 1.2: Schematic showing the adsorption and the desorption processes that lead to sensing on the SnO_2 surface. R represents a reducing gas.

istic particle size. Since the sensitivity is primarily due to the surface phenomenon described earlier, a change in the particle size influences the depth of influence of the depletion later. The depth of the electron depletion layer formed near the surface of the particles can be defined by Debye length, L_D [18]:

$$L_D = \left(\frac{kT\epsilon}{q^2 n}\right)^{\frac{1}{2}} \tag{1.1}$$

which depends on the dielectric constant (ϵ), temperature (T) and the carrier charge concentration (n) of tin dioxide. k and q are the Boltzmann constant and the electron charge, respectively. With these parameters constant, as the particle

diameter decreases there is a diameter at which the depletion layer engulfs the entire volume of the particle. The resulting depletion layer would have a significant change in resistance as a function of the target gases which is desirable for improving sensor sensitivity. This effect can greatly affect the neck regions between two particles even if the depletion layer does not affect whole primary particles. Yamozoe et al. [17] has shown that there is dramatic improvement in sensitivity at particle diameters less than 6 nm. Under these conditions the sensor sensitivity is also a strong function of size of the necks between particles (see [16] for detailed discussion).

Additives can have several effects on the SnO_2 properties important to gas sensing applications, including inhibiting SnO_2 grain growth, modifying the electron Debye length and modifying the gas-surface interactions via electronic and catalytic mechanisms. Metals such as Ni, Pd, Pt, Cu, Au, Mo, Sb, In, Al have been shown to improve sensor response when incorporated in SnO_2 [19, 20, 21, 22, 23]. Figure 1.3 shows the general steps involved with the electronic and catalytic mechanisms during the chemisorption of target gases. In the electronic mechanism (left column of Fig. 1.3) the target gas reacts with chemisorbed oxygen on the additive surface, releasing the electrons to the additive which are eventually transferred to the depletion layer. In the catalytic mechanism (right column of Fig. 1.3), the target gas reacts with chemisorbed oxygen on the SnO_2 surface releasing the electrons to the depletion layer directly. Metal and metal oxide additives to tin dioxide have received considerable attention for improving sensing performance of gas sensors due to suggested changes in the material sensing mechanisms. Table 1.1 provides several examples of metal doped gas sensors which demonstrated enhanced sensing behavior. The table also provides the associated crystallite sizes, where available.

The sensing performance depends on various other microstructural properties that

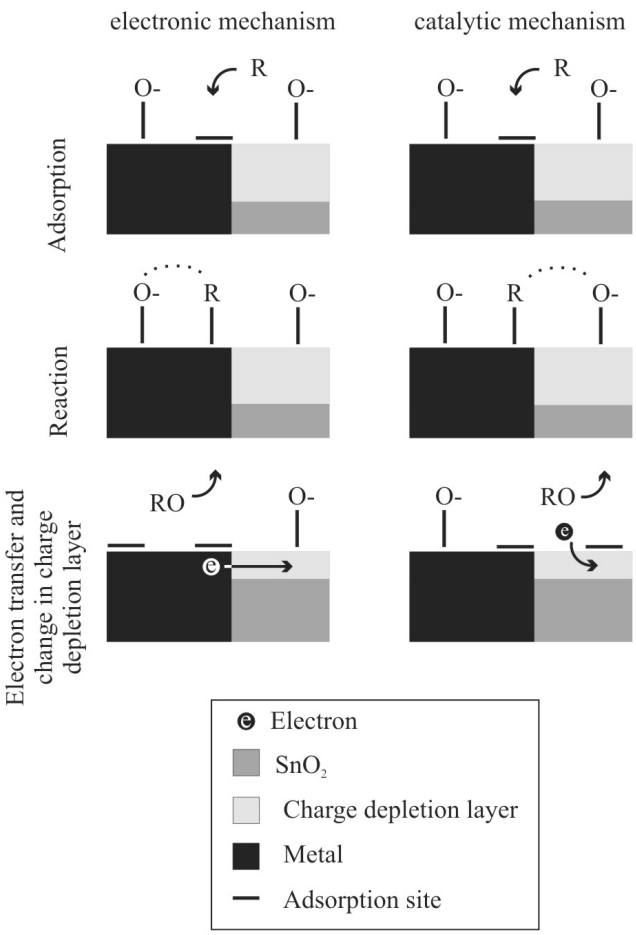

Figure 1.3: Schematic indicating the general steps involved in the electronic and catalytic mechanisms active in SnO_2 sensors with metal additives. R represents a reducing gas.

can have secondary effects, if not direct effects. For instance, the porosity of the sensing film can limit diffusion of the target gases, and therefore limit the time response of the sensor. Connectivity or necking can significantly affect the conductivity as discussed above. The interface between the active material and the sensing electrodes forming the three phase boundary (TPB) is a crucial interface which may play a primary or a secondary role in sensing. Thus, the understanding of the electrode material and the connectivity with the active film is important. Morphology of the particles can also influence the active surface area available for chemisorption as well as the interaction with the depletion layer. As a result, several researchers

have explored lower dimensional morphologies of tin dioxide [24, 25, 26, 27]. Figure 1.4 shows a schematic of a cross section of a thin film sensor with embedded inter-digitated electrodes to illustrate some of the critical parameters that dictate sensing response.

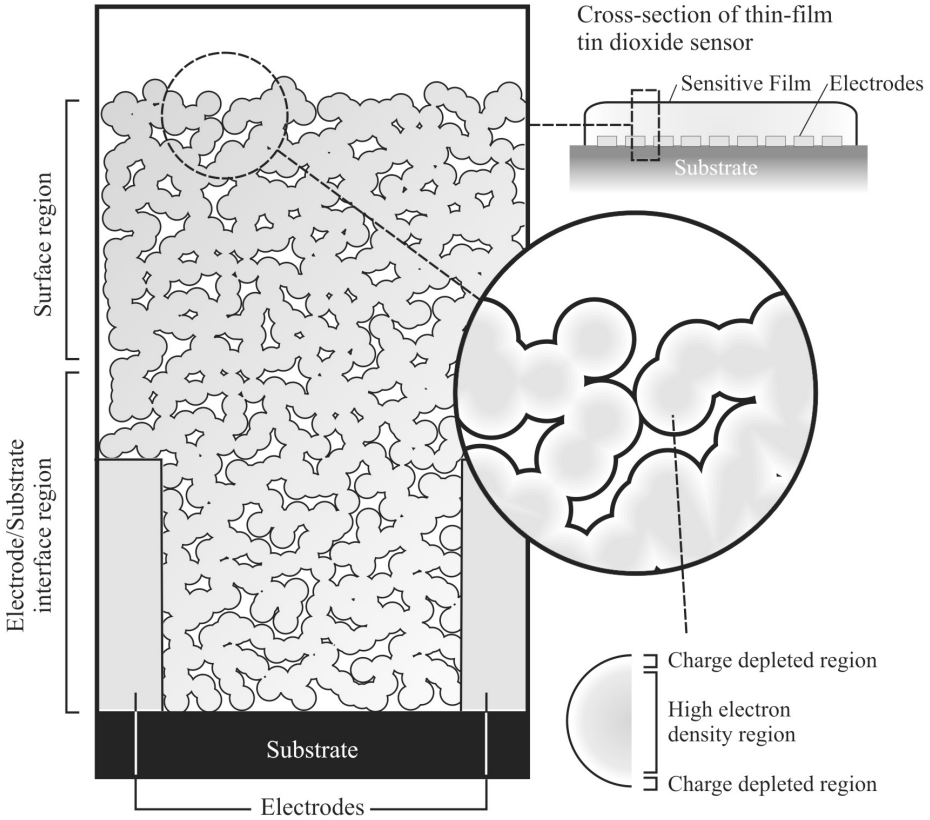

Figure 1.4: Schematic of cross section of a thin film sensor illustrating the critical microstructural properties that govern sensing behavior

Empirical studies have long been the basis for development of improved stannic oxide sensor performance. There is no single theory that provides a clear road map to enhance sensor response and this is largely due to the complex interaction between microstructural and electrochemical properties of the material. For example,

- Often a single improvement will affect multiple performance criteria because they are inter-related. For instance, improving sensitivity may also reduce time

Table 1.1: SnO_2 film sensor synthesis methods and corresponding sensor performance for metal doped systems.

Film type (thickness)	Fabrication	SnO_2 synthesis	SnO_2 cryst. size	SnO_2 additive	Sensor performance (sensitivity[a], selectivity, and stability; where provided)	Time response	Ref.
Thick (N/A)	Screen printing	Wet method* (Co-precipitation)	9 nm	Au, Pd	0.6 at 400 ^oC, 1000ppm CH_4 Qualitative selectivity data	N/A	[22]
Thick (20-25 μm)	Screen printing	Commercial powder	N/A	Pt	800 at 300^{o}C, 1000ppm C_2H_5OH Selectivity number provided	8 s	[19]
Thick (20-25 μm)	RF magnetron sputtering	Commercial powder	N/A	Pt	100 at 300 ^oC, 1000 ppm C_2H_5OH[b]	12 s	[19]
Thick (20-25 μm)	DC-sputtering	Commercial powder	N/A	Ag, Ti	80 at 300 ^oC, 1000 ppm C_2H_5OH[b]	7-15 s	[19]
Thick (250 μm)	Screen Printing	Commercial paste	N/A	Pd	3.5 at 470 ^oC, 1000 ppm CH_4 Qualitative selectivity data	N/A	[28]
Thick (N/A)	Screen printing	Commercial paste	30 nm	Rh	3.5 at 500 ^oC, 1% CH_4	N/A	[29]
Thick (N/A)	Screen printing	Commercial paste	60 nm	Pt	800 at 300 ^oC, 1000 ppm C_2H_5OH	15 s	[9]
Thin (1.5 μm)	Gas-deposition and energetic cluster impact	Gas-phase oxidation (SnO precursor used)	14 nm	None	3.5 at 300 ^oC, 1000 ppm C_2H_5OH	10 s	[15]
Thin (100 nm)	Spin-coating	Commercial colloidal dispersion	10 nm	None	0.08 $k\Omega^{-1}$ at 350 ^oC, 1 ppm CH_3OH (sensor conductance) Stability shown for 120 h	N/A	[30]
Thin (1 μm)	Spin-coating	Wet gel*	6 nm	None	1100 at 350 ^oC, 800 ppm CO	20 s	[31]
Thin (300 nm)	Spin-coating	Hydrothermal treatment*	6 nm	None	400 at 350 ^oC, 800 ppm H_2	N/A	[32]
Thin (300 nm)	Spin-coating	Mechanochemical reaction	24 nm	None	5 at 300 ^oC, 1000 ppm O_2	120-180 s	[33]
Thin (500 nm)	Ion beam sputtering	Precipitation	11 nm	Ca	1.3 at 400 ^oC,4000 ppm CH_4 Stability shown for 90 days	N/A	[34]
Thin (200 nm)	Reactive DC sputtering	No info.	12 nm	Pt, Pd	5.25 at 325 ^oC, 100 ppm of CO[b] Stability shown for 75 days Qualitative selectivity data	5 s	[35]
Thin (120 nm)	RF diode sputtering	Commercial tin target	N/A	CuO	7443 at 150 ^oC, 20ppm H_2S Stability shown for 1000 s	14 s	[36]
Thin (380 nm)	Pulsed laser ablation	N/A	20-60 nm	Au, Pd, Pt	1.2 at 400 ^oC, 30 ppm of CO[b] Stability shown for 200 h	10 s	[20]

* $SnCl_4$ used as the SnO_2 precursor

[a] Sensitivity given as the resistance ratio, $S = R_a/R_g$, at specified operating temperature and mole fraction of target gas

[b] Sensitivity given as a conductance measurement, where $S = (G - G_o)/G_o$.

response or reducing particle sizes may improve sensitivity but increase the sintering rates for particles to fuse together and therefore deteriorates the long term stability

- Multiple interdependent sensing variables are involved, and therefore altering one property will influence others and hence make it difficult to interpret the results. For example, doping may also result in a decrease in SnO_2 particle size, therefore introducing ambiguity in the catalytic activity of the dopant.

As a result of the convolved system responses, a clear understanding of microstructure-performance links is lacking, though general trends continue to guide research. To achieve better understanding there is a need to carefully characterize the sensing material, while evaluating the corresponding sensing response. This will, in turn, yield better sensors models and assist theoretical development of the sensing mechanism.

1.1.4 Material and microstructural characterization

A variety of analytical techniques have been used to study particles and film properties, which can be used to link microstructure to performance and lead to better design and optimization of SnO_2 sensors. Table 1.2 provides a summary of analytical techniques used for material characterizations with specific requirements for sample preparation and sample mass. Additionally, specific surface area analysis (N_2 adsorption isotherms using BET theory) for evaluating specific surface area of the film, porosity and estimated grain sizes can provide a valuable insight.

Electrochemical information of the microstructure can either be inferred from the characterization described above or directly via spectroscopic analysis. Other techniques such as Mossbauer spectroscopy, Fourier transform IR spectroscopy, and

Table 1.2: Summary of commonly used analytical methods for gas sensing material characterization

Method	Applications	Sample preparation and form	Sample mass	Specimen area/volume considered
Scanning Electron Microscopy (SEM)	Morphology, Particle size (μm range), Critical dimensions (film thickness)	Sample size: $\leq$ 6 inch (2 inch tall). Powders held with copper or carbon tape (particles >1 μm), otherwise make paste using solvent. Non-conducting samples need sputtered metal layer. Sample may require, grinding and polishing.	50 mg	Resolution: 5-10 nm (material dependent)
Transmission Electron Microscopy (TEM)	Morphology, Particle size in nm range, Crystallinity through Selected Area Electron Diffraction (SAED)	Aerosolized or alcohol-dispersed powders deposited on 3 mm grid. Ground and ion-milled <100 nm thick substrates	<1 mg	Resolution: <1 nm (material dependent). Requires crystalline particles/films <100 nm
X-Ray Energy Dispersive Spectroscopy (XEDS)	Elemental speciation, Percent composition	Same as TEM and SEM requirements because XEDS systems compliment electron microscopy		SEM probe depth: $\sim$ 200 nm. Area depends on beam size, e.g. < 50 nm for TEM
X-Ray Diffraction (XRD)	Phase identification, Purity/quality control of materials, Orientation of single crystals, Particle size determination	Paste prepared from powder and IPA on glass slide, 1 in x 1 in substrate, <1 mm thick film	0.5-0.1 g	Depends on the material. Approx. probing depth is <0.2μm (200 nm)
X-Ray Photoelectron Spectroscopy (XPS)	Elemental, chemical state analysis, depth profiling and imaging.	Sample diameter $\sim$1 cm and <2 mm thick. Alternatively: 8 x 15 mm and <10 mm thick. Powder samples must be compacted into a pellet, pressed against soft indium metal or secured to a holder	200 mg	Analysis: 1-2 mm or 300-700 μm. Imaging: 200-900 μm^2. Depth: 95% of signal comes from the top $\sim$6 nm of surface (Highly dependent on material).
Electron Microprobe Analyzer (EMPA)	Elemental speciation	Similar to SEM, but powders must be compressed into pellets (flatness is required). Up to 1.5 inch in size	1 g	1-5 μm diameter. Probing depth is sample dependent.

electron energy loss spectroscopy (EELS) have also been used in gas sensing research. Batzill and Diebold [3] provide an excellent review of material analysis of tin dioxide in their recent article on surface characterization of SnO_2.

1.2 Combustion synthesis

Particles formed or burned in flames have been employed in a vast range of systems: as metal propellants for rockets, as pulverized coal or solid waste for power generation and as carbonaceous soot to promote radiation heat transfer in industrial furnaces. Such applications belong to the realm of combustion engineering where the particles augment the combustion. Combustion synthesis (CS), on the other hand, uses combustion to generate particles that are utilized elsewhere. Commercially, these particles are typically used as pigments or fillers in cosmetics, plastics, paints and tires, with further applications on the horizon.

Combustion synthesis has proved to be a versatile production technique for metal oxides and carbon-based particles such as SiO_2, TiO_2, Al_2O_3 and carbon black. With annual production volumes of several million metric tons and typical production rates of the order of 100 metric tons per day [37], combustion synthesis is a key technology for generation of particles. Recent developments have expanded the scope of combustion synthesis to the generation of metal nanoparticles [38], nanocomposites [39] and one-dimensional structures [40] - focusing on the morphology and size as well as the material itself. This renewed interest is attributed to the progress made in discovery of functional nanomaterials for catalysis, electronics, medical imaging, drug targeting and sensing [16, 41].

Combustion synthesis provides a single step solvent-free process to achieve nanopar-

ticles. Other advantages to combustion synthesis include: it is a continuous process as opposed to a batch-process, high purity and temperatures allow better control over crystal state/morphology and the process is intrinsically scalable [42]. There are many control variables that can be altered to achieve control over particle structure. However, it is often challenging because the synthesis occurs within a fraction of a second. Various studies have demonstrated achieving tailored nanoparticle properties by changing the complex processes taking place in the flame, such as by changing: differential velocities of the fuel/precursor and oxidizer streams [43], flame temperature via diluents [44], flame structure [45, 46], fuel-oxydizer ratio [47, 48], precursor concentration and type [44, 49, 50], external electric fields [51], etc. Recent developments in experimental and theoretical studies of combustion synthesis systems are provided in the reviews by Pratsinis [52], Rosner [42], Kammler et al. [37], Gutsch [53] and Wooldridge [54].

1.2.1 SnO_2 synthesis

A variety of techniques have been employed in literature to generate nanocomposite SnO_2 materials for gas sensing purposes such as, sol-gel processing, chemical vapor deposition (CVD), wet chemical deposition, sputtering methods, gas-phase condensation, pulsed laser ablation and mechanochemical processing, as evident from Table 1.1. Sol-gel processing is a popular method used for generating SnO_2 powers for research-based gas sensors due to the limited tools required for synthesis and high quality materials that can be produced [55, 56]. One of the disadvantages to using sol-gel chemistry is the contamination from chlorine due to the use of $SnCl_4$ as a tin precursor. Processes such as CVD and pulsed laser ablation can generate particles with unique microstructures however these are techniques that require vacuum cham-

bers and high power that may be sufficient for research purposes but are limiting for large scale production.

Combustion synthesis of tin dioxide has shown to be a robust technique for generating nanoparticles of SnO_2 agglomerates with considerable control over particle sizes, both in our laboratory and by other researchers [57]. Therefore, not only does combustion synthesis offer the benefit of achieving control over particle characteristics, it also provides a platform for demonstrating a versatile production technique for these revolutionary particles.

1.3 Project objective and description

The primary objective of the project was to develop an understanding of the links between the microstructural properties of SnO_2 nanocomposites and the corresponding gas sensor behavior, with the end goal of using this understanding to improve sensor performance. The approach employed involved combustion synthesis as a means to generate nanocomposites of SnO_2 with varying particle sizes, morphology and dopants. The different SnO_2 nanoparticles and nanocomposites were deposited on testing platform for sensing characterization. By keeping the rest of the parameters unchanged (deposition technique, annealing temperatures and time, test gases, operating temperature, etc.) the influence of the microstructure on the sensing performance can be elucidated. The analytical techniques described earlier were utilized to perform material characterization. Material microstructure characterization of the combustion synthesized powders before and after deposition on sensing platform was necessary to identify effects of sensor fabrication on the material properties and sensing behavior.

1.4 Dissertation outline

The combustion laboratory at University of Michigan has previously demonstrated the flexibility of the combustion synthesis system to control SnO_2 crystallite size and to incorporating metal dopants such as Au, Al, Pd, and Cu in SnO_2 powders [58]. This work further explores the synthesis parameters in the flame to achieve improved control over particle size and morphology, with anticipated application of the tailored particles in gas sensors. The dissertation is divided into two main parts: (1) the combustion synthesis of SnO_2 nanocomposites and (2) application of the combustion synthesized powders for gas sensing.

Chapter 2 presents the experimental procedures that were used for the combustion synthesis and the sensor testing studies. Chapter 2 also includes discussion of sample preparation and material characterization that was conducted through out the dissertation studies. Particular deviations (if any) in the procedures are clarified in the subsequent chapters.

Chapter 3 presents the results obtained from the combustion synthesis investigation of SnO_2 nanocomposites and discussions associated with identifying the critical parameters that influence microstructure. Here mainly two systems are studied: the unassisted and the methane-assisted system that can have remarkable effect on the morphology of the particles. Apart from the synthesis of SnO_2, the decomposition mechanism of a gold additive precursor is investigated to gain better understanding of the evolution of the gold in the flame to yield the metal dopants in SnO_2.

Chapter 4 addresses the sensor response testing of the combustion synthesized particles. This chapter primarily presents the sensitivity and time response results of combustion generated SnO_2 and the doped systems. The sensor data are compared

to microstructrural evaluation of the deposited films.

The final chapter of this thesis discusses the conclusions made from this work and the resulting implications. This chapter also includes recommendations for future research avenues.

CHAPTER II

Experimental Approach

The experimental approach is divided into three sections. The first section describes the combustion synthesis facility and the experiments conducted to yield a range of nanoparticles to be used in sensor testing. The second section discusses the deposition process and experimental setup used to evaluate sensing response of the synthesized materials. The final section describes the material characterization employed to study the flame generated materials before and after the film deposition.

2.1 Combustion Synthesis

All experiments were conducted using the combustion synthesis facility shown in Fig. 2.1 consisting of a multi-element diffusion flame burner, a bubbler chamber to supply the tin dioxide precursor and a particle feed system (PFS) to deliver the solid-phase additive precursor. The experimental approach described here pertains the studies presented in Chapter 3 of the dissertation. The experiments are generally described here while the specific details are presented in Appendix A.3.

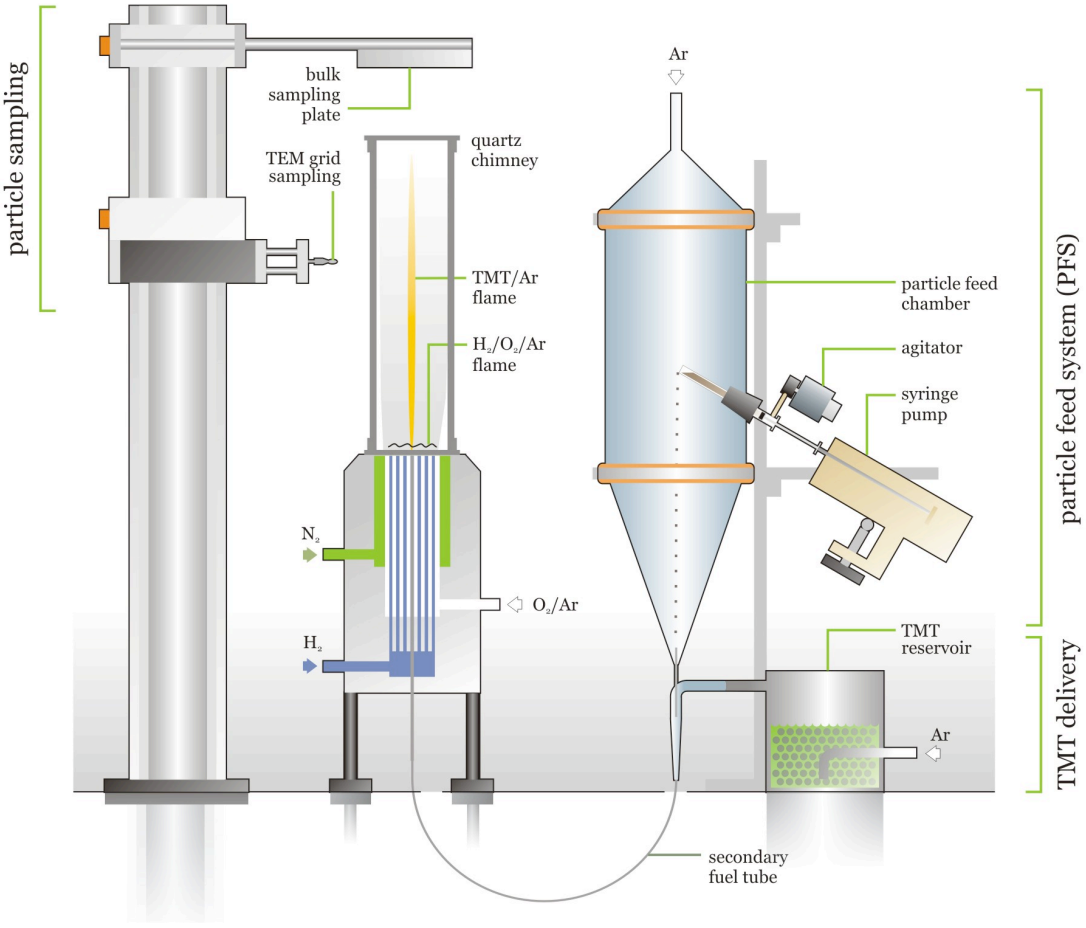

Figure 2.1: Experimental schematic of combustion synthesis facility for generation of doped tin dioxide nanocomposites. To the right of the burner are the precursor delivery chambers: the particle feed chamber and the the bubbler (TMT reservoir). While to the left of the burner the bulk sampling plate and the TEM sampling system are depicted.

2.1.1 Synthesis facility

Mutli-element diffusion flame burner

The burner is a 2.54 cm square matrix of 173 stainless steel fuel tubes (ID = 0.5 mm) and 473 oxidizer channels (ID = 0.8 mm) and is operated at atmospheric pressure. Figure 2.2 provides a schematic of the top view of the burner that shows each fuel tube surrounded by six oxidizer channels located in a hexagonal arrray. Hydrogen (H_2) is supplied at 2.78 lpm (2.09 lpm for the methane-assisted study -

see Section 3.3) to the primary fuel tubes and oxygen (O_2, 1.48 lpm) dilute in argon (Ar, 17 lpm) is supplied to the oxidizer channels. The H_2 and O_2 rapidly mix above the burner (within 5 mm) to form a nominally flat sheet of diffusion flamelets. The slightly fuel-lean $H_2/O_2/Ar$ ($\Phi = 0.94$) flame system provides the high-temperature oxidizing environment for particle synthesis. The combustion synthesis environment is shrouded by nitrogen (N_2, at 15 lpm) and a square optical chimney (3.8 x 3.8 x 34 cm) to isolate the synthesis environment and extend the high-temperature conditions. The compressed gases (H_2, O_2, Ar, N_2) had purities >99.99% (Cryogenic Gases).

A central fuel tube (ID = 0.85 mm), isolated from the fuel tube array, is used to deliver the particle precursors: tetramethyl tin (TMT, $Sn(CH_3)_4$, Alfa Aesar, 98% assay, liquid at 20 ^{o}C) to yield SnO_2 and organometallic powders for the doped-SnO_2 systems. Both the precursors are entrained in argon gas before reaching the burner using their respective entrainment systems.

SnO_2 precursor delivary

The bubbler is a sealed cylindrical aluminum container that serves as a reservoir for the SnO_2 precursor. Liquid phase tetramethyl tin is the organometallic precursor used throughout this study to produce SnO_2 nanoparticles. The bubbler is operated using argon at a flow rate of 0.0635 lpm to entrain the TMT vapor. At 20 ^{o}C, the flow through the TMT reservoir yields a mixture of 21-23% TMT (mole basis) according to previous saturation experiments [59]. A specially designed glass-metal tube connection allows mixing of the TMT-Ar and solid precursor-Ar flows to be introduced into the flame through the secondary fuel tube (schematic details are provided in Appendix A.1). Further details on the experimental setup for combustion synthesis of SnO_2 nanocomposites using the baseline system can be found in Miller

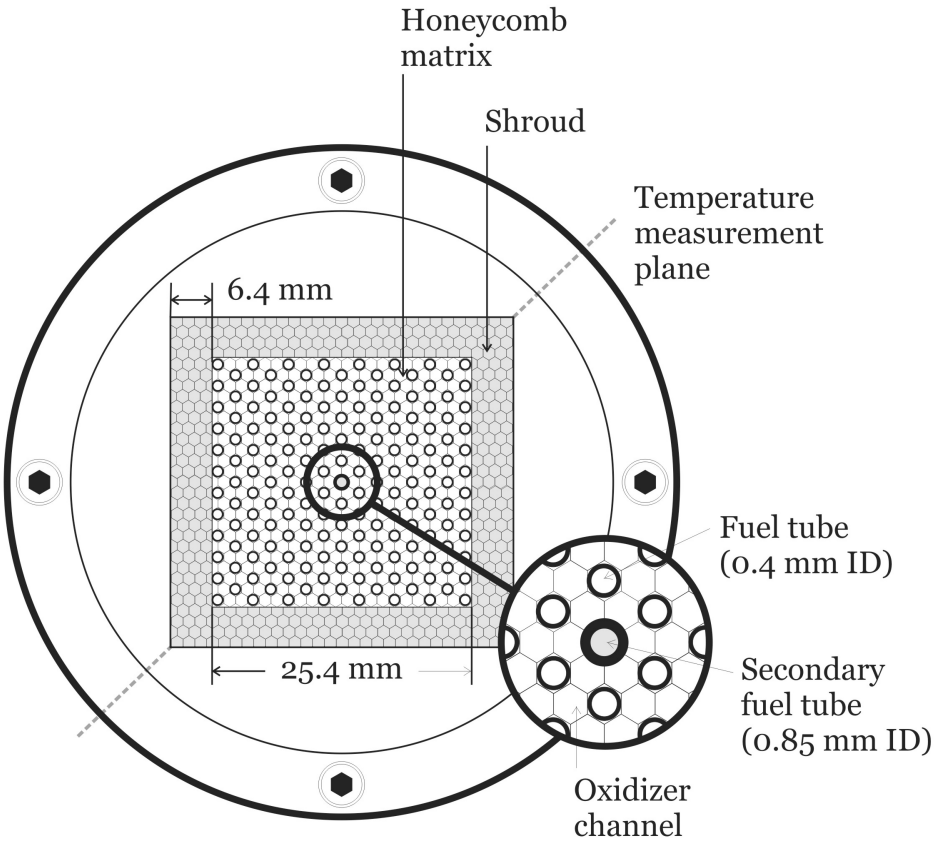

Figure 2.2: Schematic showing the top view of the burner used to produce the nanocomposite materials. The plane used for the thermocouple measurement is indicated in the figure.

et al. [60, 58]. As vapor phase TMT is introduced into the $H_2/O_2/Ar$ flame system, a long and thin yellow diffusion flame over the secondary fuel tube exit is formed. The visible portion of the TMT flame ranges in height from 15 - 20 cm without the chimney. The bubbler system was at room temperature (298 K) for all cases.

Metal dopant delivary

The solid-phase precursors are sieved to < 45 μm before use and used as-received. The solid-phase precursors are entrained in argon (flow rate of 0.26 lpm, Re = 720) using the Particle Feed System (PFS). The PFS consists of a glass entrainment chamber that has a gas inlet diameter of 3.70 mm and an outlet diameter of 1.07 mm, with a maximum diameter of 98.25 mm. The PFS introduces the organometallic particles

to the flame region at a rate of approximately 0.73 g/hr (using aluminum acetate) via an open-ended syringe (Becton Dickson, U-100) and syringe pump (Medfusion 2001). The syringe pump is set at a plunge rate of 1 mL/hr. Agitators are used to ensure a uniform flow of powders into the entrainment chamber. An AC motor was fitted with a plastic tapper to agitate the syringe at approximately 1 Hz to limit clumping of the powders at the tip of the syringe. The syringe was oriented upwards to reduce mass fall-off of the precursor which resulted in clogging of the secondary feed line or non-uniform product powder composition. When aluminum acetate powders were used to determine the delivery efficiency of the PFS to the burner, approximately 99% of the powders were collected at the burner exit. These measurements were conducted by enclosing the secondary tube exit above the burner with a cup and weighing the cup before and after a complete feed of measurement powder. Using densities of gold acetate and aluminum acetate the gold acetate delivery rate can be estimated. The nominal delivery rate for gold acetate was calculated to be 1.4 g/hr.

The organometallic precursors considered for this study are gold (III) acetate ($Au(C_2H_3O_2)_3$, Alfa Aesar, solid at 20 ^oC), copper (II) acetate ($Cu(C_2H_3O_2)_2.H_2O$, Alfa Aesar, solid at 20 ^oC), palladium acetate ($Pd(C_2H_3O_2)_2$, Sigma-Aldrich, solid at 20 ^oC) and aluminum acetate ($Al(OH)(C_2H_3O_2)_2$, Sigma-Aldrich, solid at 20 ^oC).

Methane-assisted system

An iteration on the setup described above was performed by replacing the argon carrier gas through the PFS with methane gas at a flow rate of 0.41 lpm (Re = 1054). This allowed production of particles using methane-assisted combustion synthesis (MACS). The purpose of the iteration was to increase the temperature in the synthesis region of the flame. For the MACS, the optical chimney was utilized to

reduce room air entrainment. Figure 2.3 shows a schematic of the MACS mode of operation. A narrow slot on one side of the optical chimney provided access for the particle sampling from the methane-assisted system. For better comparison between the two systems, the unassisted system was also fitted with the chimney for this particular study. The nitrogen flow to the shroud was adjusted (lowered) to obtain the blue flame around the TMT flame. The blue flame is attributed to the presence of methane in the MACS system. Argon was still used as the carrier gas for TMT and the $H_2/O_2/Ar$ flame conditions were unchanged.

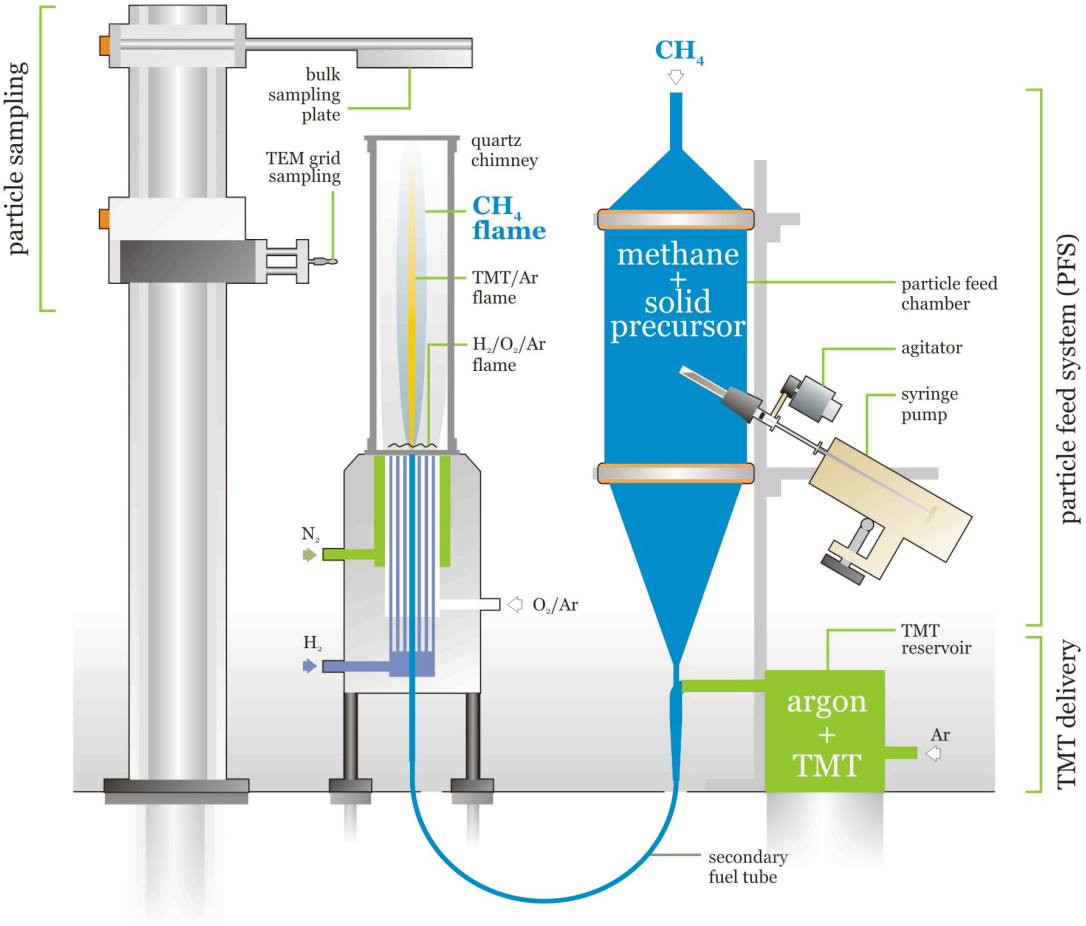

Figure 2.3: Schematic of the methane-assisted synthesis facility. The blue methane flame envelopes the yellow TMT flame in the synthesis region of MACS.

2.1.2 System characterization

In order to characterize the reactor conditions, temperature and velocity profiles were obtained for the synthesis environment. Temperature measurements were made using a platinum/rhodium S-type thermocouple (with bead diameters of 0.050 and 0.125 mm) and were corrected for radiation and deposition of material onto the thermocouple surface. An optical microscope (Leica) was used to monitor the size of the thermocouple bead and account for radiation. Temperature measurements were taken slightly off-center above the burner to avoid the secondary tube exit (and the region of high deposition of particles on the thermocouple). Uncertainties in the temperature measurements are estimated at ± 50 K.

Particle velocities for the initial nanocomposite study (Section 3.1) were examined for the aluminum acetate system using high-speed digital camera (Vision Research, Phantom v.7.1, Nicor 50 mm lens f/0.95). The argon flow rate to the primary flame was lowered to 11.4 lpm (as opposed to the typical operating condition of 17.1 lpm), to improve the imaging and TMT was not used with the secondary fuel tube. Sequences were acquired for 3 s with a frame rate of 1 kHz and an exposure time of 938 μs. Particles were tracked and counted using Vision Research software (v. 6.0.6). Residence times along the axis of the burner were estimated by integrating the velocity proles obtained from the particle tracking measurements to the appropriate distance from the burner surface.

For the methane study (Section 3.3), velocity fields were obtained at various locations above the surface of the burner. The velocity fields were determined using particle imaging velocimetry (PIV, LaVision Spray/PIV System with 532 nm high rejection filter) with aluminum acetate as the seed particles in argon flow. Average

velocities at several locations above the burner exit were evaluated to determine velocities as a function of height above the burner. These results were also used to confirm the earlier method used to determine particle velocities.

Table 2.1: Chemical reactants used in the combustion synthesis experiments

Reactant	Chemical Formula	Manufacturer	Purity
	Gas-phase burner reactants		
Hydrogen	H_2	Cryogenic Gases	99.99%
Oxygen	O_2	Cryogenic Gases	99.93%
Argon	Ar	Cryogenic Gases	99.98%
Nitrogen	N_2	Cryogenic Gases	99.98%
Methane	CH_4	Cryogenic Gases	99.98%
	Liquid-phase SnO_2 precursor		
Tetramethyl tin	$Sn(CH_3)_4$	Alfa Aesar	98%
	Solid-phase dopant precursors		
gold (III) acetate	$Au(C_2H_3O_2)_3$	Alfa Aesar	99.9%
copper (II) acetate	$Cu(C_2H_3O_2)_2.H_2O$	Alfa Aesar	99.999%
palladium acetate	$Pd(C_2H_3O_2)_2$	Sigma Aldrich	99.8%
aluminum acetate	$Al(OH)(C_2H_3O_2)_2$	Sigma Aldrich	-

2.1.3 Sample acquisition

Bulk samples were collected 50 cm (when the optical chimney was present, unless otherwise noted - see Appendix A.3 for details) above the surface of the burner using a water-cooled plate (with sampling times of 10-15 mins depending on precursor loading in the syringe). Without the optical chimney and with the nitrogen shroud, the sampling height was lowered to 37 cm to improve powder capture efficiency. The cooled plate was designed to provide a clean surface for thermophoretic deposition of synthesized powders. The bulk sampling plate hosted a serpentine channel for water cooling was machined from an aluminum block. Drawings for the bulk sampling plate are provided in Appendix **??**. The samples were collected on aluminum film tape attached to the bottom of the cold plate. The tape was replaced for each experiment

to avoid cross-contamination. The samples were removed from the tape at the end of the experiment for *ex situ* analysis.

The bulk samples were primarily used for XRD or SEM analysis. Powders obtained from the bulk sampling were also used for preparation of the sensors. Sensing powders were collected at a height of 37 cm above the burner using both the optical chimney and the nitrogen shroud to maintain the high temperatures and reduce room air entrainment. The chimney also provided greater collection efficiency of the synthesis products at the cold plate. For the sensing powder experiments, the collection rate was approximated at 1.6 g/hr.

Discrete samples were collected by direct deposition onto TEM grids (copper, 300-mesh, Electron Microscopy Sciences) rapidly inserted into the combustion synthesis environment. The grids were inserted using a pneumatic piston-cylinder assembly that was characterized to spend a minimal time in the synthesis environment. The nitrogen-actuated (at 100 psi) complete stroke time was measured to be 0.27 s, of which 0.16 s was spent in the hot gas region. The determination of the residence time of the grids was done using high-speed imaging (Vision Research, Phantom v.7.1, Nicor 50 mm lens f/0.95) to measure the velocity of the grid translation. Experimental details and results for the sampling piston are reported in Appendix A.5. The height of the sample can be adjusted by vertical translation of the sampling apparatus on the structural rail (X95, Newport), which also supported the cold plate (depicted on the left of Figure 2.1).

2.1.4 Gold acetate thermal decomposition study

Decomposition experiments

In order to investigate the thermal decomposition mechanism of gold precursor, gold acetate, a separate set of experiments were conducted outside of the flame environment. The motivation was to slow down the decomposition and allow visual access to the fragmentation process. The experiments were conducted on a hot-plate with relatively high heating rate to mimic gold acetate decomposition in a flame. Further background for this study is provided in Section 3.2.

All experiments were conducted using gold (III) acetate ($Au(C_2H_3O_2)_3$, Alfa Aesar, 99.96% Au). The as-received powders ranged in color from light brown to black. The source of the variability in the color (e.g. differences in particle size, partial decomposition of the powders, etc.) was not identified by the manufacturer. Based on the results of this study (presented and discussed in Section 3.2), we attribute the differences in color to partial decomposition of the gold acetate powders.

For the hot-plate experiments, the powders were heated at a rate of approximately 25 ^oC/min (Fisher Scientific, Thermix Hot Plate Model 300T) in room air. A high-speed digital imaging video camera (Vision Research, Phantom v.7.1, Nicor 50 mm lens f/0.95) was positioned approximately 100 mm from the hot plate for side-view imaging of the gold acetate particles. A 15 mm c-mount extension tube was used with the camera to optimize image quality. A metal halide lamp (ED 28 Universal bulb, 400W) was used to illuminate the decomposing particles on the hot plate.

The following procedure was used for the hot plate experiments. Gold acetate particles ranging from 0.5-1.0 mm in size were placed approximately 30 mm from the edge of the hot plate. The high-speed imaging camera was operated at 4800 frames

per second (208 μs) with a spatial resolution of 800x600 pixels. The exposure time was set to 19 μs. The camera was manually triggered to record the particle decomposition process after particle heating was initiated. During the experiments, a K-type thermocouple was used to record the temperature of the hot plate approximately 2 mm away from the gold acetate particles.

Analysis samples

Powders before and after the decomposition process were collected for electron microscopy analysis. The as-received gold acetate powders were deposited on copper tape and sputter coated with Au-Pd (to improve image contrast) and then imaged using a scanning electron microscope (SEM, Philips XL30). The products of the heated gold acetate particles were collected by direct deposition of the particles ejected during decomposition onto transmission electron microscope (TEM) grids. The TEM grids were placed vertically at distances of 1 mm, 2 mm and 4 mm away from the initially unreacted gold acetate particles. Unreacted (as-received) gold acetate powders and partially decomposed gold acetate powders were analyzed by XRD as described later.

2.2 Sensor preparation and testing

2.2.1 Sensing platform

In order to test the materials for sensing activity a sensing platform is required to measure the resistance response of the materials as a function of gases present. Typically, a tin dioxide sensing platform is equipped with an interdigitated electrodes to measure the resistance of the film, a heater to keep the film at elevated temper-

atures for chemisorption to proceed, and a temperature sensor to monitor the film temperature during the conditioning stage.

The tests conducted for this project utilized a commercial multi-sensor platform from Heraeus Sensor Technology (MSP 632, DWM & Associates, New Brunswick, NJ, http://www.dwmai.com). These are single-sided sensors with platinum electrodes, heater and temperature sensors printed on a 3.2 x 6.1 mm alumina substrates (500 μm thick). The inter-electrode distance is 10 μm and electrical leads are provided for measurement and supplying power to the heater. Figure 2.4 shows a schematic of the sensor platform as well as the sensing film that is deposited on the platform. The temperature calibration for the platinum resistive temperature sensor is provided by the manufacturer.

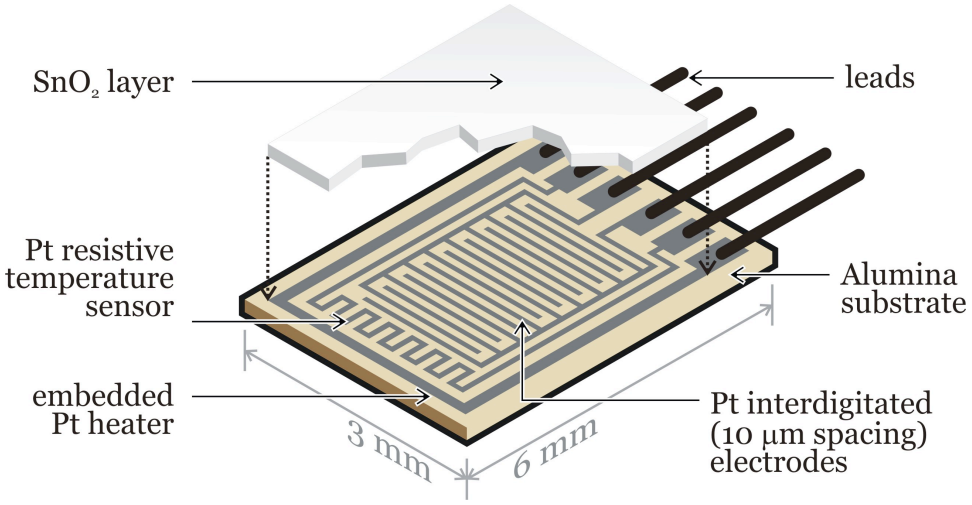

Figure 2.4: Physical and circuit schematic of the commercially available Heraeus MSP 632 multi-sensor platform equipped with interdigitated electrodes, temperature sensing serpentine and embedded platinum heater.

2.2.2 Custom sensing platform

A custom sensing platform was also fabricated using microfabrication. The fabrication involved depositing electrodes for sensing, the heating circuit and the tem-

perature sensing circuit on a polycrystalline aluminum oxide substrate. The 50.8 x 50.8 x 0.5 mm alumina substrate (95% purity) was purchased from MTI crystals (http://www.mticrystal.com). The initial configuration for the sensor platform consisted of interdigitated platinum electrodes on one side with the heater and the temperature sensor on the other side of the substrate, see Fig. 2.5. Low optical contrast between Pt and alumina on the mask aligner led to difficulty aligning the top and backside patterns for this design. Consequently, the design was altered to a single-sided platform which included the heater and the temperature sensor on the same side, as the sensing electrodes. This design also reduced the number steps involved in the microfabrication process for the platform.

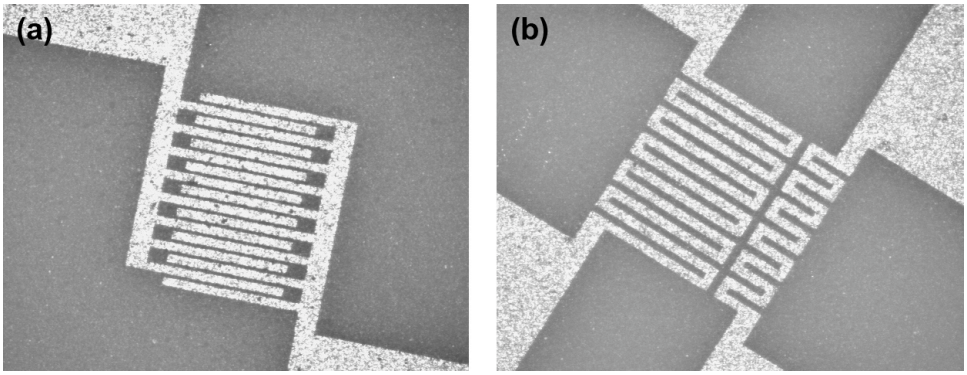

Figure 2.5: Optical microscope images of the initial sensor testing platform design involving a double-sided sensor on alumina. (a) platinum interdigitated electrodes (b) platinum heater and temperature sensor circuit.

Microfabrication

The sensor platform fabrication was performed at the solid state electronic laboratory (SSEL) facility at University of Michigan. The circuit layout and design was created using AutoCAD software which was then processed to generate a mask maker file. A 5 x 5 inch chromium plated glass mask with 42 sensing circuits was generated using EVG Mask Maker, followed by a chromium etch and pattern de-

velopment procedure. The substrate was prepared for UV pattern exposure by spin coating hexamethyldisilizane (HMDS) and photoresist (PR 1827), which served as adhesive and photosensitive polymers, respectively. MA/BA-6 Mask Aligner was used to expose the photoresist with the circuit pattern. The pattern was developed using MF 319 developer followed by removal of the exposed pattern using DI water. A physical vapor deposition (PVD) chamber (EnerJet Evaporator) was used to evaporate and deposit titanium (20 nm thickness) followed by platinum (100 nm thickness) on the substrate. Titanium was used as the adhesive layer between the platinum and alumina due to its tendency to readily form oxides at the metal-ceramic interface. An acetone lift-off process removed the excess platinum and titanium to produce the final sensor platform. Figure 2.6 shows optical microscope images of the single sided sensor with 2 x 2 mm contact pads for electrical connection for resistance measurements. The electrodes are 40 μm wide with an inter-electrode gap of 20 μm. Two single-sided platforms were fabricated for preliminary testing with 20 functional sensing circuits on each. Further, two double-sided platforms were produced by visual alignment of the front and back circuits.

2.2.3 Film deposition

Dispersion-drop method

The combustion generated powders of SnO_2 were sampled using a cold plate and were ground with mortar and pestle before dispersing in a solution. The undoped SnO_2 dispersion was obtained by adding 0.118 g of SnO_2 to 6.281 g of solution. This yielded approximately 1.85 wt% SnO_2 in the dispersion. The powder was dispersed in a solution of ethanol (15%) and distilled water (85%) using a sonic horn (Sonics VC-505 Ultrasonic processor). The powder would remained in dispersion for

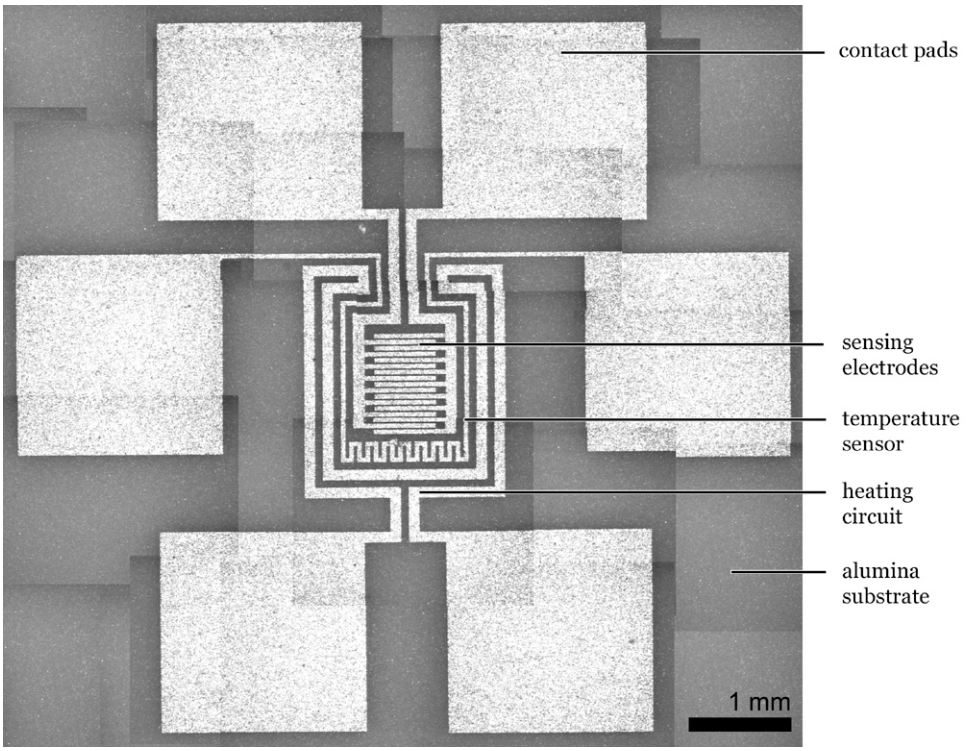

Figure 2.6: Optical microscope image of one single-sided sensor on 2 inch alumina wafer.

approximately 10-15 minutes before beginning to settle in the solution. Before every deposition the dispersion was sonicated at 20% amplitude (at 20 kHz) for 1 min. A micropipetter (Fisherbrand Finnpippette I Pipetters) was used to deposit a single drop of 10 μL on a clean platform. Typically the drop was allowed to evaporate at ambient conditions followed by a low heating step. The low heating step was performed in the muffle furnace (Fisher Scientific) at 80 ^{o}C for half an hour. This was followed by another drop deposition step to add a second layer and a low heating step leaving the film of the dispersant behind. Generally five such layers of tin dioxide were deposited before sintering the film at high temperature. The sintering process involved stepwise increase in temperature (typically stopping at around 100 ^{o}C and 250 ^{o}C, since the furnace was not equipped with an automated ramp rate) from ambient conditions to 500 ^{o}C. The sensors were kept at 500 ^{o}C for 1.5 hrs before allowing the furnace to cool to ambient conditions (which took approximately 3 hrs).

At this point, the sensors were ready to be mounted to the breakout board for testing. Doped tin dioxide powders were prepared using identical procedure.

Binder-paste method

Often in practice binders are added to SnO_2 to achieve better connectivity between the particles and the substrate. Silicate binders are commonly used for such sensors, which have shown to improve sensor's transient response as well [13]. For the binder-paste method, xerogel-based binder recipe was used, as recommended by Ihokura *et al.* [13]. The recipe involved combining tetraethylorthosilicate (TEOS), ethanol (C_2H_5OH), distilled water (H_2O), and 2 % hydrochloric acid (HCl) according to the volumetric ratio 65:27:7:1 which yielded 26 wt% silica. The amount of binder added to the powder was adjusted to yield 14 wt% silica in the film to achieve reasonable rheological characteristics. The binder-powder mixture formed a dry paste that was uniformly spread over the sensing platform into a $\sim$50 μm thick film. The film was allowed to dry at ambient temperatures (evaporation of mostly ethanol) followed by the sintering step at 500 ^{o}C for 1.5 hrs in the muffle furnace. Again, doped tin dioxide sensors were processed identically.

Deposition for custom platform

In order to deposit the doped or undoped tin dioxide on the custom wafer (50.8 mm x 50.8 mm) a spin coating process (Laurell Technologies Spin Coater, WS-400B-6NPP-Lite) was developed. For preliminary tests bulk SnO_2 powder was ball-milled to remove soft agglomerates. The powder was dispersed in an ethanol (15%) and water (85%) solution using a sonic horn (Sonics VC-505 Ultrasonic processor). The dispersion was used to spin-coat (at 750 rpm) a layer of tin dioxide on the as-

purchased alumina substrate to test for adhesion. Successful adhesion was achieved on unpatterned susbstrate after heat treating the substrate at 200 ^{o}C for 2 hours in a muffle furnace (Fisher Scientific).

2.2.4 Sensor testing

Testing facility

The testing facility was designed and built to test the sensing response of the combustion generated materials to a target gas. The testing facility consisted of a glass flow chamber (ID 67.5 mm, total volume $\cong$ 700 mL) used to house the sensor during testing. A premixed tank of CO (1000 ppm) in dry compressed air (Cryogenic gases, 99.99%) was mixed with another flow of dry air to dilute the CO to the range of concentrations of interest in the parametric study. Typically tests were performed with CO concentration at 500 ppm in dry compressed air. The gases are metered with digital flow meters (TSI 4100) that flow into a stainless steel mixing tank (150 mL) prior to introduction to the sensor test chamber. A total volumetric flowrate of 400 mL/min was maintained for all the tests. The gases are exhausted to an exhaust line at the other end of the glass flow chamber at a slight vacuum. Figure 2.7 shows a schematic and an image of the sensor testing facility used for the experiments.

Each sensor was mounted to an ethernet breakout board (Winford, winford.com) and connected to a power supply and a picoammeter via an ethernet cable. A BK Precision 1760A power supply was used to power the sensing platform heater. The temperature monitoring and film resistance measurements were made using Keithley 6487 Picoammeter/Voltage source connected to a PC for data acquisition and analysis via a RS-232-to-USB connection. Temperature monitoring was based on a calibrated platinum RTD circuit with the calibration supplied by the manufacturer

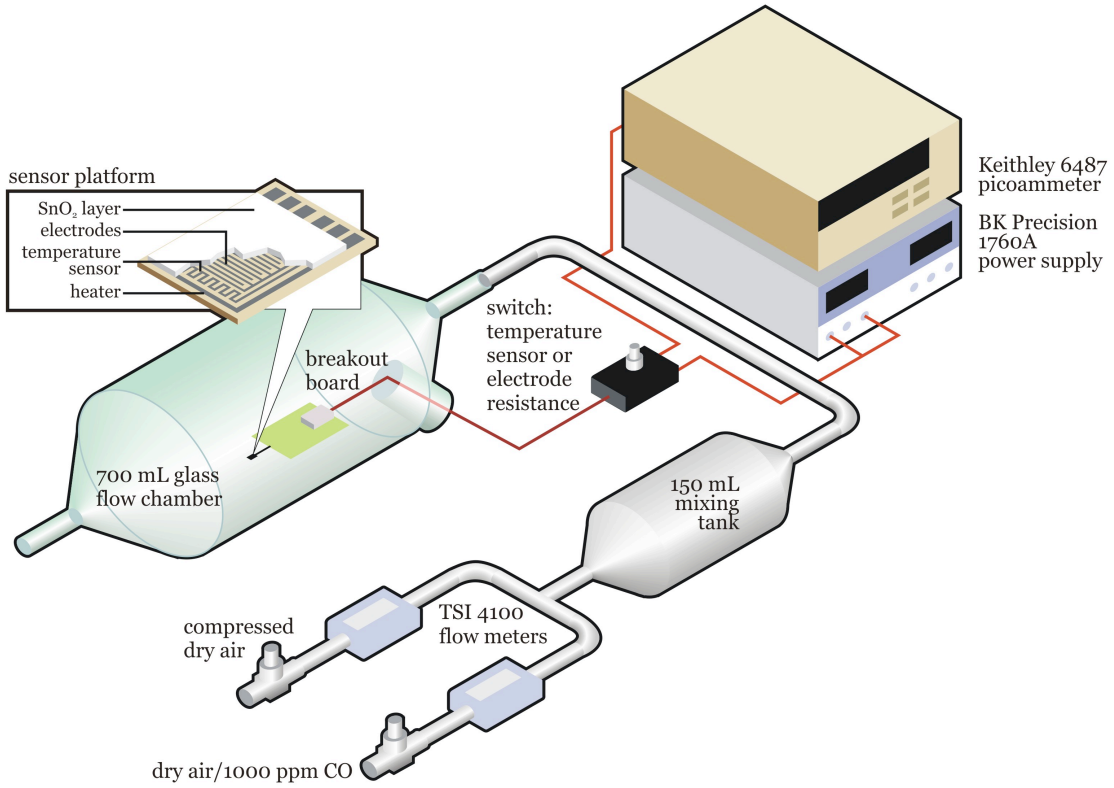

Figure 2.7: Sensor testing facility for monitoring resistance change in the sensing film to 500 ppm carbon monoxide in dry air. The sensor is maintained at high temperature using a resistive heater embedded in the sensing platform. The switch is used to alternate the resistance measurement from the electrode and temperature sensor.

(Heraeus).

In order to measure the resistance of the sensor and supply heater power to the custom wafer, a probe mount was constructed using acrylic sheets to hold the tungsten probes (each with a shaft diameter of 0.5 mm with a 200 μm tip) that make contact with the platinum contact pads on the wafer. Figure 2.8 shows the probe station assembly with wafer and the tungsten probe block.

Sensor tests

The sensors were typically tested at an average operating temperature of 330 ^{o}C. The temperature of the sensor was increased to the operating temperature at a

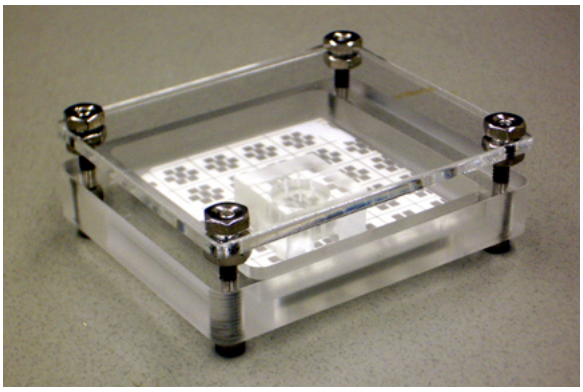

Figure 2.8: Acrylic probe station assembly for achieving electrical contact with the custom sensing platform (with multiple sensors). Tungsten tips are used as probes.

relatively slow rate (∼5 ^{o}/min) to avoid film de-lamination which occurred during rapid heating or cooling. The sensors were maintained at the operating temperature for at least 24 hrs before testing, in order to condition the sensing film. The heating power required to maintain the operating temperature of 330 ^{o}C was approximately 1 W (V = 6.6 V and I = 0.154 A).

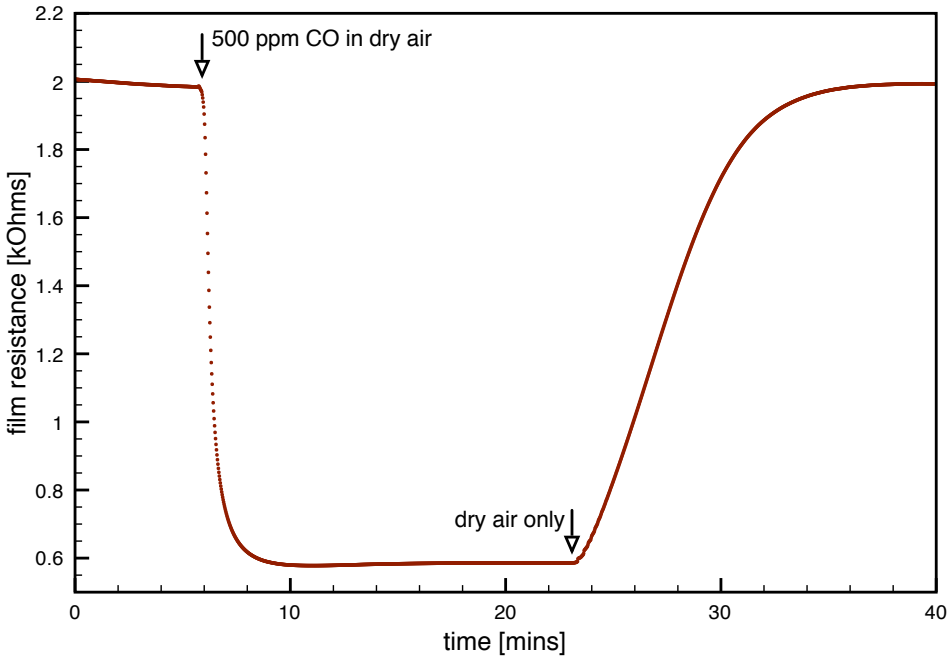

Figure 2.9: A typical combustion synthesized SnO_2 response to 500 ppm CO in dry air. As CO/dry air mixture is turned off the absolute resistance returned to the baseline value in dry air flowing at 400 mL/min.

Once conditioned at the operating temperature, the flow chamber was purged with dry air at 400 mL/min for an hour in order to remove any moisture or impurities in the chamber. The configuration of the electrical setup did not allow simultaneous monitoring of the resistance from the temperature sensor and the electrodes. Therefore after the purging step, the temperature of the sensor was calculated and recorded. The testing began with triggering the picoammeter to begin acquiring data as per the parameters set on the ExceLINX software (V2.0) package provided by Keithley. Generally the applied voltage on the instrument was set to 1.0 V with a current limit of 25 mA. The data acquisition rate was set at $\sim$0.8 Hz. Figure 2.9 presents a typical sensor resistance as a function of time. The first ten minutes of any test involved flowing dry air into the chamber to establish the resistance baseline and to avoid the initial transience in response. After approximately ten minutes into the test the dry air flow rate was lowered to 200 mL/min while introducing a CO-dry air mixture of equal flow rates to yield 500 ppm of CO in the flow chamber. This resulted in lowering of the resistance of the sensor to a new value until a relatively stable value was achieved. The film resistance generally reached an equilibrated condition within 5-10 minutes. Once the low resistance value was established the CO-dry air mixture flow was reduced to zero while increasing the dry air to a flowrate of 400 mL/min. After this step, the original resistance in dry air was recovered (and this time is referred to as the recovery time). For each sensing test, three runs were conducted without halting the gas flows or changing the operating temperature. The cycle of three tests took approximately 3-4 hours. After the tests were completed, the sensor was either cooled to ambient conditions or left at the operating temperature conditioning state.

Sensor response analysis

Two performance criteria were selected to monitor as a function of the SnO_2 microstructures and additives: sensitivity and time response. Stability and selectivity measurement experiments were not conducted for this project in order to limit the parametric space of the study. Gas sensor sensitivity (S) was calculated using the traditional definition where the resistance of sensor in air (R_a) is divided by the resistance of the sensor in the target gas (R_g), as seen in Eq. 2.1. An alternative sensitivity (referred here as S_{alt}) definition was also evaluated; defined as Eq. 2.2. S_{alt} takes into consideration the absolute magnitude of the sensor resistance. Time response (τ) was evaluated as the first order time response of the resistance change.

$$S = \frac{R_a}{R_g} \tag{2.1}$$

$$S_{alt} = \frac{R_a - R_g}{R_a} \times 100\% \tag{2.2}$$

A MATLAB algorithm was developed to evaluate the sensitivity and time response based on the data acquired from the Keithley picoammeter. The approach involved taking the absolute resistance and the corresponding relative time to determine the local minima in the derivative of the signal, which yielded the approximate time when the sensor responded to the presence of CO inside the chamber. This marker was used to determine the sensitivity from the maximum and minimum resistance around the local derivative minima. This portion of the data was also used to linearize the signal by calculating the natural log of the resistance and plotting against relative time. The slope of the linear fit provided the first order time response of the sensor.

Figure 2.10 provides an example of the output plots generated from the data analysis by the MATLAB algorithm. Appendix B.2 provides the MATLAB algorithm used for the data analysis.

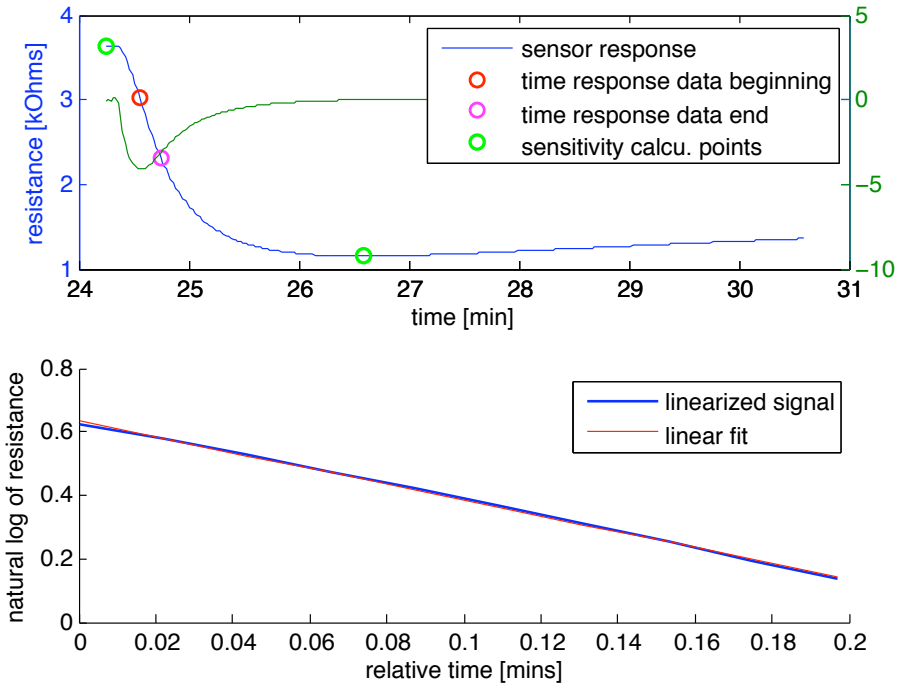

Figure 2.10: An example of the plot outputs generated by the MATLAB program used to evaluate the sensitivity and time response of sensor data. The panel on the top indicates the points used to calculate sensitivity and the start and end points of the data subset used to determine the first order time response. The bottom plot shows the linearized signal and the linear fit to indicate the quality of the fit.

2.3 Material characterization

In order to understand the effects of the synthesis environment on the nanoparticles produced, several techniques were used to characterize the product powders, including x-ray diffractometry (XRD), and electron microscopy with x-ray energy dispersive spectroscopy (XEDS). The bulk samples were analyzed using XRD (Scintag Theta-Theta X-Ray Diffractometer) and scanning electron microscope (SEM).

The transmission electron microscope (TEM) grids were imaged using analytical and high resolution TEM (Philips CM12 and JOEL 3011) equipped with x-ray energy dispersive spectroscopy (XEDS) units. The same approach was taken when studying the deposited films in order to document the corresponding microstructural properties for given sensor response.

2.3.1 X-ray diffraction

Samples for XRD were collected from the bulk sampling plate and deposited on a glass slide (∼40 mg). The powders were mixed with isopropyl alcohol to make a paste that was dried at ambient conditions for 10 mins prior to the analysis. This was done to obtain a uniform film on the glass slide. XRD was used to provide the crystallographic identity of the materials present in the powder based on the XRD features that correspond to catalouged peaks for individual crystalline materials and phases (JCPDS database [61]). Additional important information that XRD spectra provide is the average crystallite size based on peak broadening according to the Scherrer equation:

$$d_p = \frac{0.9\lambda}{\beta_{1/2}\cos\theta} \tag{2.3}$$

For SnO_2, high resolution XRD scans were conducted over the $\langle 110 \rangle$ feature, where $\lambda = 0.1542$ nm, $2\theta = 26.6\ ^o$ and $\beta_{1/2}$ is the full-width at half maximum (FWHM). The lambda, λ, corresponds to the x-ray source wavelength which in this case is the Cu Kα line. The FWHM for each feature of interest was determined using the XRD software peak fitting function (which used Pearson 7 fit) and which also provided the 2θ location of the given peak. The peak analysis used to determine the crystallite

sizes (on Scintag software) is provided in Appendix C.1. Generally, the broader the XRD features, the smaller the average crystallite size.

Scans for phase identification and for average crystallite size of the tin dioxide were obtained using an automated Scintag Theta-Theta XRD with step sizes 0.02^o 2θ. The full scans were obtained over a 2θ range of 15^o-90^o at a scan rate of 4^o 2θ/min. Spectral scans for average crystallite size were measured over a 2θ range of 23^o-36^o at a scan rate of 0.5^o 2θ/min.

XRD analysis of the sensing film materials was performed on glass slides that had been processed identically and in parallel to the corresponding sensor except for deposition substrate material. The, deposition (paste or drop) was performed on the sensing platform and on a glass slide simultaneously which was followed by identical annealing processes to yield film properties that would parallel the characteristics of the sensing film. This method tracks changes in crystallite sizes that may occur after annealing.

2.3.2 Electron microscopy

An analytical and high resolution TEM (Philips CM12 or JOEL 3011) was used to analyze the TEM samples from the combustion synthesis studies of the materials. The copper grids (3 mm diameter, Electron Microscopy Sciences, carbon film, 300 mesh copper) were inserted into the synthesis environment using tweezers attached to the piston-cylinder sampling unit described above. The grids were made of open squares approximately 54 μm in length with carbon film covering one side allowing a surface for deposition of the particles. TEM images provided nanocomposite structure while image analysis (described below) was used to determine the primary particle size distribution in the SnO_2 aggregates. TEM samples were taken at various

locations above the burner which provided information about how the particles sizes and morphologies were evolving through the synthesis region.

TEM imaging of the dispersed powders (from the dispersion-drop method) was performed to elucidate the nature of dopants within the SnO_2 powders. These samples were obtained by depositing a drop of sonicated sample of doped-SnO_2 powders on a TEM grid and allowing the solution to evaporate. No annealing process was used, since the carbon film would evaporate at high temperatures.

SEM analysis (SEM, Philips XL30) performed on the bulk samples provided qualitative porosity of the powders and composition information based on XEDS measurements. Typically, the metal acetates were imaged to determine the structure before decomposition. Due to the high decomposition characteristics, these particles were sputter coated with 15 nm thick Au-Pd layer. The powder particles were deposited on conductive copper tape.

SEM was useful for observing the large scale structures of the deposited sensing film. Here the sensing platforms were placed on a copper tape and observed for cracking, film uniformity, porosity as well as film thickness. All SEM images of the sensors were taken after the sintering step at high temperatures.

Analysis of micrograph images

Automated image analysis of TEM or SEM images can be challenging due to the highly aggregated particles and overlapping/necked features. Such features are very common in combustion generated tin dioxide powders. Often manual counting is employed for better feature identification. In this work, a semi-automated method was developed to assist the manual counting and greatly decrease the time required to generate particle size statistics. The method automates the accounting of feature

sizes, leaving feature identification to be performed manually. The process facilitates rapid acquisition of statistically significant data.

The procedure involves two steps which are illustrated in Fig. 2.11. The first step is feature identification, which requires duplication of features in a vector graphics package (e.g. CorelDraw or Adobe Illustrator). The features of interest (e.g. primary spherical particles) are identified from the background in the image by overlaying equivalent outlines on the features. The overlays are then extracted into a new file and aligned in a column, with no overlap between features. The scale bar is duplicated in the new image. Exporting the vector-graphic generated features to a binary (black and white) bitmap image file produces an image with either 1 or 0 value for each pixel. Such a file can be readily analyzed using an algorithm to extract particle size distribution by counting the zeros in the central column of each feature and applying the appropriate scale. In the current work, the particle size distributions were extracted assuming spherical particles and using a Matlab algorithm to analyze the bitmap images. The Matlab code used for this analysis is provided in the Appendix C.2 of this document.

Automated image analysis software is highly successful in providing particle statistics when particles are unaggregated. Therefore, in the gold acetate decomposition study, where discrete spherical particles of gold were observed on the TEM grids, Java-based ImageJ software [62] was utilized for image analysis. After subtracting the background via thresholding the algorithm provided average particle size, as well as the particle distribution.

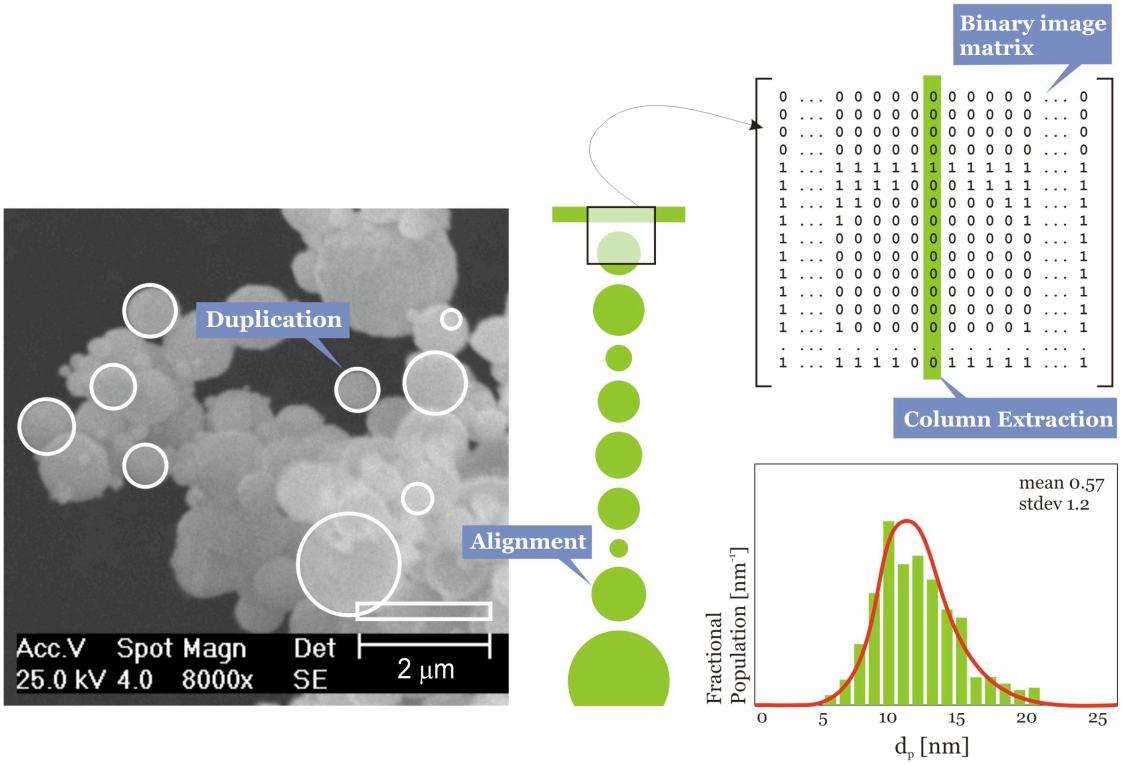

Figure 2.11: Schematic indicating the technical approach used for the semi-automated particle dimension analysis. On the left is an SEM image of the gold particles illustrating the procedure to identify particle features and the image magnification. The center section shows the features harvested from the image and aligned in a single column. On the right is the binary matrix image generated from the black and white particle array. In the image matrix, 0 corresponds to black pixels or zero intensity and 1 corresponds to white pixels or saturated intensity.

2.3.3 Other characterizations

Other material characterization methods were employed to gain further insight into the effects of microstructure and composition. One of the most common procedures that was employed to determine the material composition was x-ray energy dispersive spectroscopy (XEDS). XEDS units were attached to electron microscopes, therefore it was a useful method to determine the elemental composition of the particles being observed under TEM or SEM. In order to gain more accurate composition measurements, electron-microprobe analysis (EMPA) was performed on dispersion-

drop films of gold- and palladium-doped SnO_2. The films were deposited on glass slides and allowed to dry at ambient conditions. Liquid nitrogen specific surface area analysis via adsorption (using BET method) was conducted on both SnO_2 and gold acetate powders. The BET measurements were provided by Micromeritics, Inc and were conducted using as-received gold acetate powder.

Thermogravimetric Analysis (TGA) was performed on the gold acetate to determine the decomposition temperature (Section 3.2) as well as the percent weight loss of the sample due to decomposition to metallic gold. The TGA experiments were conducted in an inert (nitrogen) environment using a heating rate of 5 ^oC/min (TA Instruments Q50).

CHAPTER III

Combustion Synthesis

The studies conducted previously by Miller *et al.* [58] have demonstrated an appreciable degree of control over the combustion synthesis products. The current work goes further into investigating the various processes that lead to the formation of nanocomposites; in other words, how the particles are evolving in the combustion synthesis process. It is believed with this understanding, the critical parameters that influence particle characteristics can be identified. Parameters such as decomposition temperatures, sintering rates, solid-phase fragmentation, etc., can potentially be controlled to yield particles with tailored characteristics. Specifically for tin dioxide, particles with a range of microstructural properties can be tested for sensing response to understand the microstructure-performance links. Presented here are three key studies that contributed to the elucidation of the particle evolution in the high-temperature CS environments. The studies focus on nanocomposite synthesis (Section 3.1), gold acetate decomposition (Section 3.2) and methane-assisted synthesis (Section 3.3).

3.1 Nanocomposite synthesis

The primary objective of this work was to identify the combustion processes and reactant characteristics affecting the microstructural properties of nanocomposite materials fabricated using a combination of solid- and gas-phase precursor reactant materials. Links between the properties of the solid-phase reactants (such as particle size and chemical structure) and the condensed-phase products are critical for designing composition and microstructure of a nanocomposite. Improved understanding of these links will greatly facilitate expansion of the combustion synthesis method to additional material systems and applications. In order to meet the objective of the study, the synthesis environment was characterized, and analyses of the reactant and product particles were conducted to identify and quantify the properties as a function of the reactor conditions. The results are discussed in terms of potential reaction pathways. The bulk of this work was presented and discussed in Bakrania *et al.* [63].

3.1.1 Characterization of unburned solid-phase reactants

Table 3.1 provides a summary of the solid-phase precursors investigated and the thermophysical properties of the precursors. Bulk of the material properties were obtained from the CRC Handbook [64]. For many of the materials considered, there are limited thermodynamic data, such as melting and boiling points, enthalpies of vaporization, etc. The most critical data for this study are the decomposition temperature and the density of the solid phase reactants. Estimates were available for all the metal acetates considered in this study, except for gold acetate. As a consequence, efforts were made to determine these properties using simplified yet

quantitative methods.

The as-received gold acetate was analyzed using a displaced gas volume method (Micromeritics, AccuPyc 1330) to determine the particle mass density listed in Table 3.1. The decomposition temperature of the gold acetate was estimated using a visual melting temperature tool (MEL-TEMP 3.0). A sample of the unreacted gold acetate ($\sim$20 mg) was placed in a capillary tube (i.d. 0.9 mm). The tube was heated and the sample observed. The decomposition temperature was approximated as the temperature at which a dramatic change in the color of the powder took place, from light brown to a dark brown. The relationship between the color change and the degree of decomposition was later investigated and confirmed in the gold acetate thermal decomposition study (see Section 3.2). The experiment produced a decomposition temperature in the range 150 - 160 ^{o}C for gold acetate. This range is consistent with the decomposition temperatures of other metal acetates (see Table 3.1) and thermogravimetric analysis (TGA) conducted at a later stage which yielded a decomposition temperature of 170 ^{o}C (see Section 3.2). Additionally, the visual method reproduced a decomposition temperature for palladium acetate in the range of 222 - 229 ^{o}C, which is in good agreement with the literature value for palladium acetate of approximately 240 ^{o}C [65]. The systematically lower temperature for the visual decomposition temperature analysis method is attributed to the gradual (as opposed to instantaneous) decomposition process before the abrupt fragmentation observed and supported by the TG analysis in Section 3.2.

Figure 3.1 presents SEM images of as-received metal acetates powders. As seen in the images, gold and aluminum acetates appear as porous and irregular structures, while copper and palladium acetates appear as condensed and well-defined crystalline structures. The metal acetate samples here were sputter coated with a 15 nm Au-Pd

Table 3.1: Thermophysical properties of bulk condensed-phase materials relevant to the material synthesis systems studied. The majority of the properties were obtained from the CRC Handbook, unless noted otherwise.

Chemical formula	Name	Molecular weight (CAS #)	Reactant manufact. purity	Melting point [K][a]	Boiling point [K]	Vapor pressure [atm][b]	Density [g/cm^3]
			Reactants				
$Al(OH)(C_2H_3O_2)_2$	aluminum diacetate	162.163 [142-03-0]	Sigma-Ald. N/A	327	N/A	- -	1.74
$Au(C_2H_3O_2)_3$	gold (III) acetate	374.101 [not estb.]	Alfa Aesar, 99.9%	Decomposes at 423-433 K[c]		-	3.26[d]
$Cu(C_2H_3O_2)_2.H_2O$	Copper (II) acetate monohydrate	199.650 [6046-93-1]	Alfa Aesar, 99.999%	388	Decomposes at 513 K	-	1.88
$Pd(C_2H_3O_2)_2$	Palladium acetate	224.507 [3375-31-3]	Sigma-Ald., 98%	478	Decomposes at 480-570 K	-	3.00[e]
			Intermediate and product species				
Al	Aluminum	26.982 [7429-90-5]		933	2792	-	2.70
Al_2O_3	Alumina	101.961 [1344-28-1]		2326	3253	-	3.97
Au	Gold	196.967 [7440-57-5]		1337	3129	6.61 x 10^{-4}	19.3
Au_2O_3	Gold oxide	441.931 [1303-58-8]		Decomposes at 423 K		-	N/A
Cu	Copper	63.546 [7440-50-8]		1358	2868	4.38 x 10^{-3}	8.96
Cu_2O	Cuprous oxide	143.091 [1317-39-1]		1508	Decomposes at 2073 K	-	6.00
CuO	Cupric oxide, copper oxide	79.545 [1317-38-0]		1719	N/A	-	6.31
PdO	Palladium(II) oxide	122.42 [1314-08-5]		Decomposes at 1023 K		-	8.3
Sn	Tin	118.71 [7440-31-5]		504	2875	3.94 x 10^{-3}	7.27
SnO	Tin monoxide	134.709 [21651-19-4]		Decomposes at 1353 K		-	6.45
SnO_2	Tin dioxide tin(IV)oxide	150.709 [18282-10-5]		1903	N/A	-	6.85

[a] Metal acetate melting points are too close to the decomposition temperature to differentiate.
[b] at 2000 K.
[c] Estimated using visual melting tool (MEL-TEMP 3.0).
[d] As determined using a density analyzer (Micromeritics, AccuPyc 1330)
[e] Estimated density [65].

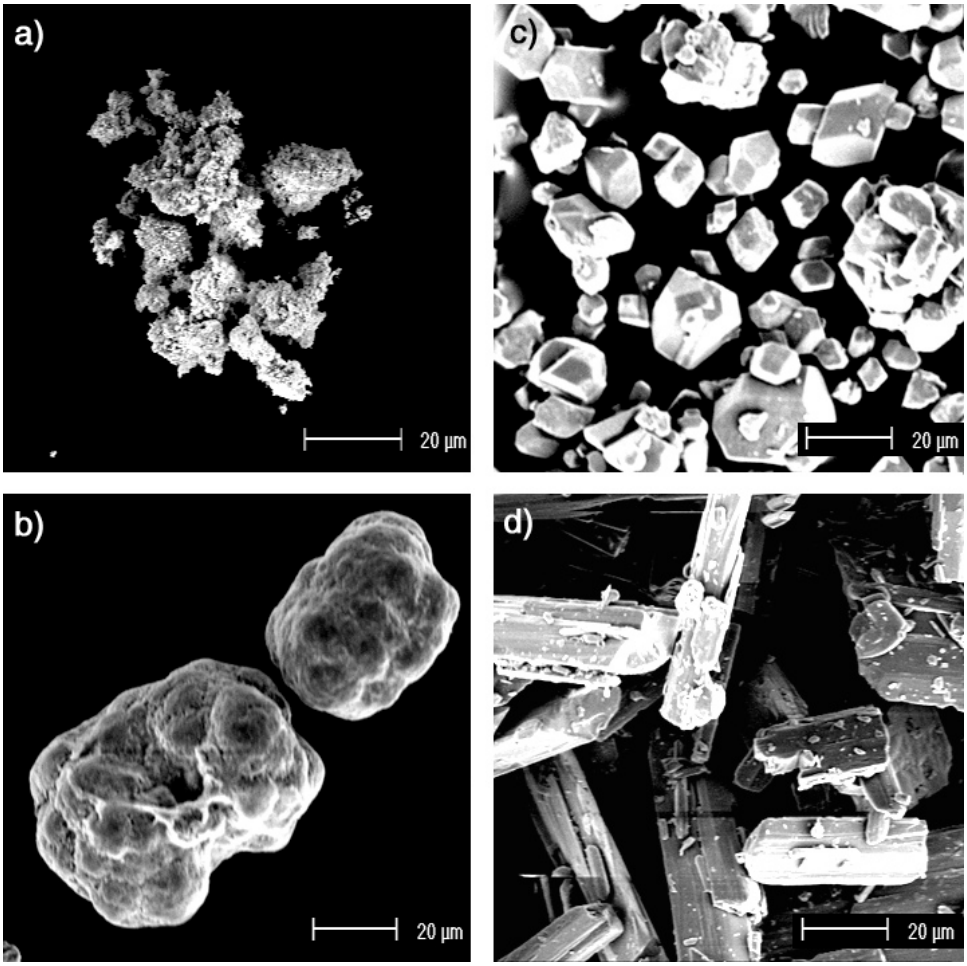

Figure 3.1: SEM images of as-received unreacted (a) gold acetate, (b) aluminum acetate, (c) copper acetate, and (d) palladium acetate particles.

layer on copper tape to achieve better contrast. Figure 3.2 presents a TEM image of gold acetate after the reactant powder had been sieved and transported through the PFS. As seen in the image, the irregular structure of the gold acetate particles is retained after processing through the PFS.

Typical XRD patterns of the as-received unreacted gold, aluminum, copper and palladium acetate powders are presented in Fig. 3.3. The corresponding reference diffraction patterns accompany the spectra. There are no standard reference patterns available for gold acetate in the JCPDS database [61] for comparison; however, Kristl *et al.* [66] provide an XRD scan obtained of gold acetate used in their study of

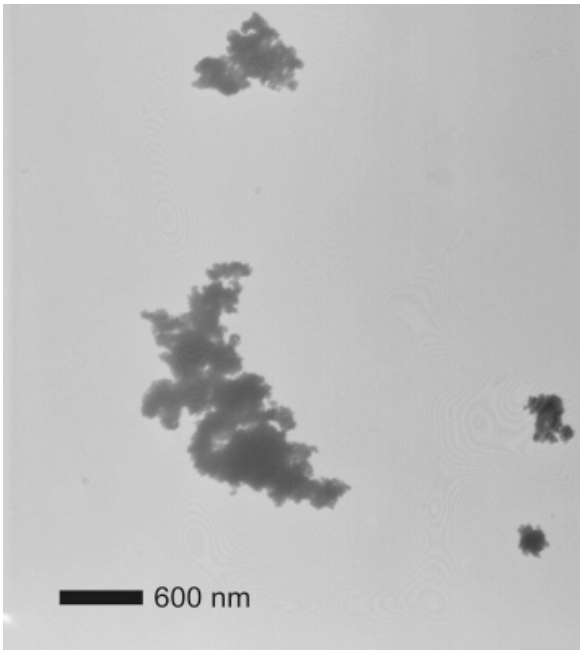

Figure 3.2: TEM image of unreacted gold acetate sampled at the secondary fuel tube exit with argon flow as the carrier gas.

sonochemical preparation of Au_2S_3. The XRD scan by Kristl *et al.* is provided in Fig. 3.3(a) for reference, and the two spectra agree well with respect to location of the peak features and relative intensities. Note the copper acetate spectra (see Fig. 3.3(c)) indicated the presence of both copper acetate (24-1126) and copper acetate hydrate (27-145) in the precursor powder.

Table 3.2 provides a summary of the average crystallite sizes determined from the metal acetate XRD spectra (d_{XRD}). High resolution XRD scans were used for the calculations, and the specific features used are indicated in the table. An average crystallite size for the palladium acetate is not provided due to the interference of multiple peaks at the index locations of interest. The crystallite sizes obtained from the metal acetate XRD spectra suggest the particles observed in the SEM images (Fig. 3.1) consist of crystallites approximately 12 nm in size for the aluminum acetate, 26 nm for the copper acetate and 160 nm for the gold acetate.

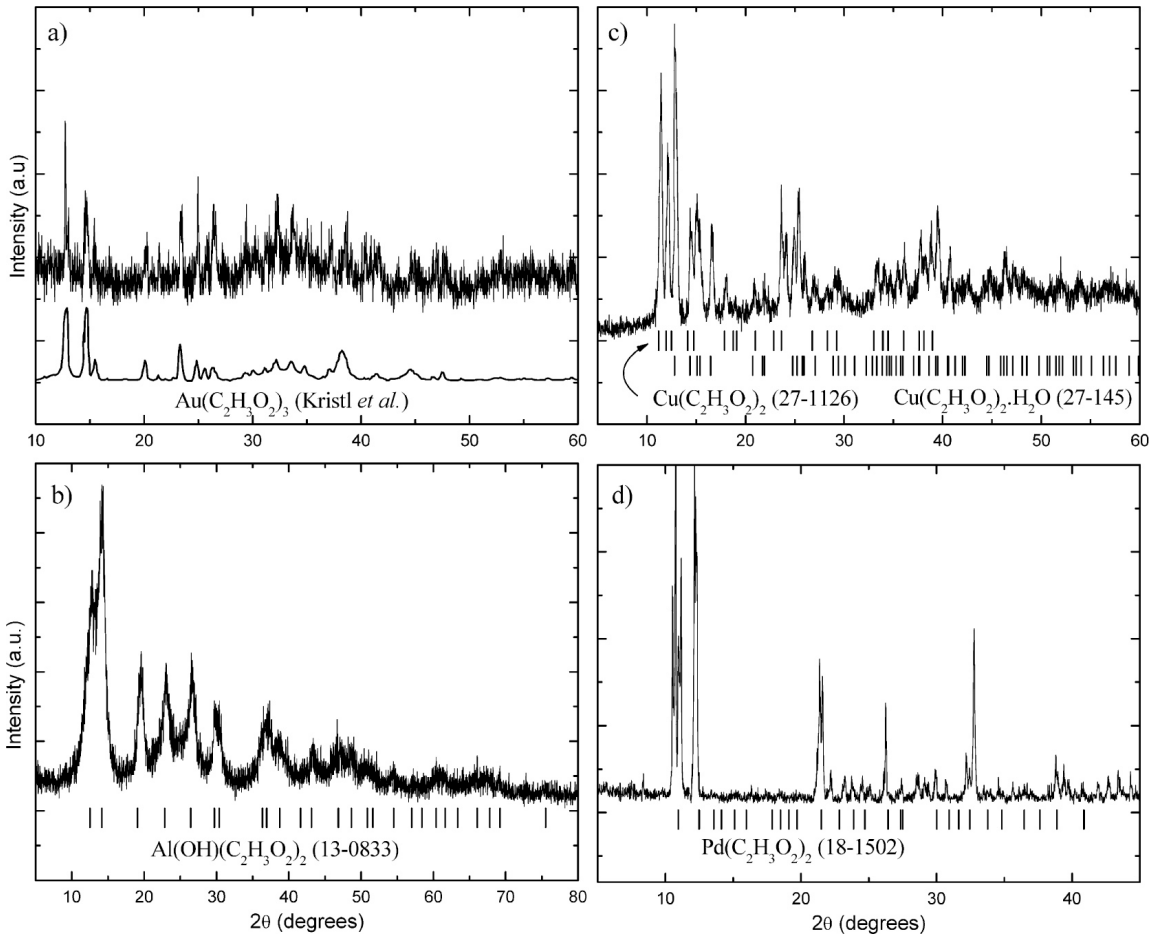

Figure 3.3: XRD spectra of as-received unreacted (a) gold acetate, (b) aluminum acetate, (c) copper acetate, and (d) palladium acetate.

3.1.2 The combustion synthesis environment

The experiments for this study were conducted without using the optical chimney with the gas flow rates provided in Section 2.1.1. Temperature profiles for the combustion synthesis system with and without the presence of the secondary flame are presented in Fig. 3.4 as a function of distance from the surface of the burner. No solid-phase precursors were used in these characterization studies. The thermocouple was located slightly off-center of the burner (see inset in Fig. 3.4) for both data sets. The presence of the TMT flame leads to higher temperatures throughout

the synthesis region encountered by the particles. Particle residence times based on the particle tracking using high speed imaging (Section 2.1.2) are presented in the inserts.

3.1.3 Characterization of particle evolution

The evolution of particle microstructure throughout the combustion synthesis environment was examined for the gold acetate/TMT system using particle sampling and *ex situ* imaging. The TEM samples were obtained by rapid insertion of the grids at increasing sampling heights above the burner surface, corresponding to longer residence times. The series of TEM images presented in Fig. 3.4 show the progressive formation and growth of the Au/SnO_2 nanocomposites. Gold particles are formed early in the system (5 ms) with relatively few discrete, small SnO_2 particles present. As the residence time increases, the frequency of appearance of the gold particles increases slightly; however, the gold particles are always sparsely located, and the gold is always in a spherical form. The tin oxide is initially present in infrequent, small clusters; the primary particles develop as the height increases; and a larger degree of agglomeration begins at approximately 3.5 cm above the burner.

The results of the semi-automated image analysis of the particle size distribution of the SnO_2 particles are presented in Fig. 3.4. Typical SnO_2 particle morphologies at the sampling locations are also provided in Fig. 3.4 for reference. The average SnO_2 particle size and the log-normal distribution are provided for each residence time and sampling height. As the residence time increases, the average particle size grows from approximately 7 nm to 13 nm and the log-normal distribution becomes more representative of the population as indicated by an increased quality of fit to the experimental data. Approximately 150 to 550 particles were counted at each

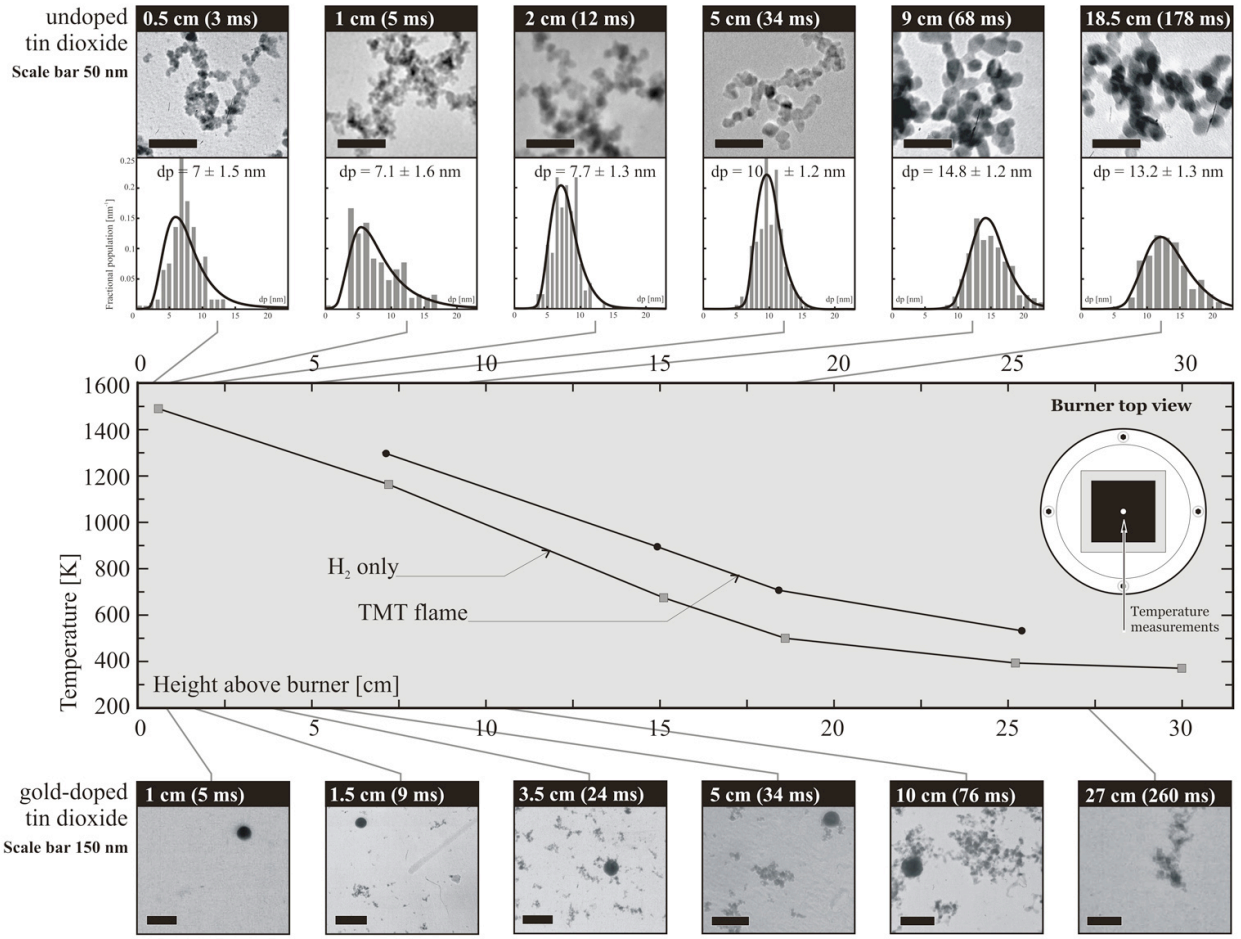

Figure 3.4: Temperature and particle imaging results as a function of height (h) above the burner surface (i.e., increasing residence time). The flame temperature data were obtained at a location approximately 2 mm from the centerline of the burner or 26 mm from the outer edge of the shroud region. The residence times are based on average velocities measured using high-speed imaging. The top panel of figures presents the tin dioxide particle morphology and primary particle size distributions as a function of height. The bottom panel of gures presents the evolution of the gold-SnO_2 nanocomposites.

height from multiple TEM images using the semi-automated image analysis described earlier (Section 2.3.2).

3.1.4 Characterization of final nanocomposite materials

The effects of the operating conditions and solid-phase reactants on the final product morphology (via TEM), average SnO_2 crystallite size (via XRD) and metal loading (via XEDS) are reported in detail in Miller *et al.* [58]. The results of that study are briefly summarized here for reference. The average SnO_2 crystallite size of the product powders could be increased or decreased compared to a baseline undoped SnO_2 synthesis condition using the additives and the burner operating conditions. Metal or metal oxide forms of the additives were created (as determined via XRD spectra) depending on the precursor used. For example, only metallic gold was identified from the XRD spectra of the nanocomposite materials made using gold acetate and TMT. Whereas, copper oxides were formed when copper acetate and TMT were used. A range of microstructures was observed from partial encapsulation of the metal additive within a layer of SnO_2 particles to mixed material systems.

Typical results for the microstructure of the nanocomposites produced using gold acetate and TMT are presented as an inset in Fig. 3.5. The darker larger particle in the image is gold, as identified using XEDS. Similar to gold acetate, copper acetate and palladium acetate produced metal additive particles that were readily identifiable by the size, crystalline structure and contrast in the TEM images (see [58] for examples).

XRD spectra of the Au/SnO_2 nanocomposites produced using gold acetate and tetramethyl tin are presented in Fig. 3.5. The XRD data demonstrate the SnO_2 is in the cassiterite phase and the gold is present in metallic form. XRD analyses of

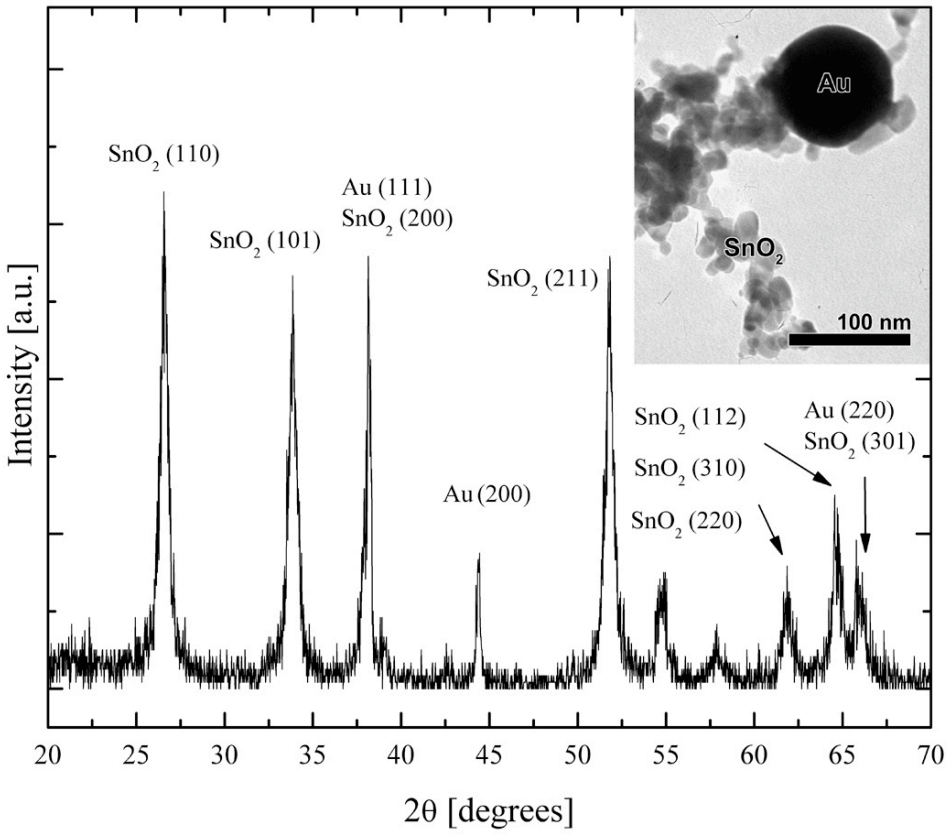

Figure 3.5: XRD spectra of Au-doped SnO_2 powder produced using gold acetate as the additive precursor. The features and lattice parameters associated with the cassiterite phase of SnO_2 (21-1250) and metallic gold (4-784) are indicated in the figure. The inset presents a typical TEM image of the nanocomposites. The larger high-contrast particle was identied as Au using TEM-XEDS.

the average crystallite size for the SnO_2 particles and how the SnO_2 is affected by the presence of the metal additives are presented in detail in Miller *et al.* [58]. XRD analyses of the metallic gold peaks conducted as part of the current work yielded an average particle size of 80 nm for the gold in the nanocomposites, which is in excellent agreement with the TEM imaging results conducted previously, where an average value of 83 nm was determined [58].

The aluminum acetate system was unusual compared to the other metal acetates, in that no metals or metal oxides (besides SnO_2) were identified in the XRD spectra. Additionally, it was very challenging to detect aluminum additives in the TEM im-

ages using contrast, crystalline structure or XEDS. After considerable analysis, some particles were identified as containing aluminum using XEDS. Such an example is presented in Fig. 3.6, where the particles identified as alumina (Al_2O_3) indexed to aluminum using XEDS and were assumed in an oxide form. The particles are noticeably smaller than the SnO_2 particles and appear highly fused. Semi-automated image analysis of Fig. 3.6 revealed average primary particle sizes of 11.9 $\pm$ 1.2 nm and 20.4 $\pm$ 1.2 nm for the alumina and tin dioxide particles, respectively.

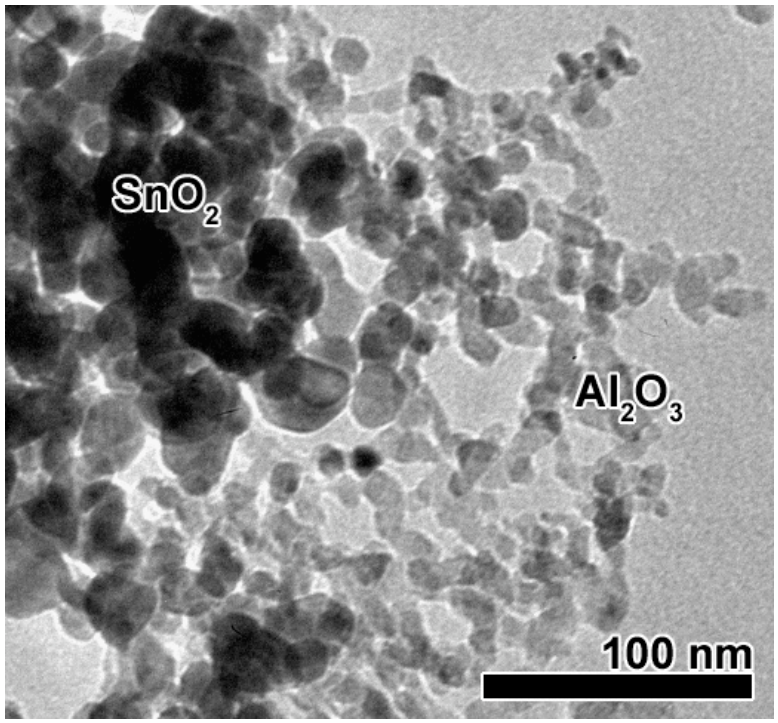

Figure 3.6: TEM image of Al-doped SnO_2 powder produced using aluminum acetate as the additive precursor. The smaller particles were identied as containing Al using TEM-XEDS and are assumed to be in an oxide form.

Note that although the TEM data indicate the presence of discrete metal additive particles, trace quantities of the metal additives may also be present within the SnO_2 particles, but below the detectable limits of TEM XEDS. For example, the work by Jain *et al.* [67] suggest it is possible for aluminum to be incorporated into SnO_2 crystals. The relatively high vapor pressures of the metals associated with the metal

acetates used in the study support this possibility. For example, Table 3.1 presents the melting and boiling points of the metal and metal oxide compounds that may be present in the systems studied. At the higher temperature regions of the reactor, close to the burner surface, most of the materials are above the bulk melting points. Table 3.1 also provides the vapor pressures at 2000 K of the pure metal species associated with the metal acetates considered. At the high temperatures found in the mixed-phase combustion system, the metal vapors can reach high concentrations with mole fractions on the order of 100s to 1000s of parts per million. These gas-phase species are highly mobile and likely to condense on existing nanoparticles as the temperatures in the reactor decrease.

3.1.5 Nanocomposite synthesis discussion

Solid-phase precursors can react in a variety of manners in a high-temperature environment. For example, the particles can decompose or explode, yielding reactive intermediates in the gas, solid or liquid phases; or the particles can burn in a fashion similar to coal particles where volatiles are emitted which combust first, followed by reaction with the remaining particle char. For metals, the burning process can entail gas-phase oxidation of evaporated metal, surface oxidation leading to a volatile or suboxide species, or surface oxidation leading to a non-volatile oxide deposit which may dissolve into the molten metal [68]. Combustion of pure metals has also been observed to be explosive, resulting in particle fragmentation and dispersion [69].

The experimental data obtained in the current work for the solid-phase metal acetates indicate the precursors rapidly decompose at the temperatures found in the combustion synthesis environment. Specifically, the presence of spherical gold particles at low sampling heights/short residence times (see Fig. 3.4) indicates the

conversion from solid-phase metal acetate to gold nanoparticle occurs in less than 5 ms. This has been further substantiated by the gold acetate decomposition study presented in Section 3.2. In addition, no gold aggregates or agglomerates were observed at any sampling location, demonstrating the sintering process between gold particles must occur virtually instantaneously. Indeed, calculations for the characteristic time for gold nanoparticle sintering, described in Bakrania *et al.* [70], yielded values below 100 μsec for regions near the surface of the burner, below 5 cm (discussed in methane-assisted study below - see Section 3.3).

Table 3.2: Comparison of average crystallite size based on XRD analyses of as-received metal acetates (d_{XRD}), predicted metal additive size based on Eqn. 3.1 (d_{Me}), and TEM-observed metal additive particle dimensions ($d_{p,TEM}$).

Precursor	2θ feature used with Eqn. 2.3 [^{o}]	d_{XRD} [nm]	Metal additive product	d_{Me} [nm]	$d_{p,TEM}$ [nm]
gold acetate $Au(C_2H_3O_2)_3$	15.4	160	gold, Au	63.4	83
aluminum acetate $Al(OH)(C_2H_3O_2)_2$	19.6	12	aluminum oxide Al_2O_3	9.8	12
copper acetate	11.4 $Cu(C_2H_3O_2)_2$ 12.9 $Cu(C_2H_3O_2)_2.H_2O$	26*	copper oxide	12.8 (CuO) 19.9 (Cu_2O)	50

* Average based on the anhydrate and hydrated copper acetate

The Au particles produced in the nanocomposite system can be compared with the gold acetate precursor as a means to determine if there is a relationship between the parent and child materials. Such a connection, if it exists, would be valuable for predicting nanocomposite morphology. Assuming spherical particles, the size of the gold particle (the child particle) is related to the gold acetate (the parent particle) via

$$d_{Me} = \left(N \frac{\rho_{MeAc}}{\rho_{Me}} \frac{MW_{Me}}{MW_{MeAc}} \right)^{1/3} d_{MeAc} \tag{3.1}$$

where N is the molar conversion factor, ρ is density and MW is molecular weight. The subscripts Me correspond to metal and $MeAc$ correspond to metal acetate. Using the densities and molecular weights listed in Table 3.1 for gold and gold acetate and assuming a one-to-one molar conversion rate, Eqn. 3.1 yields $d_{Au} = 0.45 d_{AuAc}$. Recall an average gold particle size of $d_{Au} = 83$ nm was determined based on the Au size distribution measured from the TEM images [58]. When Eqn. 3.1 is used to estimate the characteristic dimension required for gold acetate to directly form 83 nm diameter particles, a value of $d_{AuAc} = 186$ nm is determined. This value is very close to the average crystallite size of 160 nm determined using XRD of the gold acetate.

Using the average crystallite size from the XRD analysis of the solid-phase reactants and the appropriate data from Table 3.2, Eqn. 3.1 can be applied to determine the size of metal particles in nanocomposite materials produced using the aluminum acetate and copper acetate precursors. Table 3.2 provides the metal particle dimensions for the aluminum and copper systems for the appropriate molar conversions from the precursor crystallite sizes (d_{XRD}). TEM images of aluminum and copper acetate products indicate typical particle sizes ($d_{p,TEM}$) of approximately 12 and 50 nm for alumina and copper oxide, respectively. Note, the TEM values are biased to larger sizes (smaller particles are more convolved with SnO_2 particles and therefore more difficult to identify), and because the additives are sparsely located in the TEM images, the size estimates have high uncertainties. There is good correlation between the metal particle sizes (d_{Me}) and the measured dimensions ($d_{p,TEM}$) for the gold and aluminum acetates, while there is over a factor of 2 difference for the copper acetate. The discrepancy may be due to different physical decomposition mechanisms for the metal acetates. Specifically, the porous precursor materials, such as gold acetate,

undergo additional particle fragmentation which does not occur for the solid-phase reactants with limited porosity (see Section 3.2).

The SEM images of the metal acetates show remarkable differences in the structures of the materials. Combined with the data of Table 3.1, the results indicate morphological differences in the precursor materials may affect the final metal additive dimensions, particularly for gold and aluminum acetate which exhibit appreciable porosity. The porous structure supports the theory that the acetate particles can fragment, potentially along grain boundaries, due to increased pressure within the pores as the metal acetate vaporizes and decomposes. The metal atoms nucleate locally, and these nanoparticles undergo collision to form aggregates and agglomerates. If the sintering rates are high, as is the case for gold nanoparticles, spherical particles are formed with dimensions on the order of the grain size of the gold acetate. Figure 3.7 presents a schematic representing the steps of metal acetate decomposition and metal particle formation suggested by the results for the porous materials. Here gold acetate decomposition to yield gold nanoparticles is used as a model system to represent the particle evolution. When the copper and palladium acetates vaporize and decompose, these denser structures may not fragment along grain dimensions. Without the additional fragmentation, neighboring grains can coalesce to form larger particles as observed in the TEM images [58]. The fragmentation process in gold acetate is investigated further in Section 3.2.

A schematic integrating the gold acetate and TMT systems during the formation of nanocomposites is presented in Fig. 3.8, where the early gold acetate decomposition processes are omitted for clarity. The presence of the metal additives can affect the tin dioxide formation and growth processes in a variety of complex ways. The metals can induce significant new reaction pathways via homogeneous and heteroge-

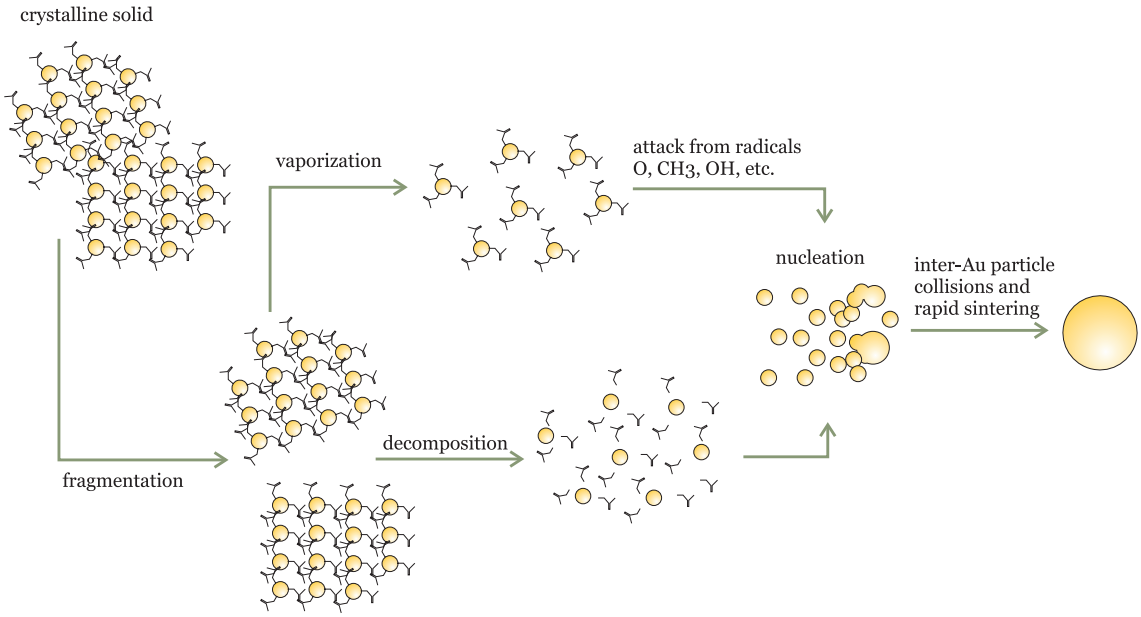

Figure 3.7: Schematic of the decomposition of gold acetate and subsequent formation of gold nanoparticles.

neous catalysis. The temperature and flow fields can be considerably altered when the additive precursors are introduced. The metal additives can modify the SnO_2 grain growth kinetics and provide sites for heterogeneous deposition and SnO_2 particle growth. Based on the results of the current study, the spherical gold nanoparticles are presumed to interact with SnO_2 primarily through interparticle collision and aggregation and as sites for surface growth. The coalescence of SnO_2 is slower compared to gold resulting in the aggregated structures seen in TEM images. Further evidence for this process is provided in Section 3.3.

3.1.6 Nanocomposite synthesis conclusions

Controlling nanocomposite morphology is a vital step towards designing new and advanced optical, semiconductor, catalyst and sensor materials. In particular, encapsulation of metals has yielded remarkable photonic properties. Combustion synthesis

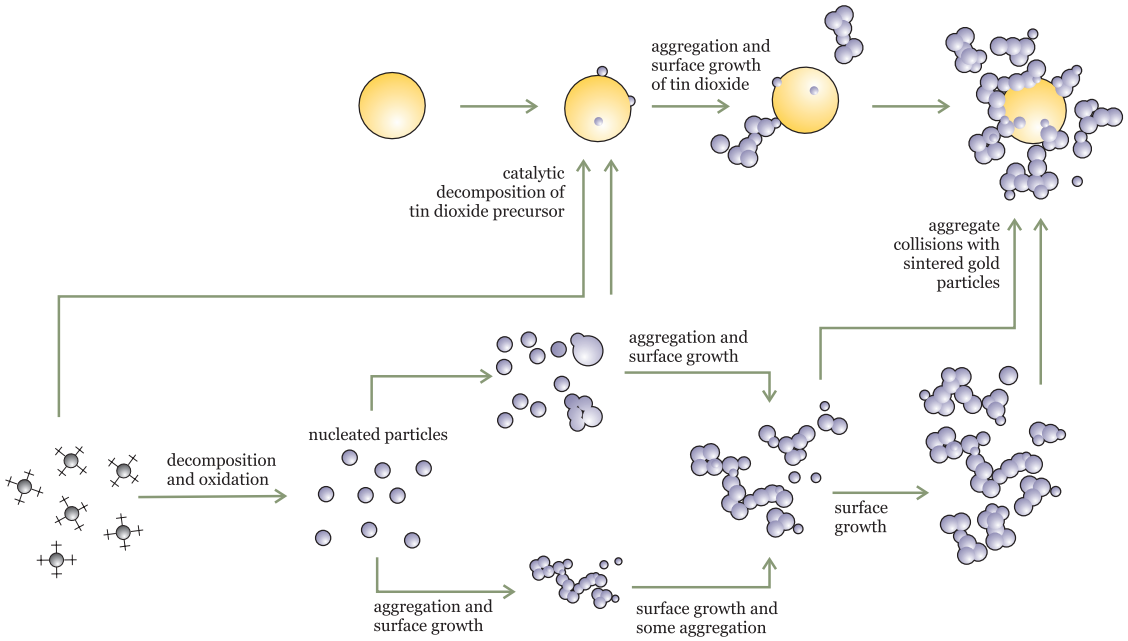

Figure 3.8: Schematic of the formation of nanocomposite Au/SnO_2 materials from mixed solid-phase gold acetate and gas-phase tetramethyltin reactants.

methods offer the potential to produce such high-value-per-gram materials at high rates with good control of the nanocomposite properties. The results of the current work indicate that metal acetates provide an excellent source for metal additives in flame synthesis environments. Metal acetates can also provide access to nanosized additives, where the approximate dimension of the metal additive can be predicted using the grain size of the parent material. The formation of nanodimensioned metals, the ease of handling, low toxicity, and relatively low cost of metal acetates point towards a promising new scope in the synthesis of nanocomposite materials.

3.2 Gold acetate thermal decomposition

The study of gold acetate thermal decomposition was conducted to clarify our understanding of the decomposition processes suggested in Fig. 3.7. This effort

focuses on identifying the mechanisms important during thermal decomposition of metal acetates in an oxidizing environment. The results of this study have relevance not only to combustion synthesis but to pyrolysis and oxidation synthesis methods as well, which use metal acetates as reactant precursors, and to synthesis methods which use solid-phase organometallic precursors for generating nanoparticles [71, 72]. One of the major objectives of the investigation was to evaluate if there is a direct relationship between the average crystallite size of the metal acetate and the resulting metal nanoparticles produced, as suggested previously by Eqn. 3.1. Gold acetate was selected for the study due to the importance of gold nanoparticles in many advanced optical, electrical and catalytic applications and the strong dependence of material performance on the size of the gold nanoparticles [73, 74, 75, 76]. In particular, the experiments were designed to elucidate the early steps in the synthesis process, when metal acetate particle decomposition occurs. The initial steps in this process are critical in determining the characteristics of the final product nanoparticles. The bulk of this work as been submitted to the *Journal of Thermal Analysis and Calorimetry* for publishing.

3.2.1 Characteristic particle size and morphology

Representative XRD patterns of the as-received gold acetate and heated gold acetate samples are presented in Fig. 3.9. As noted earlier, JCPDS database does not have a reference pattern for gold acetate. Consequently, the XRD spectra for gold acetate reported by Kristl and Drofenik [66] is provided in the figure as a basis for comparison. As seen in the figure, the XRD pattern for the gold acetate used in this work is consistent with the previous XRD pattern for gold acetate documented in the literature; however, each spectra indicate some gold impurities (e.g. the features

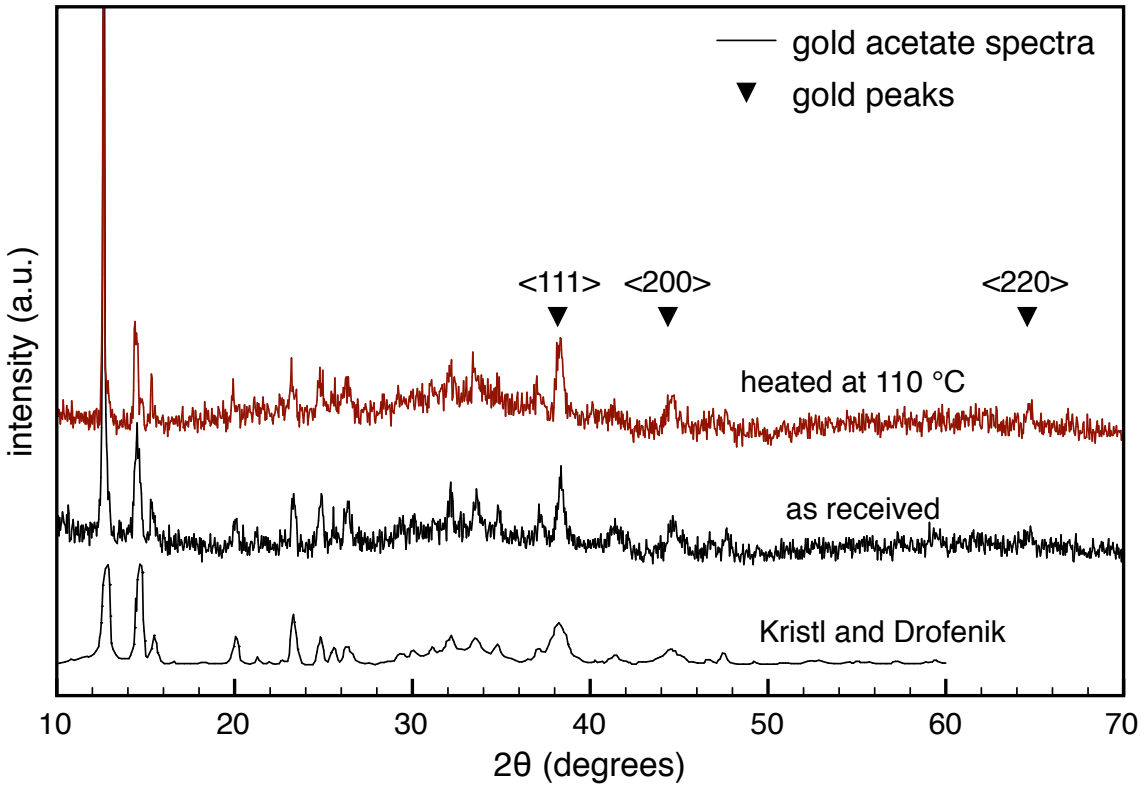

Figure 3.9: Typical x-ray diffraction patterns of as-received (light brown in color) and heated (dark brown) gold acetate powders. A reference XRD pattern presented in Kristl and Drofenik for gold acetate and the JCPDS reference for metallic gold are provided for comparison (▼).

at $2\theta = 38.17^o$ and 44.37^o). The heated gold acetate spectra was used to determine if the gold impurity was from partial decomposition of gold acetate. The degree of decomposition can be discerned by evaluating the gold $\langle 111 \rangle$ peak intensity relative to the gold acetate peak intensity of the feature at approximately $2\theta = 14.5^o$ for the as-received and heated gold acetate powders. A comparison of the difference in peak intensities normalized by the gold acetate peak height indicates greater presence of gold in the heated sample ($(I_{goldacetate} - I_{gold})/I_{goldacetate} = 0.11$) compared to the as-received powders ($(I_{goldacetate} - I_{gold})/I_{goldacetate} = 0.43$); suggesting greater degree of decomposition has occurred in the heated sample. This experiment also yielded

a change in color from light brown (for the as-received powders) to dark brown (for the heated gold acetate powders). As a consequence, we conclude that darker gold acetate powders are more partially decomposed than the light brown powders. This result validates the earlier study to determine decomposition temperature visually by observing the change in color of the reactant powder (Section 3.1).

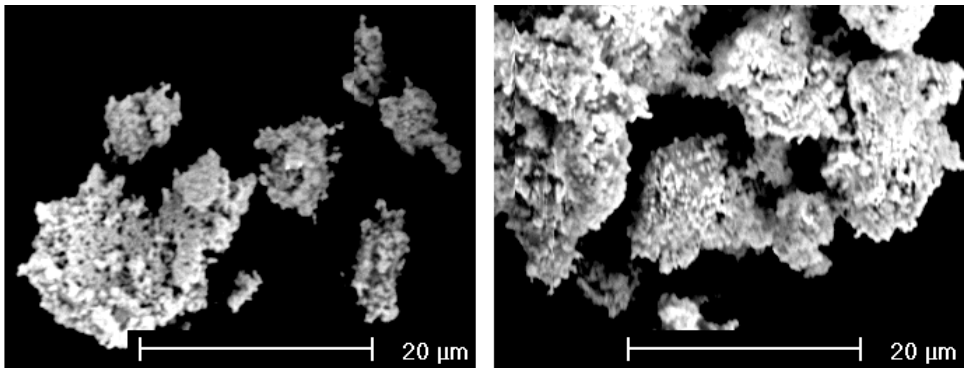

Figure 3.10: SEM images of as-received gold acetate powder.

Figure 3.10 shows SEM images of the as-received gold acetate powders. The images show the powders have a highly porous structure formed by finer grains that are less than 1 μm in size. XRD Scherrer analysis of the as-received light brown powders yielded an average crystallite size of 160 nm for the gold acetate used in this study.

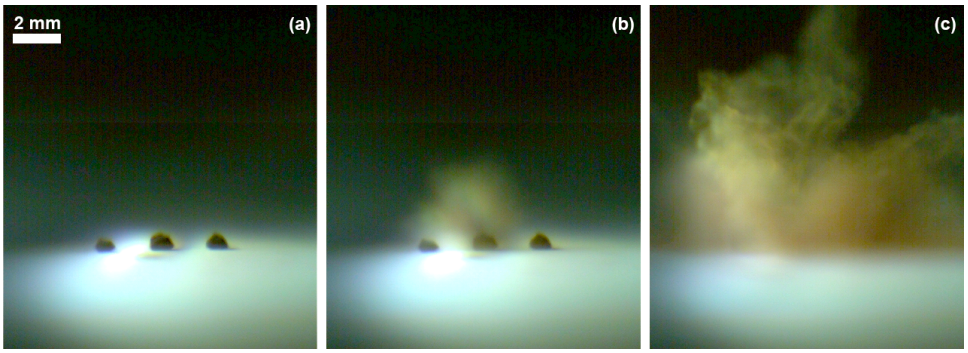

Figure 3.11: Typical imaging sequence showing the progression of gold acetate particle decomposition and fragmentation after heating at 25 ^{o}C/min was initiated at t = 0 min: (a) t = 0 min., (b) t = ~4 min., (c) t = 4 min 0.2 ms.

As described in Section 3.2, gold acetate particles were rapidly heated on a hot plate to achieve thermal decomposition. Figure 3.11 presents a typical imaging sequence of the gold acetate decomposition and fragmentation process that occurred during each hot plate experiment. The first panel of Figure 3.11 shows three gold acetate particles on the hot plate at the start of the experiment. The second panel shows the initial asymmetric fragmentation of the center gold acetate particle. A sharp cracking sound was also heard at this time. Figure 3.11(c) shows the formation of a nebula of particle fragments that occurred a fraction of a second ($\Delta t = 208$ μsec) after the first decomposition event. The decomposition temperature, defined as the temperature of the hot plate when the particles fragmented, was 103 ^{o}C with an uncertainty of $\pm$ 20 ^{o}C (based on the standard deviation of multiple experiments). Although not apparent in the images in Figure 3.11, the gold acetate particles also changed in color from light brown to dark brown/black before fragmentation was observed. After the experiments had concluded, pink streaks forming fairly uniform radial patterns of nanosized metallic gold were identified on the hot plate.

As noted earlier, samples of the particles ejected during decomposition were acquired at various locations near the hot plate by direct deposition onto TEM grids. In order to estimate the residence time of the particles sampled, a radial particle ejection velocity was calculated from the high-speed imaging sequence based on the evolution of the particle plume relative to the center of the gold acetate particle. The average minimum initial particle ejection velocity was 14 m/s. This average ejection velocity yields a residence time of 0.14 ms for a grid located 2 mm from the center of the source particle.

TEM images of the particle fragments collected during decomposition revealed generally spherical nanoparticles dispersed non-uniformly on the grids. All the par-

ticles present on the grid were identified as metallic gold using x-ray energy dispersive spectroscopy. A typical TEM image of particles sampled at 1 mm is provided in Fig. 3.12(a). There were two categories of particles observed in the TEM imaging as seen in Fig. 3.12(a): discrete spherical particles and more densely co-located particles which often appear partially coalesced (circled features). Figures 3.12(b) and 3.12(c) show examples of two such clusters captured from two separate grids located 1 mm from the initial gold acetate particles. Grid samples collected at 4 mm did not produce such cluster patterns. Instead much larger (with diameters ranging from 50 to 100 nm) and highly dispersed spherical gold particles were observed, such as shown in Fig. 3.12(d). Fast sintering rates are clearly present in this system, as samples obtained at 4 mm were dominated almost exclusively by large coalesced particles.

The TEM images were analyzed to determine the characteristic features of the gold fragment particles. Figure 3.13 shows an example of the image analysis performed on a gold cluster. In particular, the area of individual particles and cluster projected areas (defined as the total area of co-located and clustered fragmented particles) were measured from the images. The areas of the particles were used to determine the characteristic diameters of the discrete spherical particles, the diameters of the particles co-located within a cluster and the equivalent diameter that would be obtained if all the particles located in a cluster were coalesced. All image analysis assumed spherical particles. Analysis conducted on two grids sampled at 1 mm and 2 mm (obtained from two experiments) yielded coalesced sphere diameters of 140 ± 65 nm and 171 ± 54 nm, respectively. Here, the uncertainties represent the standard deviation in the particles analyzed. Individual particles in the clusters had diameters in the range of 5-10 nm. TEM images of the discrete spherical particles that were not part of the clusters yielded average diameters of 12.8 ± 4.9 nm.

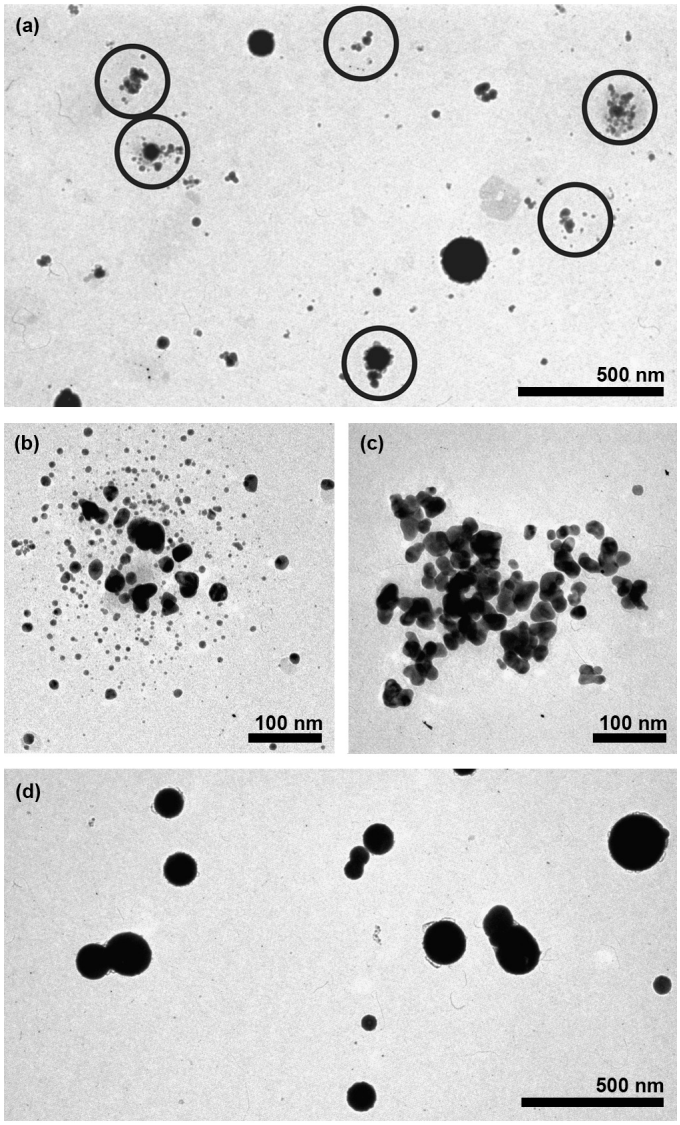

Figure 3.12: TEM images of gold nanoparticles captured during gold acetate fragmentation. (a) Typical gold nanoparticles sampled at 1 mm (b, c) Typical partially coalesced gold clusters sampled at 1 mm from two experiments (d) coalesced gold nanoparticles sampled at 4 mm.

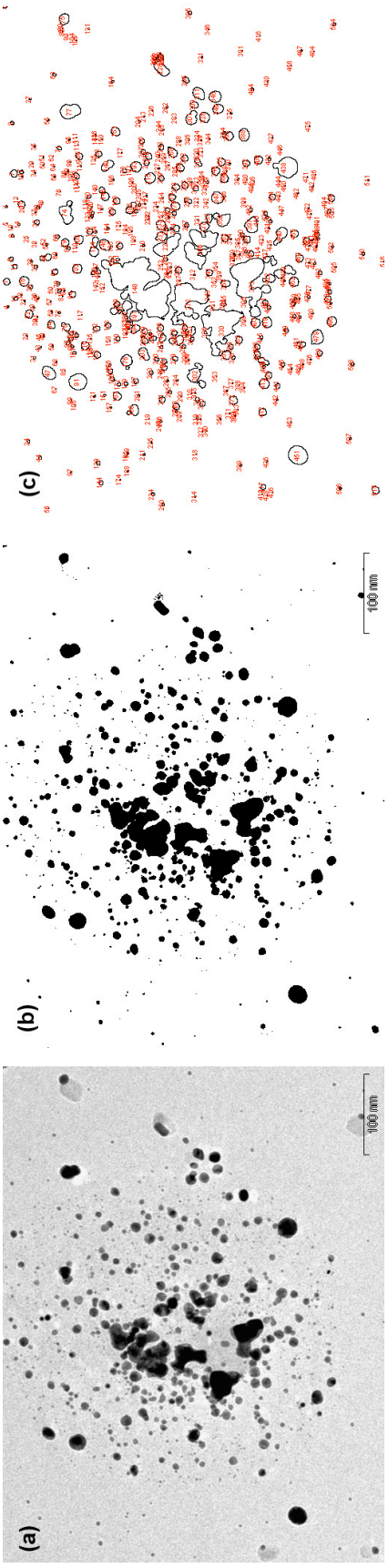

Figure 3.13: A sequence of images demonstrating the imageJ analysis performed. (a) original TEM image (b) after thresholding (c) indexed and processed to evaluate particle areas.

The TEM data can be compared to the characteristic dimensions of the unreacted gold acetate powders, where d_{XRD} = 160 nm, to develop an understanding of the effects of the decomposition process on the gold nanoparticles produced. Our hypothesis, initially proposed in Bakrania *et al.* [63] (also in Section 3.1), is that the gold acetate crystallite grains are direct precursors to the initial gold particles formed and the crystallite grain dimensions therefore dictate the minimum dimension of the gold nanoparticles. The results of this work provide further data to consider this theory. Accounting for the molecular weight and density of gold acetate and gold, assuming complete conversion of gold acetate to metallic gold (using Eqn. 3.1) and assuming the gold acetate fragments along crystallite grains, the average crystallite size of 160 nm would yield spherical gold particles with an average diameter of 63 nm. This average is between the characteristic sizes determined for the larger coalesced particles (140 nm ± 65 nm) and the smaller discrete particles (12.8 nm ± 4.9 nm). While the results do not isolate a unique decomposition pathway, the results do point toward a relationship between the average crystallite size of the metal acetate reactant and the resulting metal nanoparticles.

Figure 3.14 presents a schematic of a decomposition mechanism based on the hypothesis described above and which is consistent with the experimental data observed in this study. Initially, heating causes discoloration of the particles indicating relatively slow gold acetate decomposition. This is rapidly followed by the explosive fragmentation stage, where fragments with a range of sizes (on the order of 160 nm) are ejected. The decomposition of metal acetates is typically highly exothermic [65, 77, 78]. These fragments can potentially be at much higher temperatures than the decomposition temperature of 100 ^{o}C. The fragments form clouds of gold particles and vapor phase gold. Differences in the size of the clouds and the number density

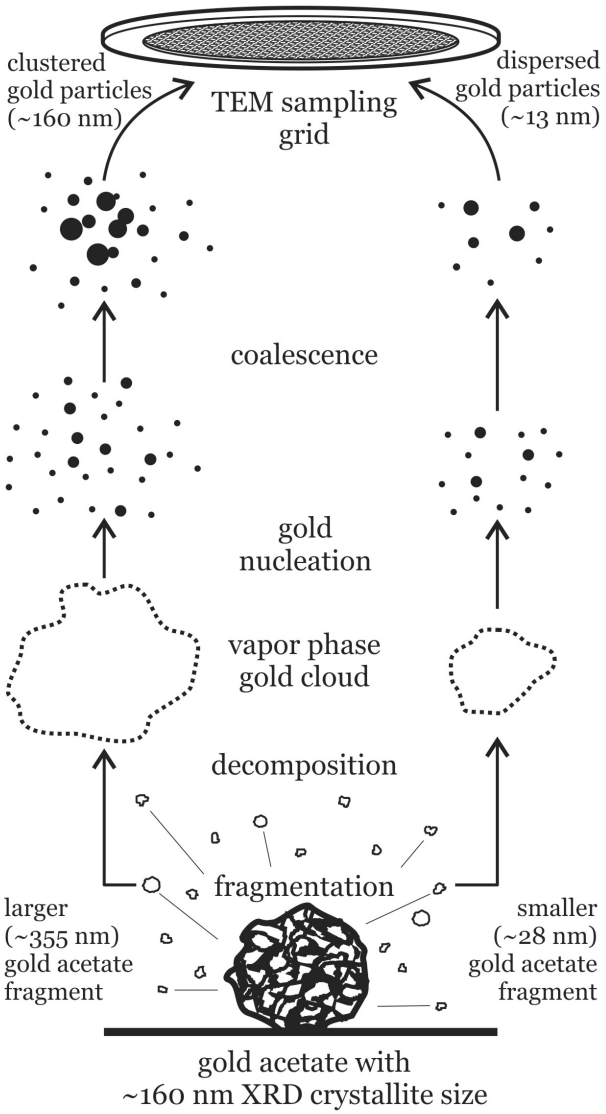

Figure 3.14: Schematic of proposed gold acetate decomposition and gold particle formation mechanisms under rapid heating.

of gold affect the number of initial nucleation sites present within the cloud. Given similar residence times (∼0.14 ms in the current study), higher number densities will yield more nucleation sites and higher interparticle collision frequencies than lower number densities. Consequently, more dense fragment clouds will yield more gold particles and larger gold particles (assuming rapid coalescence rates), such as shown in the reaction pathway on the left side of Fig. 3.14. Less dense clouds of particle fragments will form smaller and more discrete spherical particles, as shown in the reaction pathway on the right of Fig. 3.14. A range of initial particle fragment sizes is expected as the XRD data represent an average crystallite dimension. The rates of interparticle collision and coalescence dictate the final size of the gold nanoparticles.

3.2.2 Decomposition temperature

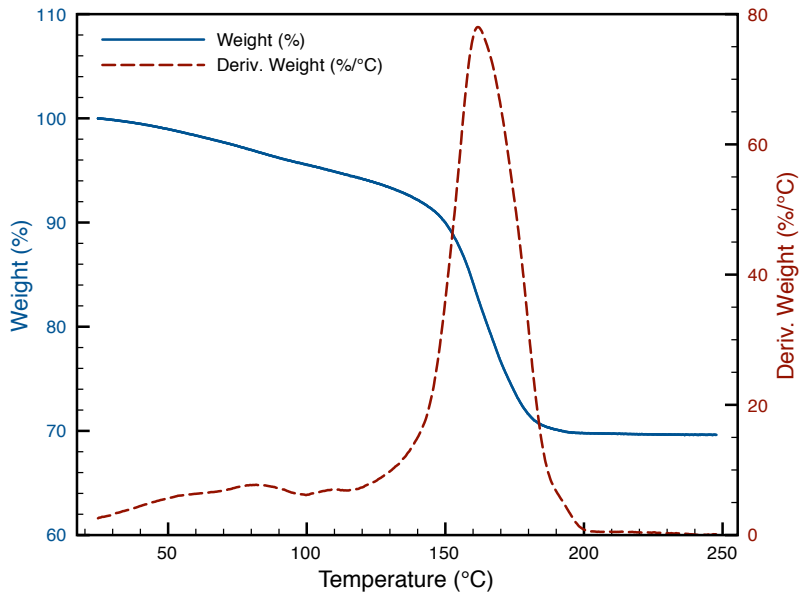

Figure 3.15: TG results for heating gold acetate in nitrogen at a rate of 5 ^{o}C/min.

Figure 3.15 presents the thermogravimetric (TG) data for gold acetate mass loss under heating and the derivative of the percent weight loss with respect to temper-

ature. Significant mass loss was observed between 120 - 210 ^{o}C, with an average peak mass rate of loss occurring at T = 170 ^{o}C. Although the decomposition temperature measured during the hot plate experiments (103 ^{o}C $\pm$ 20 ^{o}C) was at a significantly different heating rate, the decomposition temperature is comparable to results obtained from the TG peak decomposition temperature.

The TGA decomposition temperature for gold acetate agrees relatively well with other metal acetate thermal analysis such as palladium and copper acetate [65, 77, 79]. Such studies have suggested acetic acid is the dominant organic by-product when decomposition yields a pure metal. Note, the weight loss observed in these TG experiments was lower than expected; which is consistent with some partial decomposition of the powders prior to the analysis.

3.2.3 Gold acetate decomposition study conclusions

This work provides the first documentation of the dramatic particle fragmentation process that occurs during heating of gold acetate in air. Measurements of the gold acetate decomposition temperature are in reasonable agreement and are consistent with expectations for metal acetates. The results of materials analysis supports that there is a relationship between the gold acetate crystallite size and the metal nanoparticles produced. Solid-phase metal-acetate precursors have tremendous potential to expand the composition and architecture of nanomaterials. This work provides key insights into the physical and chemical decomposition pathways (previously suggested in Fig. 3.7) that are important during decomposition of gold acetate and provides quantitative data that are critical for refining existing and developing new synthesis applications.

3.3 Methane-assisted synthesis

High-aspect ratio, single crystal structure, doped and undoped SnO_2 can dramatically enhance sensor properties. This work explores a new degree of control over the reaction environment in order to create a broad range of crystalline SnO_2 structures using combustion synthesis. Here, a hydrocarbon fuel is used as the carrier gas for the solid-phase precursors for the metal additives instead of the inert carrier gas used previously. As a result, the thermal, chemical and flow characteristics experienced by the particles are significantly altered to obtain highly faceted single crystal structure SnO_2 particles. A simple model for reaction, coagulation and coalescence is applied to understand the nanocomposite formation. The simplified model, based on characteristic times, is also used to explain the morphologies observed.

3.3.1 Pure SnO_2 synthesis

Two systems were considered in this study: the unassisted synthesis system and methane-assisted combustion synthesis (MACS). The unassisted system used argon as the carrier gas through particle feed system while the MACS system used methane as the carrier gas through the particle feed system. This resulted in a blue methane flame surrounding the yellow TMT flame for the MACS system. The details of the experimental setup are presented in Section 2.1.

Typical TEM images of undoped SnO_2 particles created using the two systems are provided in Fig. 3.16. Each grid was sampled at a height of 37 cm above the exit plane of the central fuel tube. As seen in the images, the SnO_2 particles typically form aggregated structures, with smaller discrete particles also present. The small individual particles are attributed to materials, located in the outer region of the

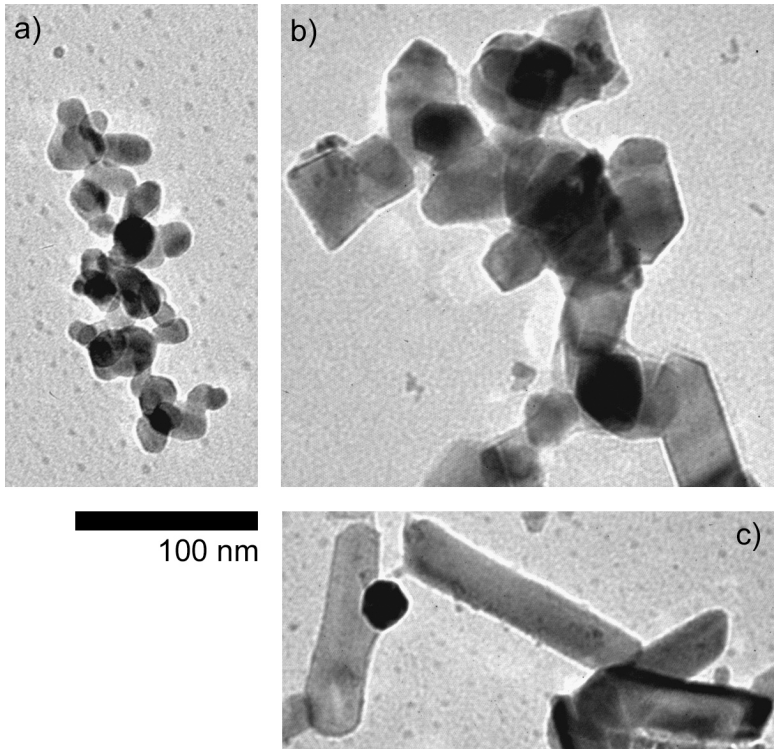

Figure 3.16: TEM images of undoped SnO_2 particles created using: (a) the unassisted system and (b, c) the methane-assisted system (MACS).

flow, deposited during the transit of the TEM grid through the co-annular region. The larger structures are attributed to particles formed near the centerline of the burner and experience longer residence times at high temperatures. It is evident that the MACS aggregates exhibit primary particles which are larger and highly faceted compared to the unassisted system. A remarkable feature of the MACS samples is the presence of long crystals (Fig. 3.16c). Semi-automated image analysis of the primary particles yields an average particle size of $d_p = 18.8 \pm 5.6$ nm for the unassisted system and $d_p = 49.9 \pm 18.6$ nm for the MACS system. High-resolution TEM of the MACS powders indicates the primary particles are single crystals (see Fig. 3.17). Image analysis of a limited number of the MACS SnO_2 nanocrystallites indicates an average aspect ratio of 2.6 ± 0.9, with a maximum aspect ratio of 5.4.

All features of the XRD spectra of the bulk samples of the MACS and the unas-

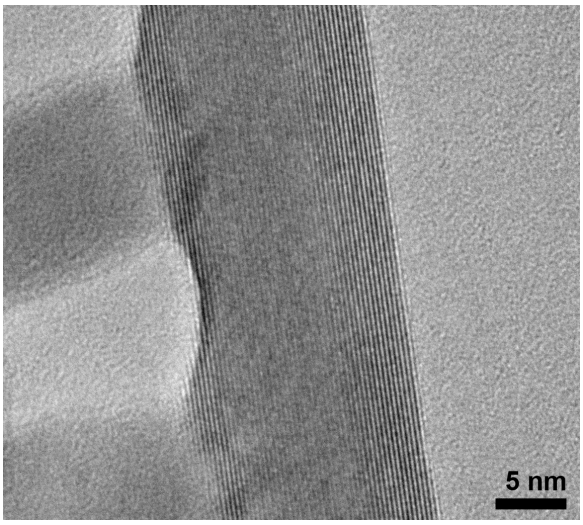

Figure 3.17: High resolution TEM image of high aspect ratio tin dioxide single crystal primary particle produced in methane-assisted system (MACS).

sisted powders index to the cassiterite phase of SnO_2. Figure 3.18 presents the corresponding XRD spectra of the $\langle 110 \rangle$ SnO_2 peak of two representative samples. Note the clear indication of larger crystallite dimensions associated the MACS particles as indicated by the more narrow line width. Scherrer analysis of the MACS particles yields an average crystallite size of 21.9 $\pm$ 3.3 nm while analysis of the unassisted flame generated particles yields an average crystallite size of 12.6 $\pm$ 1.9 nm. The XRD results are in good agreement with the TEM imaging analysis of the unassisted system particles. Note that the TEM data are based on measurements of the primary particles present in the aggregates and do not include the contributions of the discrete unaggregated particles. Consequently, the TEM results for average particle size are larger than the XRD data which include the effects of the smaller particles. Quantitative agreement between the TEM and XRD analyses of the MACS particles is not expected, as the TEM image analysis assumes a sphere of the same diameter as the longest dimension of the crystal. Due to the high aspect ratio of the particles, this approximation will also overestimate the average particle

size. Measurement of the crystallite dimensions from TEM for direct comparison with XRD requires identification of the specific lattice planes in the TEM images. This typically would require high-resolution TEM (such as Fig. 3.17) to obtain the indices followed by size measurements. Achieving a statistically meaningful sample is challenging using such a procedure.

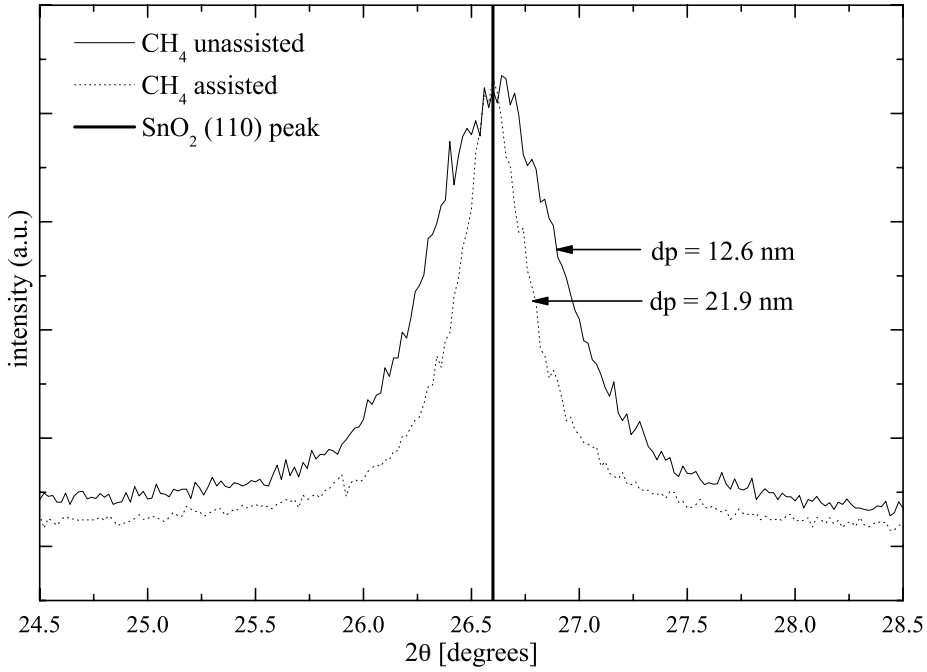

Figure 3.18: Comparison of XRD spectra of undoped SnO_2 powders sampled at 50 cm for MACS and unassisted synthesis conditions. Corresponding Scherrer peak analysis for average crystallite size are provided

Figure 3.19 presents an image of the MACS flame structure with blue methane flame enveloping the yellow TMT flame. Figure 3.20 presents the variation in particle morphology for the MACS system as a function of height along the centerline of the co-annular TMT-methane flames. Notice in Fig. 3.19 that the methane diffusion flame surrounds the TMT flame where the majority of the particle formation processes take place. As seen in Fig. 3.20 TEM images, aggregates form early, near the

surface of the burner. The average size for the primary particles in the aggregates based on image analysis is provided below each TEM image. The data show an increase in d_p as a function of height due to surface growth and sintering. Primary particles in the aggregates at lower heights are noticeably irregular. The changes in morphology along the flame axis are qualitatively similar to those observed in the unassisted system (see Section 3.1), where aggregates form rapidly near the surface of the burner and grow through collision, sintering and surface growth mechanisms. However, the MACS particles are much more faceted in nature and have higher aspect ratios throughout the residence time in the reactor compared to the unassisted particles, consistent with end-product images presented in Fig. 3.16.

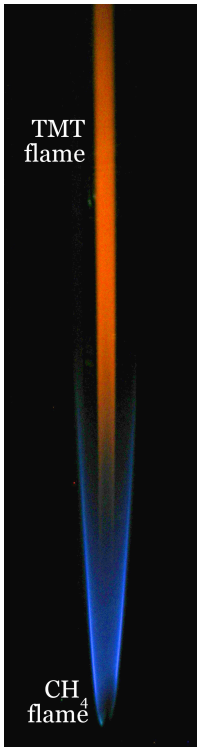

Figure 3.19: An image of the methane-assisted combustion synthesis flame structure with the blue methane flame enveloping the yellow TMT flame.

Thermocouple and PIV results for the MACS and the unassisted system were obtained at several heights above the burner surface. The velocity and temperature

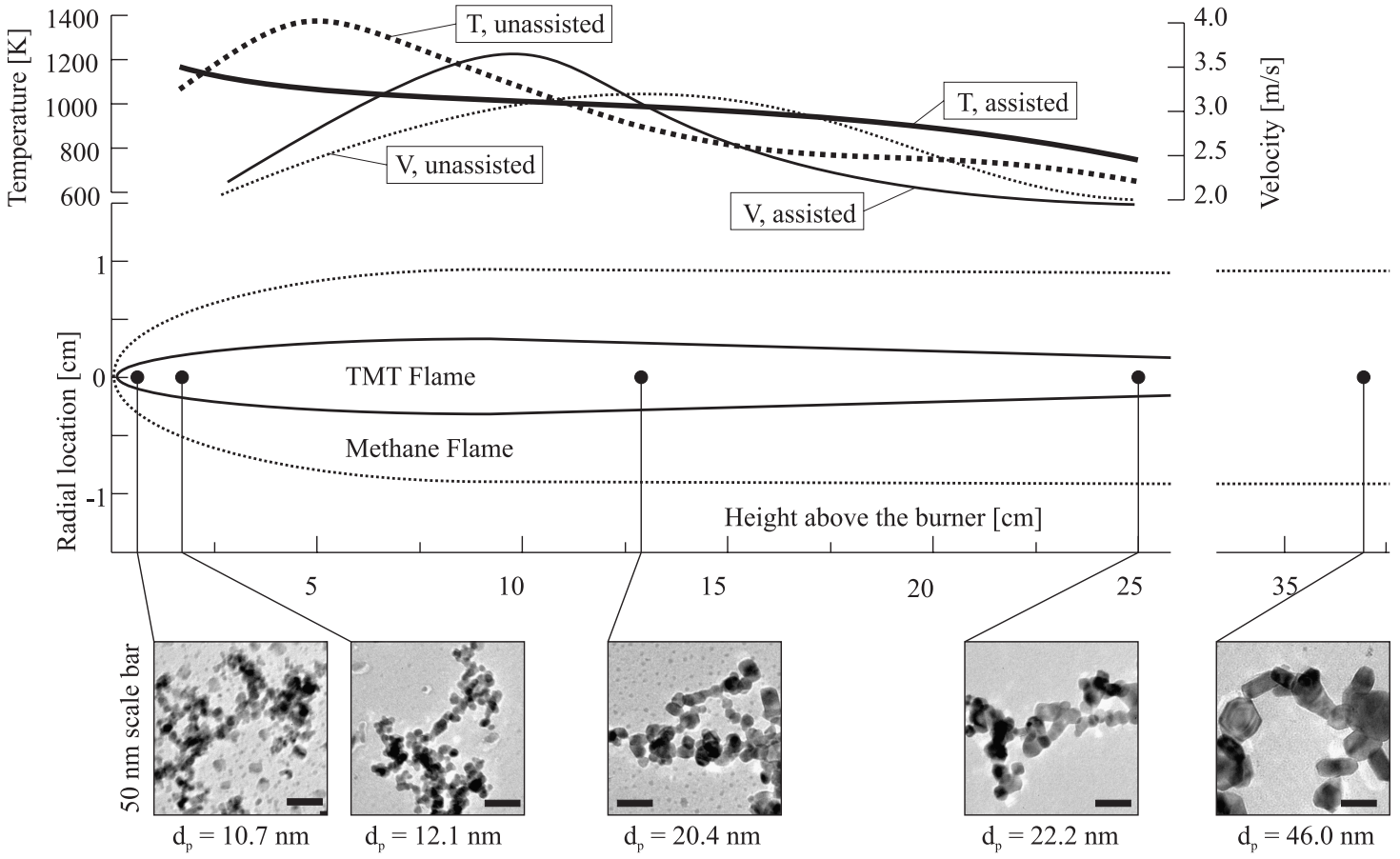

Figure 3.20: The evolution of SnO_2 morphology in the MACS system. A schematic of the flame structure is provided for reference. Polynomial fits to the thermocouple and PIV data are provided in the upper panel.

data were fit to polynomial profiles presented in chart located in the top panel of Fig. 3.20 and are used in the characteristic time analysis discussed below. The velocity data were obtained along the center-plane of the reactor, where instantaneous PIV data were averaged over 100 frames or 21 sec. The data indicate the particle velocity accelerates for both synthesis systems; however, the maximum velocity for the MACS system is higher than that of the unassisted system and occurs closer to the burner surface. The differences in temperature and velocity profiles suggest longer temperature residence times for the particles formed in the MACS system.

3.3.2 Gold and aluminum doped SnO_2

To study the effects of the MACS on nanocomposite systems, gold and aluminum doped SnO_2 particles were produced. Typical TEM images of the nanocomposites sampled at a height of 37 cm are shown in Fig. 3.21. As seen in Figs. 3.21b and 3.21d, long crystals are also observed in the doped MACS powders. The high contrast particle in Fig. 3.21a is gold encapsulated in a layer of SnO_2 particles as determined using XEDS. For the MACS system, all the gold particles observable by TEM imaging were encapsulated in SnO_2. In the absence of methane, the observable gold particles were rarely encapsulated (see Section 3.1 Fig. 3.5 inset). Figure 3.21b is an image of typical SnO_2 particles present in the gold-doped system that did not indicate the presence of gold when analyzed using XEDS. XRD Scherrer analysis of the powders produced using the gold acetate precursor resulted in an average SnO_2 crystallite size of 20.2 nm. The average crystallite size for gold (based on the $\langle 200 \rangle$ gold peak of the XRD spectra) was 60 nm for the MACS system and 81 nm for the unassisted system. The smaller size of the Au particles produced using the MACS system may be attributed to the encapsulation by SnO_2 which will limit Au particle

growth and aid diffusion of Au into the SnO_2 crystallites.

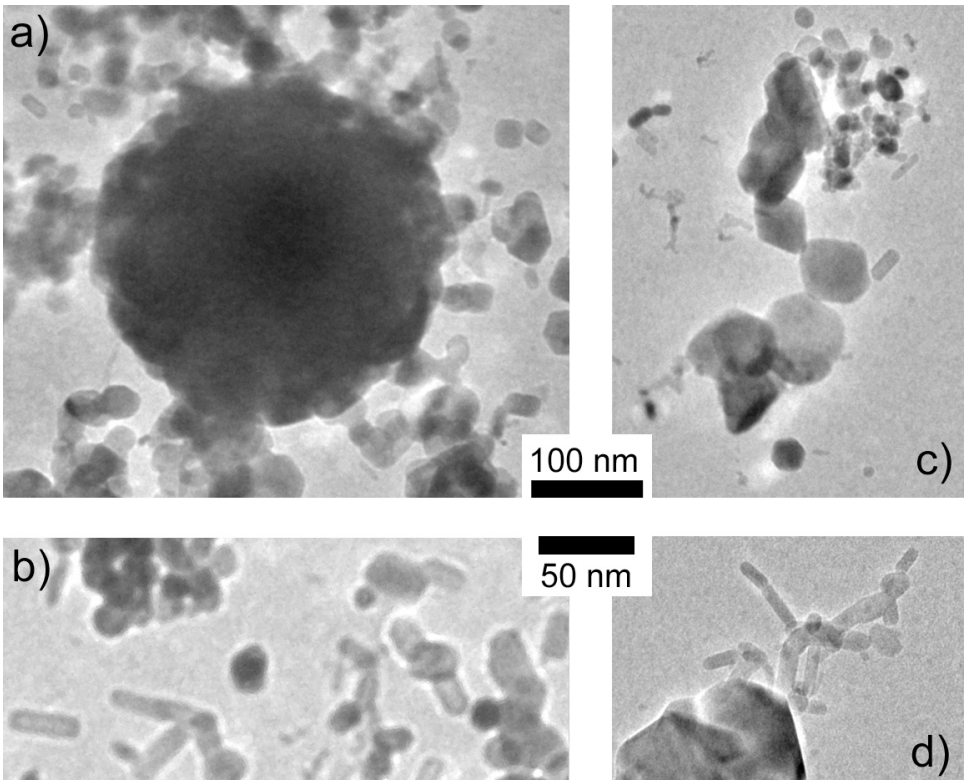

Figure 3.21: TEM images of tin dioxide doped with (a and b) gold and (c and d) alumina produced using the MACS. The high contrast particle in (a) was identified as gold using XEDS.

Figures 3.21c and 3.21d present typical morphology of the particles produced using aluminum acetate as the additive precursor for SnO_2. No encapsulated nanocomposite structures were observed for the Al-SnO_2 system, and the particles shown in the TEM images of Fig. 3.21 did not indicate the presence of aluminum in the XEDS spectra. XRD analysis of the SnO_2 produced using the aluminum acetate precursor showed no indication of aluminum or aluminum oxide peaks, and Scherrer analysis resulted in an average crystallite size of 24.6 nm. Additional studies of the Al-SnO_2 system indicated aluminum (presumably in the form of alumina) was present in the doped SnO_2 powders (Section 3.1), but was below the detectable limits of the XEDS and XRD analyses.

3.3.3 Simplified particle transit time study

Numerous models have been employed to predict reaction, nucleation, coagulation and coalescence processes in combustion synthesis systems, including Monte-Carlo simulations, sectional and moment methods, and multivariate population balance approaches to name a few [80, 81, 42]. Major weaknesses are often in the nucleation theories [42], and in the difficulty of applying such models to composite systems where multiple condensed phase species are present.

In the current work, a simplified model of the characteristic times for the particle formation and growth mechanisms was developed for the MACS and unassisted systems. The model is used to gain a better understanding of how methane affects the synthesis environment to yield the morphologies observed (e.g. the large SnO_2 primary particles and SnO_2 encapsulated gold particles). The burner operating conditions, the reactant and product material properties and the experimental data for temperature and velocity are critical input parameters for evaluation of characteristic time for agglomeration, chemical reaction, sintering and flow (transit) times. The characteristic times provide a metric for comparison between the MACS and the unassisted systems and the resulting nanoparticles. Xing *et al.* [82] proposed similar criteria for the study of flame synthesized alumina nanoparticles for which characteristic times as a function of temperatures were considered. For this study, characteristic times for the SnO_2 systems as a function of height above the burner surface are used to interpret the TEM imaging results.

In order to calculate the characteristic reaction time ($\tau_{reaction}$), the unimolecular decomposition reaction of TMT was used. The chemical reaction rate (Eqn. 3.2) was based on kinetic modeling of chemical vapor deposition using tetramethyl tin

as a precursor by Zawadzki *et al.* [83]. From several potential reaction rates the unimolecular decomposition reaction rate (Eqn. 3.3) was chosen due to its relatively low reaction rate.

(3.2) $$(CH_3)_4Sn \rightarrow (CH_3)_3Sn + CH_3$$

(3.3) $$k = 5 \times 10^{15} exp\left(\frac{-32,473}{T}\right)$$

Since the molar concentration of TMT is a function of height, the decomposition rate was used to obtain the location where TMT is completely depleted. Because, the actual TMT consumption rate is presumably higher than the thermal decomposition rate (due to radical attack and oxidation), the location determined for complete TMT consumption is considered a conservatively high estimate.

The coagulation time (Eqn. 3.4) is based on the collision frequency of single particles with rapid coalescence in the free molecular regime. The free molecular regime assumption requires large Knudsen numbers where the mean free path of the particles is much larger than the diameter of the particles. The variables and constants in the equation are as follows: k_B is the Boltzmann constant, ρ_p is the particle density, n_p is the number density of particles and d_p is the characteristic particle size. For tin dioxide the bulk density was used to represent the particle material density, $\rho_p = 6.95$ g/cm^3.

(3.4) $$\tau_{collision} = \frac{1}{2n_p}\left(\frac{6k_BT}{\rho_p}d_p\right)^{-1/2}$$

Here d_p represents the mean particle sizes involved in the collisions. For this study, TEM image analysis using the semi-automated method was conducted at

various heights above the burner to yield average particle sizes as a function of height. Figure 3.22 shows the particle size variation as a function of height for the unassisted and the MACS system. Approximately, 200 - 500 primary particles were used to estimate average particle size at each location. Therefore, the mean values for d_p obtained from the TEM image analysis were used to determine the collision frequencies at various heights above the burner.

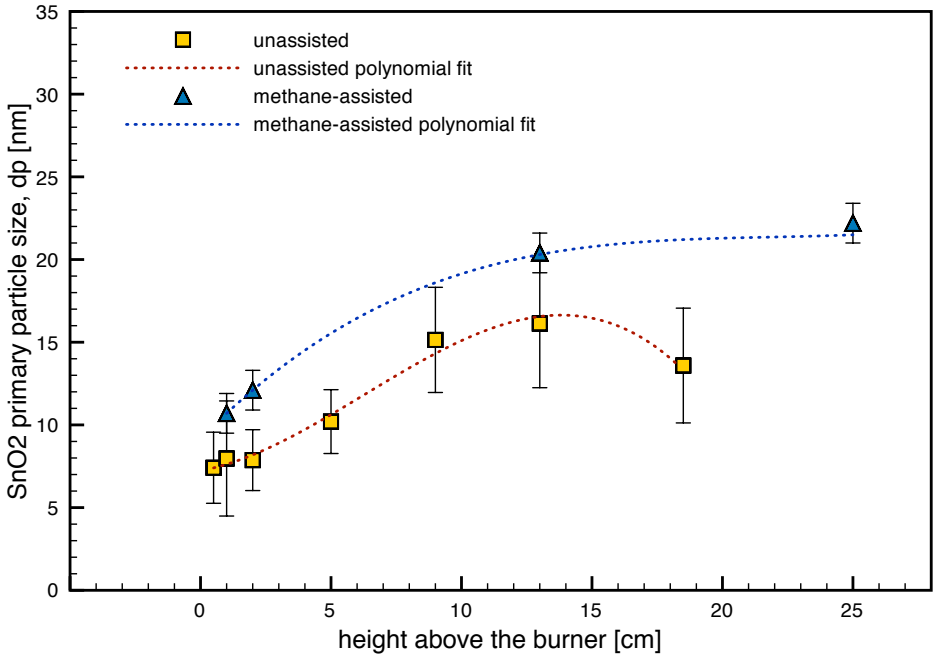

Figure 3.22: Primary particle sizes as a function of height above the burner for the unassisted and the MACS system. The error bars represent the standard deviation in the primary particle sizes at each location.

The number density n_p, on the other hand, was calculated assuming complete conversion of tetramethyl tin to tin dioxide at the given flow rate of TMT in argon. The number density, for Eqn. 3.4 was estimated by considering average tin dioxide particles entrained in the reactant gases ($H_2/O_2/Ar$). This provided a conservatively low estimate for collision frequencies.

The characteristic sintering time is a strong function of the mechanism selected

to represent the sintering process. There are primarily four sintering models available in the literature based on the surface-energy minimization, initial-stage sintering approach documented. They are described by Coblenz *et al.* [84] and include evaporation-condensation, surface diffusion, grain boundary diffusion and lattice diffusion mechanisms. For example, Xing *et al.* [82] used volume, surface and grain-boundary diffusion models for alumina sintering and the three models span an order of magnitude in sintering rate and have different dependences on particle size. Xiong and co-workers [81] used a two-dimensional moving-sectional technique to obtain effective sintering rates for pure titania, silica and silica-doped titania. Leite and coworkers [85] developed a thermally activated empirical model for tin dioxide sintering and showed that it is a combination of evaporation-condensation and surface diffusion mechanisms which better represents the sintering processes for tin dioxide. Equation 3.5 presents the empirical equation based on a scale law model by Leite *et al.* [85]:

$$\tau_{sinter} = d_p^{7.8} 3.23 \times 10^{20} exp\left(\frac{24,535}{T}\right) \tag{3.5}$$

This approach is powerful because it incorporates the effects of the change in dominant sintering mechanism from surface diffusion at low temperatures to evaporation/condensation at high temperatures specifically for SnO_2 nanoparticles. Again, d_p in the equation above represents the primary particle sizes that is a function of height above the burner. Since this is an average value, the sintering times for particles one standard deviation away from the mean is evaluated to acquire a range of characteristic sintering times.

The characteristic sintering times for the gold particles were estimated using a grain boundary or surface-diffusion based sintering model:

$$\tau_{sinter,Au} = \frac{\left(\frac{x}{r_p}\right) r_p^4 RT}{CwD\sigma_{sv}\Omega} \tag{3.6}$$

which closely approximates the molecular dynamics results obtained by Arcidiacono and co-workers [86] on gold coalescence. Here C is a constant ($C = 225$ for surface diffusion model), r_p is the radius of primary particles, σ_{sv} is the surface tension/energy for the material ($\sigma_{sv,Au} = 1.12$ J/m^2 [87]), D is the diffusivity for gold at specified temperature in the form of $D = D_o exp(-E_a/RT)$ [86], R is the gas constant, Ω is the molar volume, and w is the surface or grain boundary layer width, estimated as $\Omega^{1/3}$ (both of which are based on particle size).

The flow transit times were calculated in two ways: based on the fluid velocity $\tau_{res,v} = |dv/dz|^{-1}$ and based on the temperature dependent flow, $\tau_{res,T} = |v_z d(lnT)/dz|^{-1}$. The flow transit times were determined by integrating the axial flow profiles of Fig. 3.20 from the surface of the burner to the axial location of interest. The temperature dependent flow transit time may be considered more meaningful as it accounts for the local temperature gradients [82].

The three parameters that differentiate the two synthesis systems are temperature, velocity and average primary particle size as a function of the vertical axis of the reactor. By changing these input parameters based on the experimentally measured data for the MACS and the unassisted systems, the characteristic times were calculated and plotted as a function of height above the burner. Figure 3.23a and 3.23b present a comparison of the characteristic times for the unassisted and MACS systems, respectively. Note that radial effects are not considered in the calculations, and the transit times are based on the central axis of the burner because the TEM images and the corresponding PIV results were taken along the central axis.

The presence of methane results in longer temperature dependent flow transit

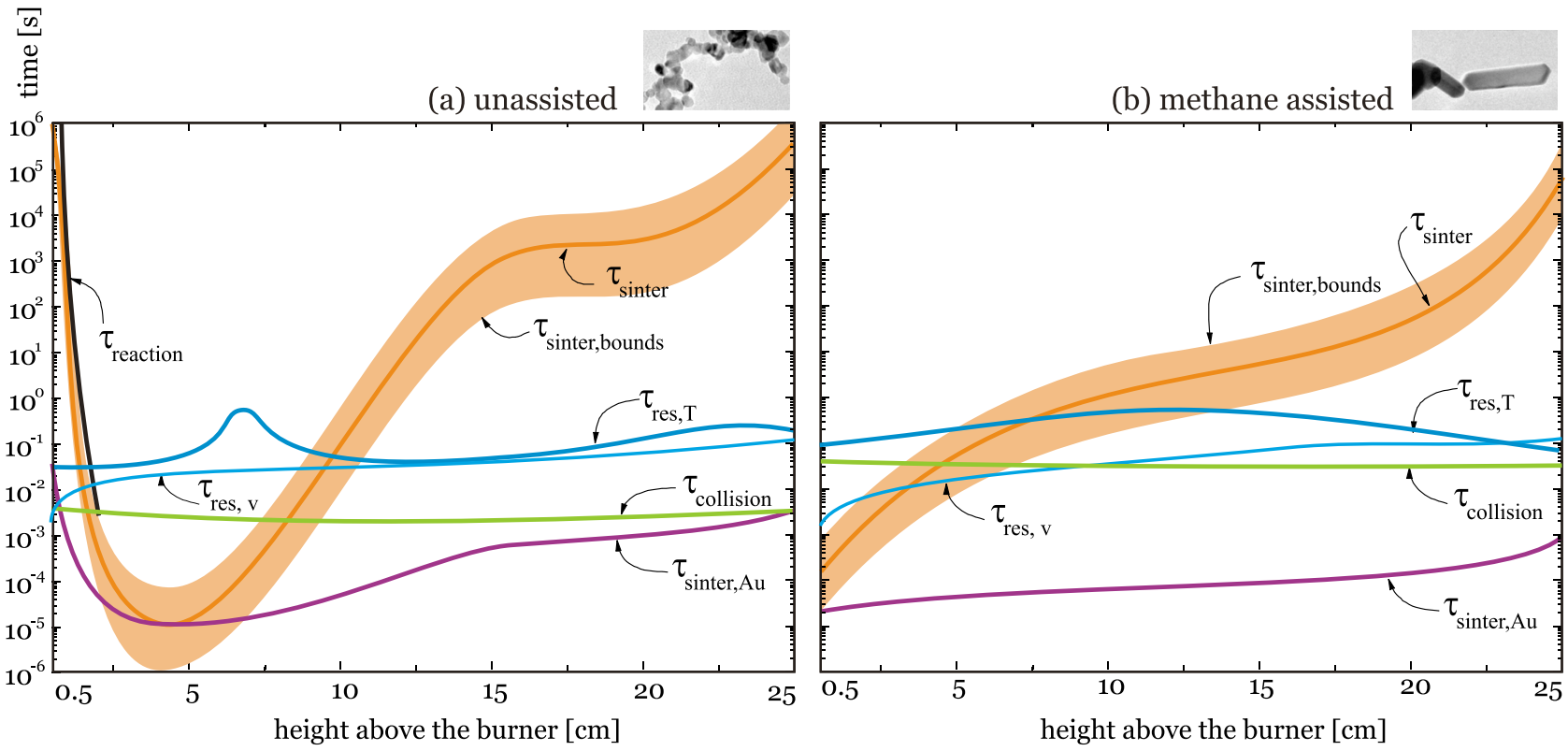

Figure 3.23: Characteristic times for particle formation and growth in the (a) unassisted synthesis system and (b) MACS synthesis system

times compared to the unassisted system. Hence, particles in the MACS flames experience higher temperatures at equivalent sampling heights. Due to the differences in transit times, the TMT decomposition times are also significantly different. For the MACS system the TMT is completely consumed below 0.5 cm, while the decomposition continues to approximately 2.0 cm for the unassisted system. The results suggest that nucleation of SnO_2 particles occurs at a much earlier stage for the MACS system, followed by longer times at high temperatures for particle agglomeration and growth by sintering.

Both systems have rapid sintering rates at lower locations due to the high temperatures and small particle sizes. However, the characteristic sintering times for the unassisted flames becomes significantly longer compared to the MACS flame at higher locations (11 - 25 cm) explaining the presence of highly sintered large crystalline primary particles observed for the MACS system (see Fig. 3.16b and 3.16c). Gold sintering times, on the other hand, are much shorter for both the systems indicating virtually instantaneous sintering of gold particles; consistent with the large spherical particles observed in the gold-doped SnO_2 system (see Fig. 3.21a).

Both systems have coagulation times less than the flow transit times, indicating agglomeration of primary particles, consistent with the TEM observations (Figs. 3.16 and 3.21). The decrease in the sintering rates at increasing heights is consistent with the increased presence of necking or bridging between primary particles observed at the higher heights.

Sintering or coalescence represents the process by which two particles fuse to form a single particle. According to the simplified model analysis presented at the oral defense, the primary process of tin dioxide primary particle evolution into larger particles for the methane-assisted system was deduced to be sintering. It was inquired

that if this was true then the particle sizes in the lower locations of the flame (where sintering dominates) can be predicted purely from particle diameters by the process of fusing smaller particles into a single larger particle. An estimate of the order of power for the particle diameter was made. In order to simplify the analysys, primary particle sizes with an average diameter of 10 nm (based on TEM image analysis) were considered at a height of 1 cm above the surface of the burner. Given sufficient time for two particles of the same dimension to sinter, the particle diameter would increase by approximately a factor of 1.26 (or $d^{1.1}$). The average particles size at 2 cm above the burner was evaluated to be 12.5 nm. Thus, the calculated factor predicts primary particle size well. However, this trend is not straightforward to propagate because at higher locations the time required for particles to completely sinter increases due to the decrease in local temperature. Therefore, only partial sintering is present at higher locations.

3.3.4 Methane-assisted study conclusions

The MACS method demonstrated in this work greatly expands the range of control possible over SnO_2 structure (including high aspect ratio single crystalline structures and encapsulated morphologies), additive composition (including good integration of the additives within the SnO_2 architecture and the versatility to use a wide variety of metals as additives) and average crystallite size (from 24.6 nm using MACS to 6.9 nm for doped SnO_2 created with the unassisted system [58], based on XRD). This system also provides the first flame synthesis of high-aspect ratio tin dioxide crystal structures of which we are aware. The long SnO_2 crystalline structures produced by MACS can have significant implications with respect to gas sensor performance, considering current efforts towards one-dimensional structures for gas sensing. Nanorod

and nanobelt materials have been demonstrated as having highly desirable sensor properties, such as sensitivities to a few ppb [25]. However, the synthesis methods used for these are complex catalyst-assisted recipes involving multiple fabrication steps. Combustion synthesis allows one-step processing for these idealized structures.

The MACS particles are largely one dimensional with minimal necks and crystalline defects and they have high surface area to volume ratios. Consequently, the gas sensing performance of the MACS materials may be similar to single crystal and nanobelt SnO_2 sensors, with high sensitivity. Optimization of MACS could yield nanorods with length dimensions comparable with the thermal evaporation and vapor-liquid solid (VLS) processing techniques currently used to fabricate SnO_2 nanorods. The high production rates and high quality of combustion synthesis materials would greatly increase scalability.

Instead of using TEM based particle size measurements, a ZetaSizer was recommended to achieve a statistically meaningful measurement of tin dioxide particle dimensions. The ZetaSizer provides measurements of sub-nanometer diameters in large quantities. It is a dynamic light scattering technique which yields hydrodynamic diameters of particles. Since the tin dioxide particles in the flames are aggregated structures, the primary particle dimensions will be difficult to interpret using ZetaSizers. However, there is value in quantifying the changes in the size of the aggregated structures as a function of location in the flame system. Such data would provide an additional parameter to monitor and compare between the methane-assisted and unassisted combustion synthesis systems.

The accurate prediction of particle morphology remains an elusive and difficult goal. The simplified modeling approach used here is a powerful means to provide

insight into the controlling mechanisms for particle formation, growth and evolution for nanocomposite systems and can be used to explain the qualitative trends observed. Understanding the active sintering mechanism for the materials is critical for even qualitative predictions and interpretation of single component or composite nanoparticle systems. The modeling approach can be improved by expanding the sintering mechanism as a means to incorporate surface growth, i.e. size dependent sintering.

3.4 Combustion synthesis conclusions

The combustion synthesis studies presented here demonstrate an appreciable range of control over particle size, metal additives and particle morphology for tin dioxide. Besides the variety of nanoparticles and the nanocomposites demonstrated, results of the studies of the decomposition and particle evolution mechanisms provide tremendous opportunities for tailoring nanoparticles by altering precursor material, temperature profiles, quenching methodologies, and precursor introduction. One of the greatest contribution of our work has been the demonstration of using solid-phase precursors in combustion synthesis systems. The studies presented here provide further insights into the particle evolution process and motivate future exploration in multi-phase precursor combustion synthesis. Preliminary studies to explore further control strategies over combustion synthesis are presented in the Appendix **??**. These studies include unpublished work that explore new particle precursors and pre-processing material methods. The potential applications for the unique materials demonstrated in the studies presented here are not limited to developing novel sensing architectures (as will be discussed in the next Chapter) but also apply to

nanoparticle use in catalysis, battery and surface coating technologies, to name a few.

CHAPTER IV

Gas Sensing

This chapter presents the results for establishing a testing platform for elucidating the links between the combustion-derived material properties of the sensing film and the performance for detecting target gases. It is crucial for such an undertaking to reduce the effects of all variables, other than microstructure and composition, that affect sensor behavior to make a more meaningful comparison between sensors. Variables such as film-electrode bonding properties, operating temperature, target gas, gas concentration, platform properties, sensor processing and conditioning must remain nominally constant between sensor tests. Leaving only the microstructure and film composition to affect sensor performance.

The tests were designed to maintain a constant target gas concentration for all tests (500 ppm carbon monoxide, CO) with all tests conducted at approximately 330 ^{o}C. The combustion-generated powders were to be tested on identical platforms, thus eliminating the influence of the substrate and electrode properties. The challenge was to create a well controlled method of tin dioxide film deposition which would yield consistent sensor film properties. The method required deposition of tin dioxide nanoparticles in a powder form. Sol-gel deposition is a common method for achieving a uniform thin film; however, it involves *in situ* synthesis of SnO_2 [88, 55, 89, 56].

Screen-printing methods, on the other hand, entail depositing powders generated *ex situ* using a printer with sufficient control over film thickness and uniformity [90, 67, 19]. The screen-printing method requires the powder be a paste form using an organic or inorganic carrier and a printer.

Initially the custom sensor platform, described in Section 2.2.2, was designed and selected for the sensor study. This would allow testing multiple sensors on a single substrate with common processing and fabrication histories. However, due to poor electrical contact between the tungsten probe assembly and the platinum contact pads on the substrate a redesign of the probe mount was necessary. An attempt was made to level the probes by mechanical grinding and polishing for better contact for all size probes which was unsuccessful. The commercial multi-sensor platforms manufactured by Heraeus Sensor Technology were selected for sensor studies of the combustion generated powders.

The gas sensing data are divided into results from undoped SnO_2 and doped SnO_2 nanocomposites; all generated using the combustion synthesis methods presented in Chapter 3. The undoped-SnO_2 section presents the results of extensive efforts made to establish a methodology for film deposition, processing, operating temperature, etc. which would allow evaluation of the influence of microstructure on gas sensing. The results from the doped-SnO_2 sensors present the effects of additives in the sensor films on performance.

4.1 Undoped-SnO_2 sensors

The undoped tin dioxide powders were generated using the combustion synthesis approach described in Section 2.1. The optical chimney was used to improve the

capture efficiency of the powders. The powders were removed from the surface of the cold plate and ground using mortar and pestle. The further processing and analysis of the powders is described in the proceeding sections.

4.1.1 SnO_2 film deposition

Direct thermophoretic deposition from the combustion products was attempted on glass and alumina substrates. Dry-deposition has previously been shown to yield films on the order of 1-5 μm thick on alumina substrates [14]. Even though a thin film of the combustion synthesized powders was deposited, the film was only loosely bonded to the substrate and easily delaminated from the substrate during handling. Annealing the film at 500 - 600 ^{o}C did little to improve the mechanical adhesion of the film to the substrate.

Spin coating is a common method for depositing uniform films of organic liquids, such as photoresists in microfabrication, with appreciable control over the film thickness. Sakai *et al.* and others [32, 91] have successfully adopted spin-coating to deposit SnO_2 thin films with thicknesses ranging from 100 - 1000 nm. Preliminary studies of spin-coating SnO_2 dispersions (in ethanol-water solution) on unprinted alumina wafers showed some success in depositing a thin film uniformly on the substrate even though the film bonding was weak. Spin-coating was challenging with the multi-sensor platforms because of the small dimensions and due to the ceramic layer protecting the contact leads. The lead contacts create an uneven surface which limits the uniformity of the coating.

Based on the exploratory work presented above, two challenges of sensor fabrication process remained: identify a repeatable deposition method and achieving acceptable film adhesion to the substrate. The next two sections address these chal-

lenges.

Binder screening study

Earlier research has shown that binders not only provide better film rigidity, but they also improve sensor response by lowering the absolute film resistance [92]. The recipes used for these studies were adopted from screen-printing and porous plug fabrication approaches suggested by Lee *et al.* [90] and Ihokura *et al.* [13], respectively. Three recipes were explored for the binder screening study. The goal of this study was to identify the binder-film combination that produced a distinct and repeatable distinct sensor response. The silicate-based recipe is a common binder used for tin dioxide gas sensors. Table 4.1 provides the recipes and the processing followed for the three sensors prepared on identical sensor platforms.

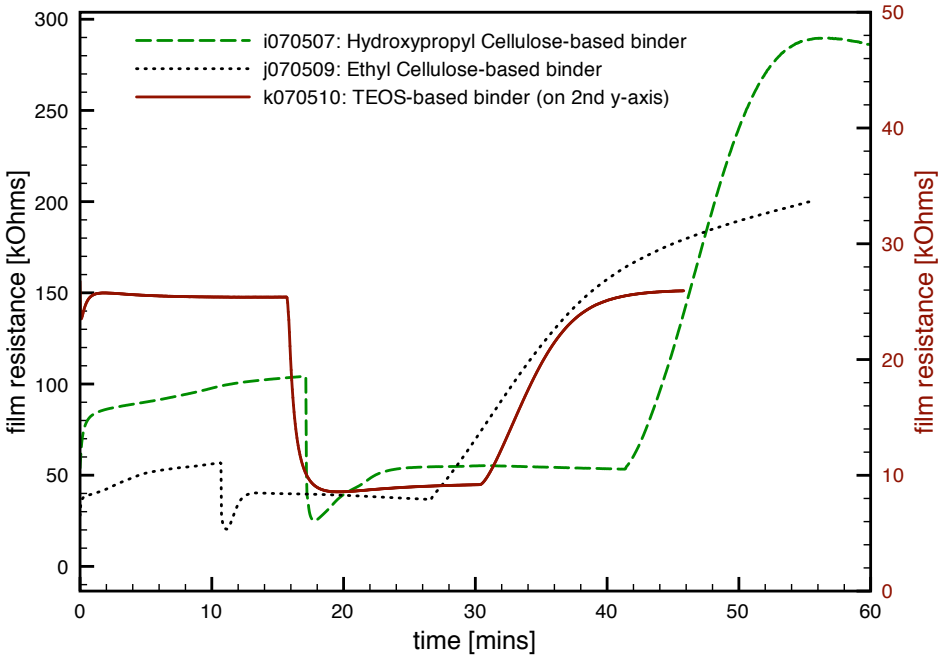

Figure 4.1: CS derived SnO_2 gas sensor response for three binder recipes. TEOS-based sensor resistance is plotted on the secondary y-axis to allow comparison of the data.

Figure 4.1 presents the gas sensor response to 500 ppm CO in dry air for each of

the binders considered. The sensor response for the TEOS-based sensor is plotted on the secondary y-axis since the absolute film resistance for this sensor was lower compared to sensors with other binder recipes. Note, the initial transience observed in the response is a common feature and corresponds to the interaction between the film and the voltage applied by the picoammeter to measure the film current. This is a less understood phenomenon that requires further research [93]. As the sensor is exposed to CO, all three sensors respond by reducing the film resistance. However, the sensors with cellulose-based binders (I and J) show a secondary response to CO after exposure to reach a different value compared to the initial minimum value. Such a response can be attributed to secondary reactions that may be taking place between the target gas and/or the detection products and the binder material. On the other hand, the sensor with silicate-based binder (K) shows an ideal sensor response after CO exposure. Once the CO flow is turned off, sensor K resistance returns to the initial baseline value in dry air while sensors I and J resistances approach significantly higher resistance values when compared to the initial baseline values.

The lower half of Table 4.1 summarizes the sensitivity and time response for each sensor-binder combination. The complete binder screen study results are available in Appendix B.1. Even though sensors I and J demonstrate higher sensitivity and fast time response, the sensor K behavior is more ideal in terms of response upon exposure to the target gas and sensor recovery to the baseline condition. The behavior of sensors I and J was consistent for every test, with lower initial baseline and much higher recovery baseline resistance. These results suggest a strong coupling of the change in resistance due to CO exposure and the baseline resistance.

Table 4.1: Binder recipes and preparation for sensors I, J and K used to test the influence of binders on sensor response.

Sensor I	Sensor J	Sensor K
	Recipe	
0.10 g SnO_2	0.32 g SnO_2	3.25 mL TEOS
0.05 g hydroxypropyl cellulose	0.32 g ethyl cellulose	1.35 mL ethanol
6.25 mL isopropyl alcohol	2.87 g α-terpineol soln.	0.35 mL H_2O
		0.05 mL 4% HCl
	Procedure	
Sonicated for 20 mins	Mixed and stirred	Made into paste
4 drop-coats with syringe	drop-coated with syringe	applied using spatula
sintering: 2 hrs @ 600 ^{o}C	sintering: 2 hrs @ 600 ^{o}C	sintering: 2 hrs @ 500 ^{o}C
	Average sensitivity, $S = \frac{R_a}{R_g}$	
4.34 $\pm$ 0.4	3.05 $\pm$ 0.24	2.97 $\pm$ 0.15
	Average time response, τ (sec)	
14.4 $\pm$ 11.8	4.2 $\pm$ 1.5	35.0 $\pm$ 5.9

Deposition method

Even though the silicate-based binder-paste recipe provided much improved sensor behavior, the reproducibility of sensor sensitivity and time response between sensors was still below the acceptable level to study microstructure effects. For instance, gas sensors with combustion synthesized powders from the same synthesis batch yielded sensitivities (S) ranging from 5 - 20. On one hand, such high sensitivities demonstrate promising gas sensor response for the combustion generated particles, and on the other hand, the results were difficult to replicate. There could be multiple reasons for the large deviations in sensor performance. Minor variations in film deposition could lead to non-reproduceable contact properties between the film and the electrodes. Additionally, since the binder solution was highly volatile due to the presence of ethanol, evaporation during the paste processing lead to varying paste

rheologies and therefore film properties.

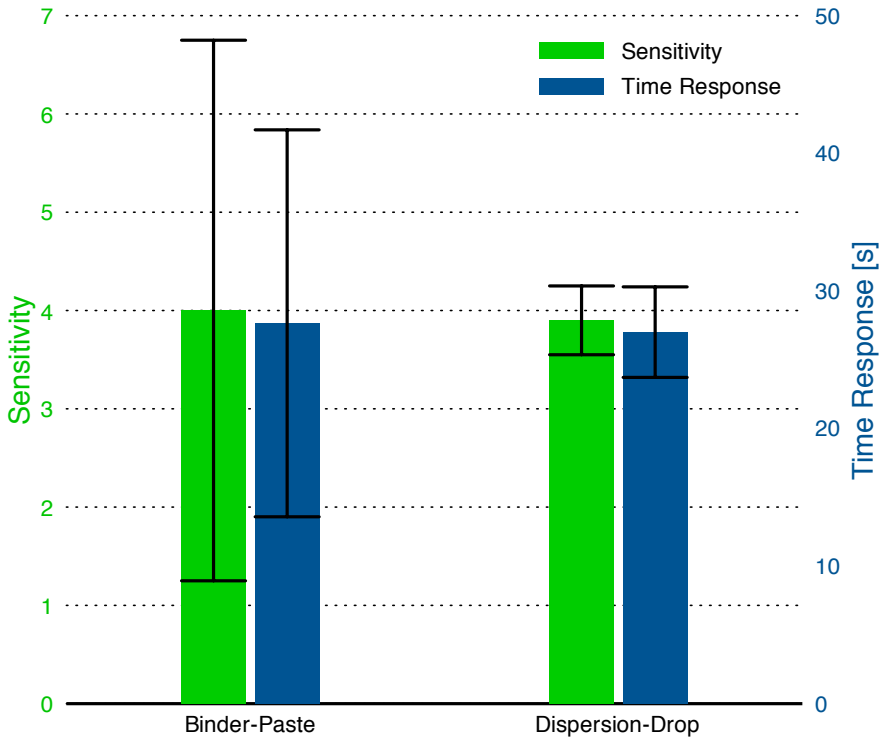

Figure 4.2: Comparison of sensitivity and time response between binder-paste method and dispersion-drop sensor fabrication methods. The error bars represent the variability in the sensors prepared with each method.

A new film deposition method was developed based on the tin dioxide dispersion initially used for the spin-coating process. The dispersion, described in detail in Section 2.2.3, was deposited as a drop on the sensing platform that eventually evaporated at ambient conditions leaving behind a relatively uniform 5 μm thick film of SnO_2. Generally five such layers were deposited (resulting in a 25 μm thick film) followed by an annealing step at 500 ^{o}C for 1.5 hrs. Figure 4.2 compares sensitivity and time responses of multiple sensors produced using either the binder-paste method described earlier or the new dispersion-drop method. The bar chart indicates comparable sensor responses for the two deposition methods; however, the dispersion-drop method demonstrates much lower variability between sensors. Additionally, com-

paring the absolute baseline resistance (in dry air) of the films, the dispersion-drop method yields lower resistances (R_a = 1 - 10 kΩ) than the films deposited using the binder-paste method (R_a = 100 - 500 kΩ). This result also indicates better electrical contact is achieved (due to lower contact resistance between the film and electrodes) using the dispersion-drop method to deposit tin dioxide films for sensing.

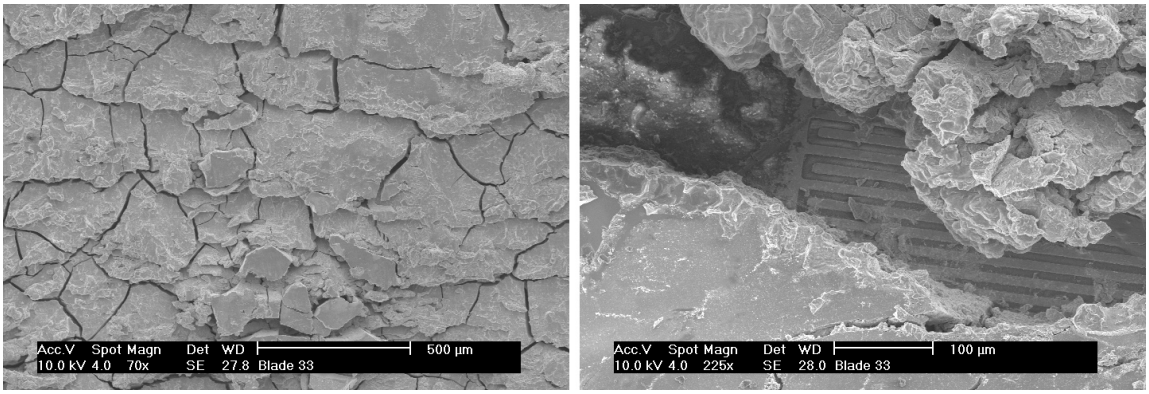

Figure 4.3: SEM images of tin dioxide gas sensor films deposited using the binder-paste method. Fractures were common features on the films. The interdigitated electrodes are visible under the film in the image on the right

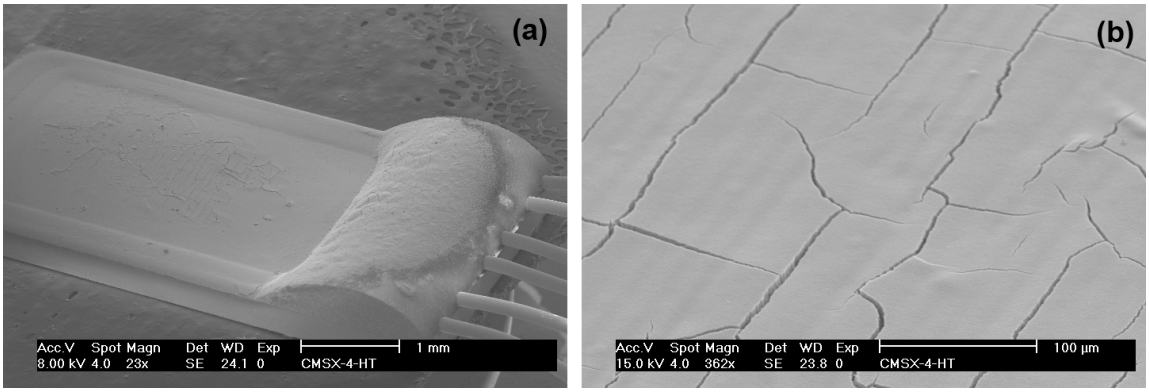

Figure 4.4: SEM images of tin dioxide gas sensor film (single layer) deposited using the dispersion-drop method. Fractures were common features on the films. The visible ridges on the film (right image) are attributed to the interdigitated electrodes underneath the film.

SEM imaging confirms the higher uniformity of the film achieved with the dispersion-drop method. Figures 4.3 and 4.4 show SEM images of the resulting films from the two preparation methods. The film thickness with the binder-paste method resulted

in films with thickness from 30 - 60 μm. This deposition method caused the film to have an uneven and non-uniform texture, as seen in Fig. 4.3. This was exacerbated by the difficulty of maintaining consistent rheological properties between pastes. Figure 4.4 shows a single layer of tin dioxide deposited with the dispersion-drop method. Compared to the films resulting from the binder-paste method the dispersion-drop method yielded more uniform films with improved control over film thickness. A common feature between the two methods is the presence of fractures in the film, presumed to be due to the drying process. The fractures are extreme in the case of the binder-paste method, leading to highly fragmented films. Figure 4.5 shows an optical microscope image of the film imaged in Fig. 4.4. This image demonstrates the optical transparency of the tin dioxide film with 10 μm wide electrodes lining the backside of the film.

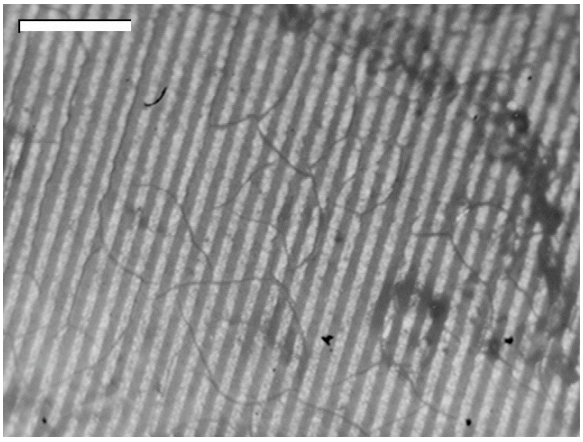

Figure 4.5: An optical microscope image of the film surface produced using the dispersion drop method. The image corresponds to the sensor as shown in Fig. 4.4. The scale bar here represents 100 μm.

The powders used for the sensors are derived from the unassisted combustion synthesis system described earlier. XRD Scherrer analysis of the CS SnO_2 powders showed no discernible change in crystallite size as a function of sintering at 500 ^{o}C for 2 hrs. The samples were prepared on glass slides and processed in parallel to the

sensors. The crystallite sizes of sintered and unsintered SnO_2 powders yielded an average of 15 $\pm$ 1 nm. TEM images of tin dioxide powders dispersed after sonication are deposited in a similar fashion as the films, revealed dense agglomerate structures, as seen in Fig. 4.6. The primary particles sizes shown in Fig. 4.6 range from 10 - 40 nm. Note that the TEM samples were not subjected to the annealing step.

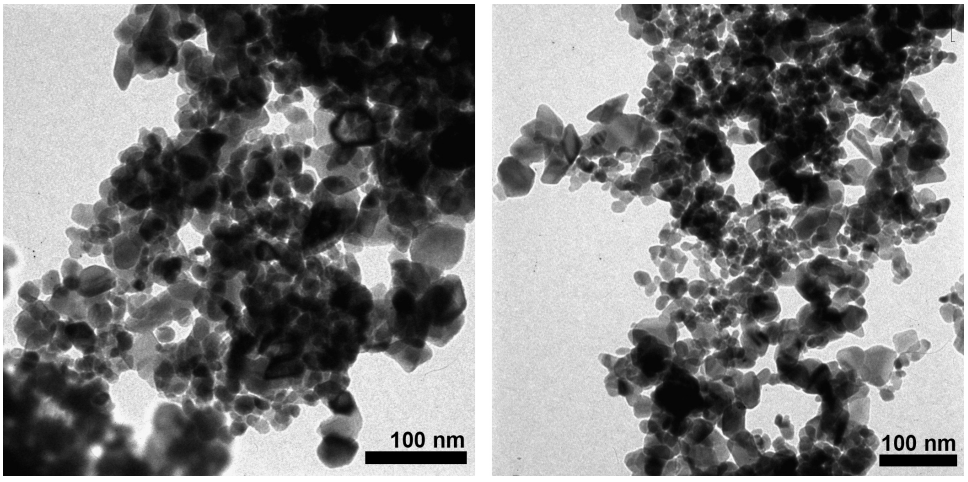

Figure 4.6: TEM images of the dense matrix of SnO_2 primary particles from samples acquired using the dispersion-drop procedure.

Beyond improving the deposition process, further attempts were made to achieve better film adhesion as well as enhanced inter-particle connections. The most common method of achieving these goals are to combine the sensitive powders with either glass frits [94] or aluminum oxide [13] in equal quantities. Here, a dispersion of SnO_2 and alumina nanopowder (Al_2O_3, Sigma Aldrich) in 1:1 weight ratio was deposited on the sensing platform. Using the standard process, the sensor was tested upon exposure to CO as before. Despite the lower film resistance, the response during CO exposure was non-ideal with an average sensitivity of 1.83 $\pm$ 0.27. Based on these results, no further changes to the dispersion-drop method were made.

4.1.2 Operating temperature

Chemisorption of oxygen species on the tin dioxide surface is a temperature dependent process. The higher the temperature, the higher the rate of oxygen adsorption and consequently the sensitivity of the sensor. However, there is an optimum temperature beyond which the desorption rates dominate leading to reduction in sensor sensitivity as temperature increases. To investigate this trend for the undoped-SnO_2 sensors, sensitivity and time response was monitored as a function of sensor operating temperature from 280 ^{o}C to 450 ^{o}C. The sensor was held at the specified operating temperature for over 24 hrs before testing under 500 ppm of carbon monoxide. Figure 4.7 presents the results of the study with each data point representing an average of three tests, with the error bar indicating the standard deviation in the tests. As expected the sensitivity increases as a function of operating temperature from $S =$ 2 to 7, while the time response decreases from almost 50 seconds to less than 20 seconds. This study, did not reveal a peak in sensitivity. Since the multi-sensor platform could not be tested beyond 450 ^{o}C (due to platform material limitations), it is expected the optimum operating temperature occurs beyond 450 ^{o}C. This is consistent with typical peak temperatures for tin dioxide gas sensors reported in the literature to range between 400 - 500 ^{o}C [34, 30].

4.1.3 Detectivity limit

To test gas sensor response to varying concentrations of CO in dry air, sensitivity was monitored as a step change in concentration. Figure 4.8 shows the sensor response for three CO concentrations: 25, 125 and 250 ppm in dry air (with total gas flow rates of 400 mL/min). To further reduce CO concentration, the total gas flow

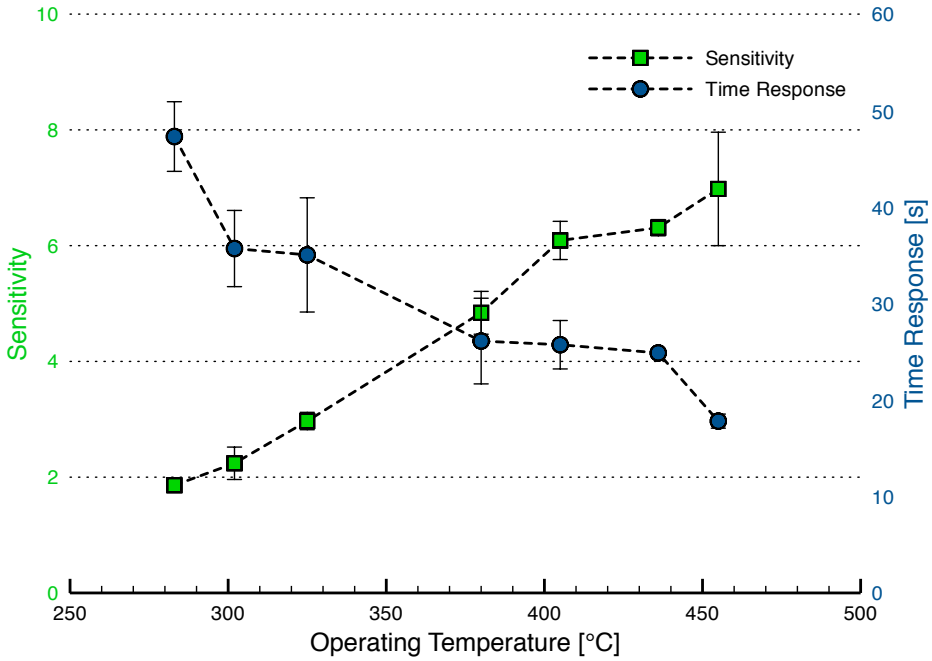

Figure 4.7: Sensitivity and time response as a function of sensor operating temperature. Error bars represent the standard deviation of three tests conducted at each operating temperature. All tests were conducted with 500 ppm CO in dry air.

rate had to be increased to 1000 mL/min, to allow better control of mixing. Note, these sensors were fabricated using the binder-paste method. At low CO concentrations (10 ppm), the sensitivities for two different SnO_2 gas sensors ranged from 1.4 to 2.9, while the time response ranged from 27 to 45 seconds. The CS generated powders showed excellent detectivity to low target gas concentrations.

4.1.4 Processing

Since porosity can play a significant role in gas diffusion, addition of subsequent layers of the sensing film can generate a dense network of pores that can potentially alter the time response of the sensors. Becker *et al.* [95], for instance, have shown how thin films (50-300 nm) of tin dioxide sensors are more sensitive to oxidizing species while thick films (15-80 μm) are more sensitive to reducing species as explained by

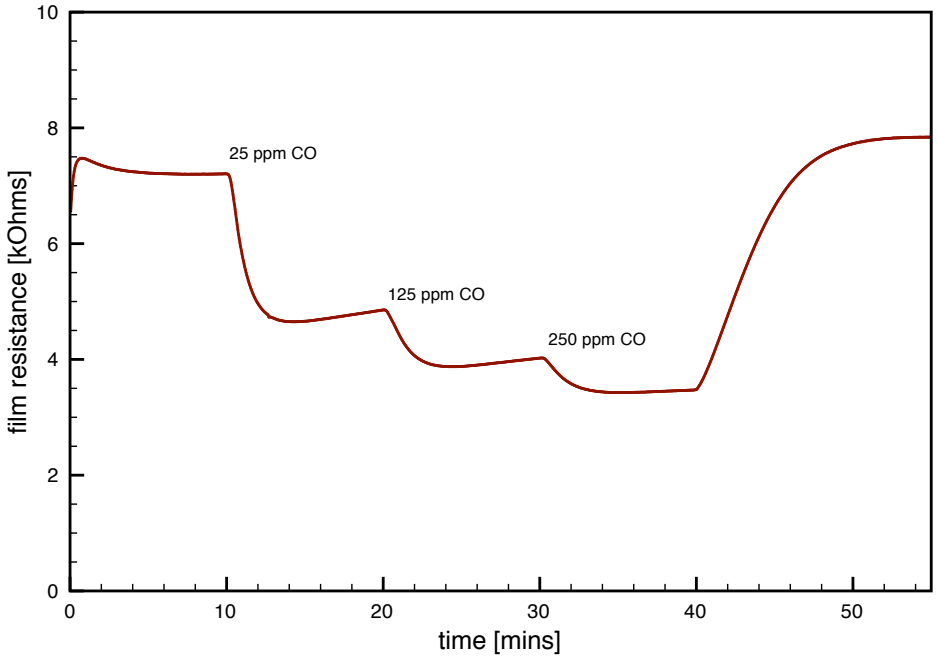

Figure 4.8: Sensor response as a function of change in CO concentration: 25, 125 and 250 ppm CO in dry air.

the pore diameters and the resulting depth profiles of the gas species. Karthigeyan and coworkers [96] as well have demonstrated film thickness dependence of sensitivity for thin film sensors (10 - 55 nm).

The current work explored the effects of film porosity and thickness by monitoring how the film characteristics evolve with the addition of layers using the dispersion-drop method. The sensor response as a function of tin dioxide layers deposited using the dispersion-drop method was investigated. A sintering step (at 500 ^{o}C for 1.5 hrs) followed each deposition step instead of the standard procedure where the sintering step followed the deposition of the fifth layer only. Figure 4.9 presents the sensitivity and time response measurements as a function of the number of layers deposited on the sensing platform for two sensor studies. As mentioned earlier, each deposited layer was determined to be $\sim$5 μm thick using side-view SEM images of films.

Comparing sensor response, there is a marked improvement in performance from

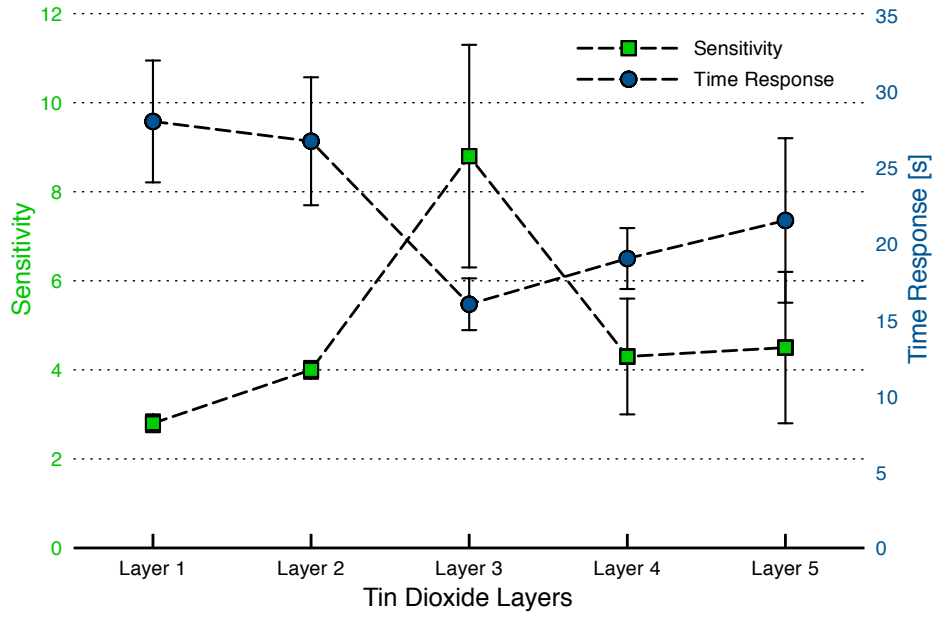

(a) Sensor ZR

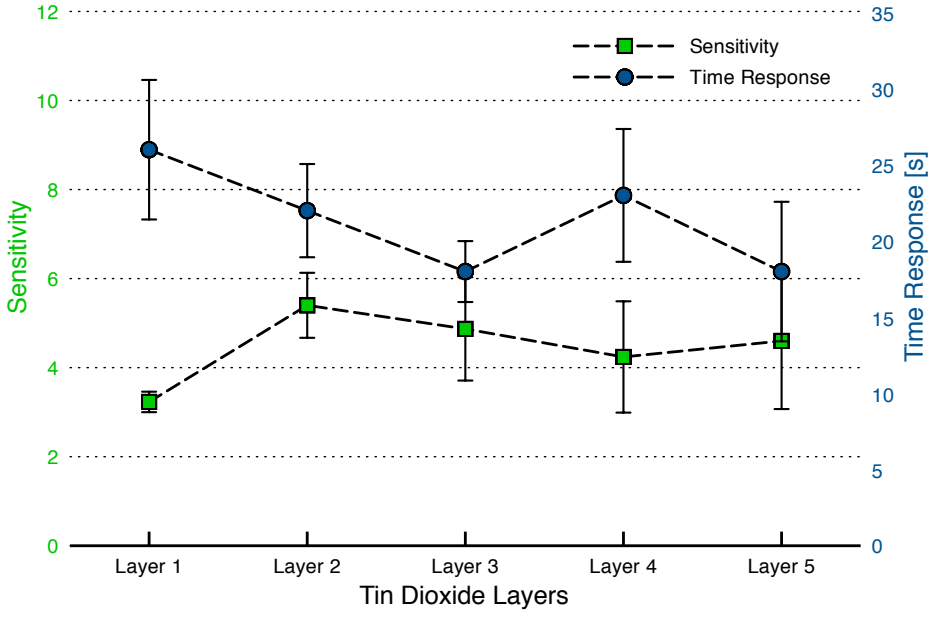

(b) Sensor ZX

Figure 4.9: Sensor ZR and ZX performance as a function of deposition layer. Each deposition step was followed by a 500 ^{o}C annealing step for 1.5 hrs. The error bars represent standard deviations associated with three tests conducted after each deposition.

a single layer to two layers of the sensing film. Recall that not only does the sensor consist of two layers which are nominally 10 μm thick, the film has received two sintering steps as well as conditioning twice at 330 $\pm$ 5 ^{o}C. Therefore, the sensor performance may be attributed to physical layering and/or to aging of the film. The dramatic jump in sensitivity and time response for the third layer on sensor ZR (see Fig. 4.9(a)) is considered an anomaly since it was not repeated in the second sensor. The deposition of layers four and five had little effect on the sensor performance.

In order to understand the effect of aging on the film, three sensors with identical SnO_2 dispersion layers were sintered at 500 ^{o}C for 1.5, 3 and 5 hours in the furnace. No discernible difference was observed in sensitivity or time response for the sensors. This suggests aging may not be a dominant influence on the results. On the other hand, the physical layering can affect the sensor by providing a denser network of interconnected particles compared to a single film. This may not necessarily affect diffusion as long as the pore sizes are still sufficiently large for the target gases to freely flow into the film. However, if the pore sizes did change dramatically on the order of the mean free path of molecules in air ($\sim$ 100 nm), then this can have a noticeable change in sensor behavior. Such pore size investigation on the bottom layer would be a challenging, at least using visual methods, since these pores are buried under the subsequent deposition layers.

Figure 4.10 presents two SEM images of the surface of sensor ZR. The images reveal a relatively smooth surface without the fractures that were typical for the films deposited without the sintering between layers. It is possible the sintering after each deposition relieves stresses in the film and reduces fracture development. The layer-by-layer sintering method yielded sensitivity and time response of 4.5 and 20 seconds, while the standard dispersion-drop method with the single sintering

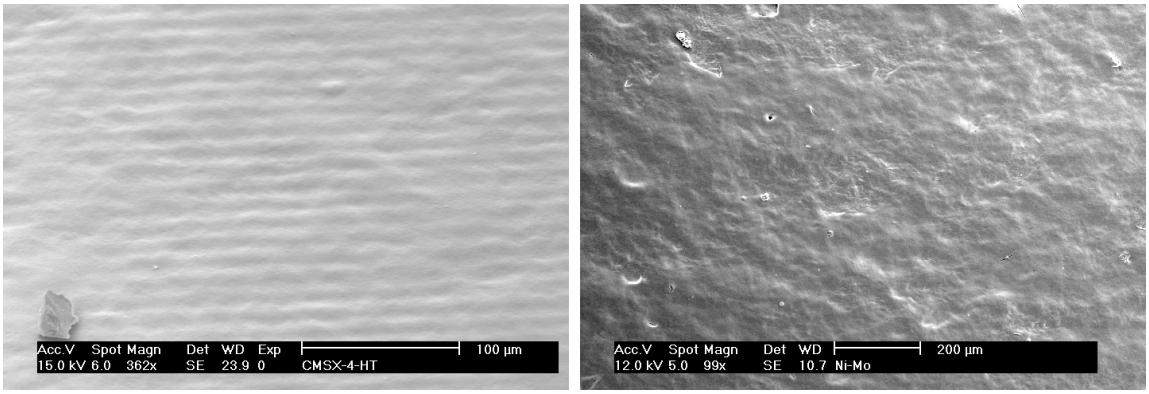

Figure 4.10: SEM images of sensor ZR after depositing the first layer (left) and after the fifth layer (right). The ridges (on the left) are attributed to the electrodes underneath the first layer of SnO_2 film.

process resulted in average $S = 3.7$ and $\tau = 26$ seconds. Consequently, these results may indicate how the existence of fractures may not significantly affect the sensing response as also suggested by Sakai *et al.* [32].

4.1.5 CS generated versus commercial SnO_2 powder

Since direct comparison of the dispersion-drop derived sensors with other tin dioxide sensor results published in literature is challenging due to the large number of variables involved (operating temperature, gas concentration, sensing platform, conditioning etc.), two different SnO_2 powders were investigated in the testing facility. For this study, CS generated SnO_2 power was compared to a commercial powder of tin dioxide (SnO_2, Alfa Aesar, 99.9%). The sensors were fabricated in parallel on two multi-sensor platforms, each experiencing identical processing steps. Figure 4.11 presents a bar chart that compares the two sensors. The sensitivity comparison shows that the sensor with combustion generated SnO_2 performs slightly better than the commercial powder sensor, while having similar time response. XRD analysis of the powders reveals a significant difference between the Scherrer crystallite sizes.

While the average crystallite size for the CS generated SnO_2 was 15 ± 1 nm, the Alfa Aesar powder yielded crystallite sizes of ~ 55 nm. The results are consistent with expectations for the effect of crystallite size on sensor performance, as suggested first by Yamazoe *et al.* [17].

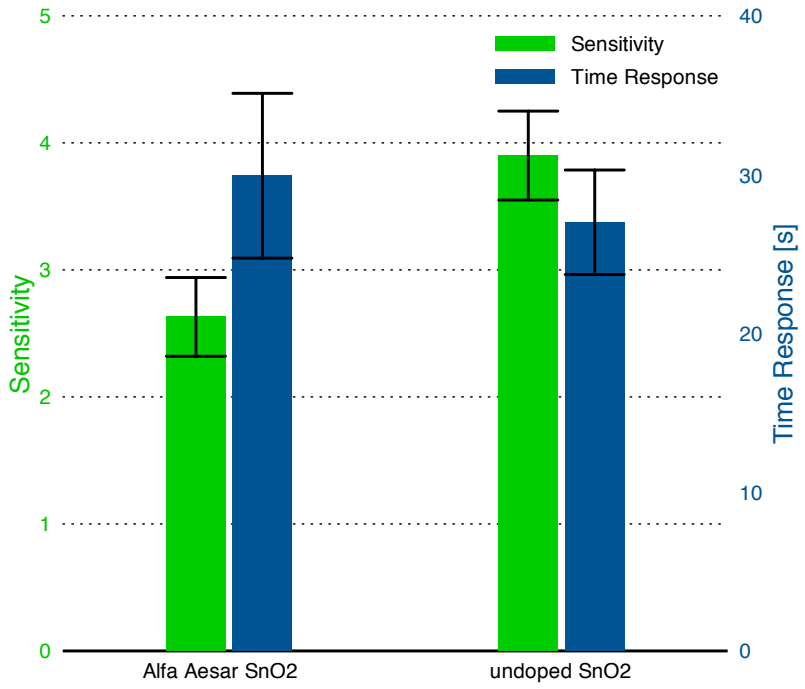

Figure 4.11: Comparison of sensor performance comparison of CS generated and commercial tin dioxide powders (Alfa Aesar). Sensor response was tested on identical platforms.

4.2 Doped-SnO_2 sensors

The previous section presented various characterizations of the sensor performance to establish a sensing platform and a methodology for evaluating microstructural and compositional effects on tin dioxide sensors. This section explores the impact of doping tin dioxide with metals or metal oxides on gas sensing.

Two doped-SnO_2 systems were considered for the following studies: gold- and palladium-doped tin dioxide. Gold and palladium demonstrate dramatic improve-

ments in tin dioxide gas sensors in terms of sensitivity and selectivity to target gases [97, 98]. Palladium and platinum are commonly added in non-negligeable quantities to commercial tin dioxide sensors to enhance performance [95]. Additionally, with respect to the combustion synthesis process, the metal acetate precursors used to generate gold- and palladium-doped tin dioxide have similar physical and chemical characteristics to achieve nominally identical compositions. This is particularly true for the powder entrainment characteristics of the respective metal acetates.

4.2.1 CS generated gold- and palladium-doped SnO_2 sensors

The combustion synthesized doped-SnO_2 materials were generated with the unassisted system described in Section 2.1. The optical chimney was used to improve the capture efficiency of the powders while the particle feed system was used to supply gold acetate and palladium acetate for the respective material systems. Each of the solid-phase precursors were sieved to < 45 μm before loading the syringe for entrainment. The captured powders were ground and applied to the sensing platforms using both the binder-paste and the dispersion-drop method. The sensor testing was performed in identical environments, with 500 ppm of CO in dry air.

Using the binder-paste method

Initial tests were conducted using the binder-paste method to deposit the gold- and palladium-doped tin dioxide powders. As observed for the undoped tin dioxide sensor study with the binder-paste method, there was such large variability between nominally identical sensors that it was impossible to draw any conclusions about the influence of the metal additives. For example, with gold-doped SnO_2, mean sensitivities ranged from 1.2 to 8.0 with time response varying from 8 to 47 seconds. The large

variations in sensor performance were attributed primarily to the deposition method that lead to large variations in the film properties. SEM images of the surfaces of three representative gold-doped tin dioxide sensors with highly inconsistent sensor response properties, show significant differences in the film characteristics (see Fig. 4.12). Amongst the three sensors, sensor Y produced the highest sensitivity and lowest time responses and note that sensor Y exhibits the least uniform film properties among the three sensors.

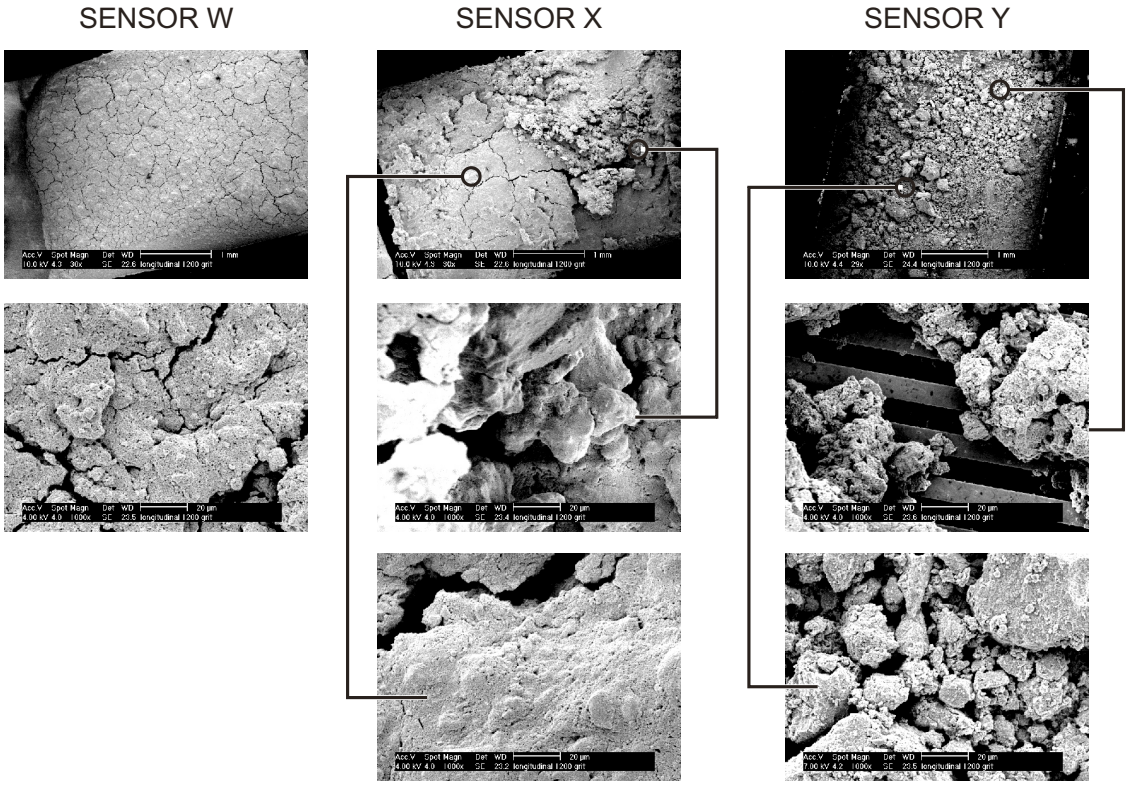

Figure 4.12: SEM images of gold-doped SnO_2 sensor films with highly variable sensor response based on binder-paste deposition method. Each sensor film consisted of identical combustion synthesized materials.

Similar results were obtained from the palladium-doped SnO_2 sensors when using the binder paste method, with a single sensor exhibiting high sensitivity ($S = 18$) while the rest of the sensors exhibited unmeasurable sensitivity. The low sensitivi-

ties may be explained by imperfect connection between the film and the electrodes; however, the extremely low resistances ($R_a < 1$ kΩ) were unusual and required further investigation. The low resistances may be an indication of the metal additives "shorting" the electrode connections.

Using the dispersion-drop method

Based on the improvements observed for the undoped SnO_2 system with the dispersion-drop deposition method; similar enhancements were expected for the doped system. The dispersions were prepared in the same manner as the undoped systems, with approximately 1.8 wt.% doped-SnO_2 powders dispersed in ethanol-water solution. The resulting dispersions of gold- and palladium-doped SnO_2 powders produced reddish-pink and grey-black dispersions, respectively.

As seen with the undoped SnO_2 sensors prepared with the dispersion-drop method, the doped SnO_2 also experienced a decrease in film resistances due to better film-electrode connectivity. Following the conditioning stage at 330 ^{o}C in dry air, the film resistances measurement yielded baseline resistances (R_a) between 0.06 - 0.18 kΩ, compared to R_a = 1 - 10 kΩ for the undoped sensors. These resistances were unusually low for both gold- and palladium-doped dispersed powders of SnO_2.

Figure 4.13 presents the sensor response of a gold-doped SnO_2 sensor with low baseline resistance (R_a = 0.17 kΩ) and low sensitivity (S = 1.08). The sensor demonstrates well behaved response, with the film resistance returning to the baseline value after the CO is turned off and no secondary response is observed following CO exposure. The palladium-doped SnO_2 sensor response was so far from ideal that itlimited the ability to determine sensitivities and time responses, as seen in Fig. 4.13. Note, the Pd-doped SnO_2 sensor response is plotted on the secondary y-axis

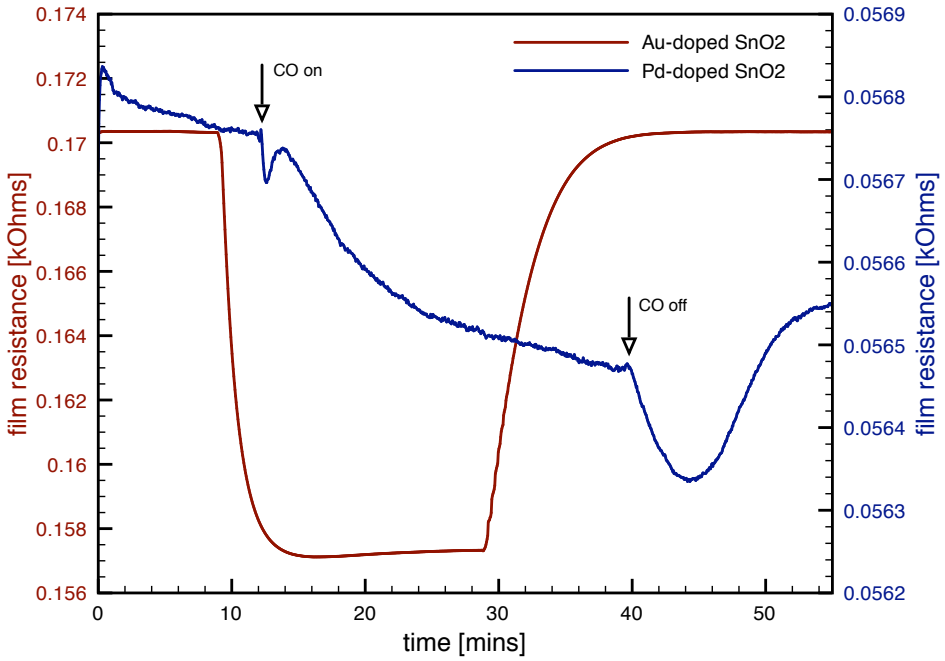

Figure 4.13: Sensor response for CS generated gold- and palladium-doped SnO_2 sensors. Changes in the carbon monoxide flow rates are indicated for the Pd-doped sensor response which is plotted on the secondary y-axis.

to allow better comparison between the gold- and palladium-doped sensors.

One of the possible explanations for the low film resistances is if the metal content (in other words the dopant loading) was so high that the metals effectively "shorted" the electrodes. To test this hypothesis the dopant loading was reduced by dilution with undoped SnO_2 dispersion. The doped and undoped tin dioxide dispersions were mixed in a 1:10 volumetric ratio that would lead to ten-fold theoretical reduction in dopant loading by weight. The gold- and palladium-doped SnO_2 dispersions were each diluted and deposited on sensing platforms for testing. However, the sensor response for each sensor remained unaffected by the dilution. Both the gold- and palladium-doped SnO_2 sensors exhibited significantly low film resistances, with the gold-doped sensor demonstrating low sensitivities ($S = 1.05 \pm 0.01$).

Film material analysis and discussion

Based on the experiments, it was clear that the unusual sensor response (low R_a) was a result of the inherent film properties and not the deposition process. This prompted material characterization of the film to investigate the potential causes for the low film resistances.

Table 4.2 summarizes the material characterizations performed on the doped SnO_2 films. It was initially thought that large metal particles (on the order of 10 μm) may bridge between the electrodes, lowering sensor resistances. XRD analysis revealed metallic gold, palladium oxide, and the casseterite phase of tin dioxide. XRD Scherrer analysis of the gold-doped SnO_2 indicated the average gold crystallite size of 65 nm with an average SnO_2 crystallite size of 15 nm. Crystallite size analysis of the palladium oxide could not be performed due to the convolved nature of the weak $\langle 111 \rangle$ PdO feature with tin dioxide peak. SEM XEDS yielded elemental gold content of the film to be $\sim$ 3 wt.% in tin dioxide. The XEDS results were augmented by electron microprobe analysis (EMPA) performed on doped dispersions of SnO_2 on glass slides. The EMPA was performed at approximately ten locations on the film (with probe sampling areas of $\sim$ 20 x 30 μm) and yielded mean weight percentages of gold and palladium to be 3.5 wt.% (1.6 at.%) and 8.6 wt.% (6.3 at.%), respectively. The complete results of the EMPA are provided in Appendix C.4.

Based on TEM and XRD results from previous (see Section 3.1 and Miller *et al.* [58]) and current studies presented in Table 4.2, there is no indication of large dopant particles that could span an electrode distance of 10 μm; especially since the average crystallite size for the doped gold particles is three orders of magnitude smaller than the electrode spacing. In terms of the dopant loading in the tin dioxide films, the

Table 4.2: Material characterization of the combustion synthesized doped tin dioxide powders.

Material property	Au-SnO_2	Pd-SnO_2
X-ray diffraction (XRD)		
Dopant crystalline phase	metallic Au	PdO
SnO_2 crystalline phase	cassiterite	cassiterite
Dopant crystalline size	65 nm	N/A
SnO_2 crystalline size	15 nm	16 nm
X-ray energy dispersive spectroscopy (XEDS)		
Dopant content	3.1 wt.%	N/A
Electron microprobe analysis (EMPA)		
Dopant content	3.5 wt.%	8.6 wt.%
Dopant content	1.6 at.%	6.3 at.%

XEDS and EMPA results indicate loadings consistent with previous studies where the additives improved the sensor performance [16]. For example, gold loading from 0.1-10 wt.% and palladium loading from 0.2-3 wt.% in tin dioxide has been shown to enhance sensor performance [16]. Both films analyzed here represent dopant contents within or near the amounts quoted by other researchers.

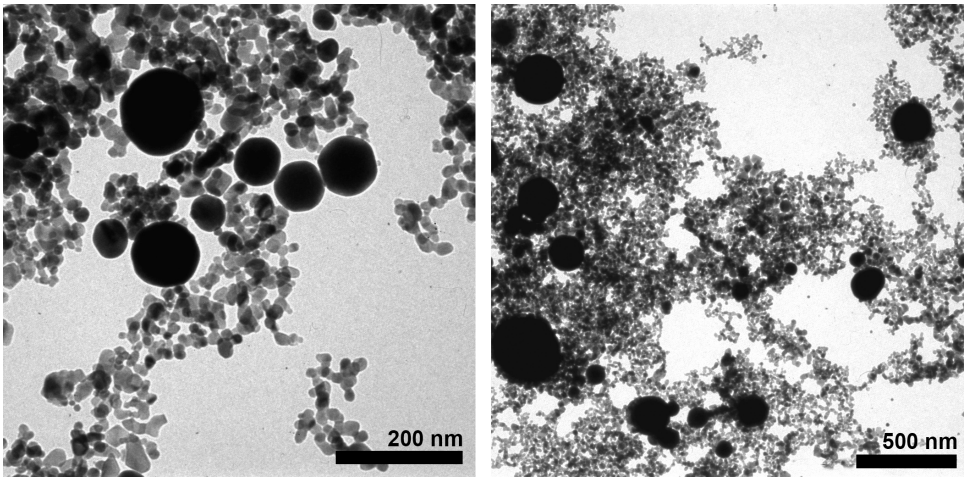

Figure 4.14: Images of gold-doped SnO_2 film deposited on TEM grids. The large and dark discrete spheres were identified as gold using XEDS.

Transmission electron microscopy was used to continue investigating the potential causes for the unusual behavior of the doped SnO_2 sensors. The dispersions were deposited on the TEM grids and dried in ambient conditions. The TEM samples did not undergo sintering process. Figure 4.14 presents TEM images of gold-doped SnO_2 films on TEM grids. The images were taken of areas where the film was thin enough to allow electron transmission. As seen in the images there was a high concentration of gold nanoparticles in local regions. The spherical gold particles observed using the TEM ranged from 50 - 300 nm in clusters of 10 - 30 discrete spherical particles at several locations on the grid. This suggests that even though the XEDS and EMPA results yielded dopant loading of 3.5 wt.% for gold, the local concentration of gold nanoparticles can be substantially higher. Such high concentrations of gold or palladium oxide, for instance, can lead to higher conductivities in local regions and thereby reduce the overall film resistance. This would also help explain the dilution experiments where doped dispersions were diluted with the undoped dispersion. The locally high concentrations would remain unaffected, while reducing the overall dopant loading, and therefore result in low film resistances observed.

4.2.2 Hybrid sensors with CS generated SnO_2

To avoid high local concentrations of dopants in tin dioxide films, alternative doping methods for combustion synthesized SnO_2 were explored. This involved using the combustion generated tin dioxide with dopant materials derived from methods other than combustion synthesis. These sensors utilized a hybrid approach to sensitize the films with dopants. This investigation focussed on gold doped sensors, since this system was well characterized in the previous work.

Using colloidal gold solution

A colloidal suspension of gold was prepared from hydrogen tetrachloroaurate ($HAlCl_4$, Sigma Aldrich) with the recipe provided by McFarland *et al.* [99]. As presented in the TEM image of the colloidal gold in Fig. 4.15, the recipe yielded approximately 15 nm diameter nanoparticles of gold with a narrow size distribution. The colloidal gold suspension was mixed with undoped SnO_2 dispersion in a 1:10 volumetric ratio. Such a mixture would have produced an approximate 0.2 wt.% of gold, based on complete conversion of $HAlCl_4$ to gold. Two experiments were performed using the dispersion-drop method to deposit two and five layers of the sensing film. Both experiments resulted in non-ideal sensor response with a low average sensitivity of 2.4 and the average time response of 18 seconds. The weak sensor performance can attributed to the same reasons discussed earlier for the combustion generated doped SnO_2 sensors (non-hybrid sensors), where high local concentrations of gold nanoparticles can result as the colloidal solution evaporates. This result is somewhat evident in the TEM image depicted in Fig. 4.15 where the gold nanoparticles clustered into a monolayer as they dried.

Using sputtered Au or Au-Pd layer

The locally clustering of metal nanoparticles is (in theory) only a concern when it happens near the electrodes. Sputtering metal dopants on SnO_2 film enables avoiding locally high concentrations of additives near the electrodes altogether. Two alternative layers of sputtered metals were considered for this study: a sputtered layer of gold and a 1:1 combination (by weight) of gold and palladium. For this study, the number of layers of SnO_2 dispersions added was an important parameter as discussed earlier. Since the performance of undoped SnO_2 sensors is unaffected

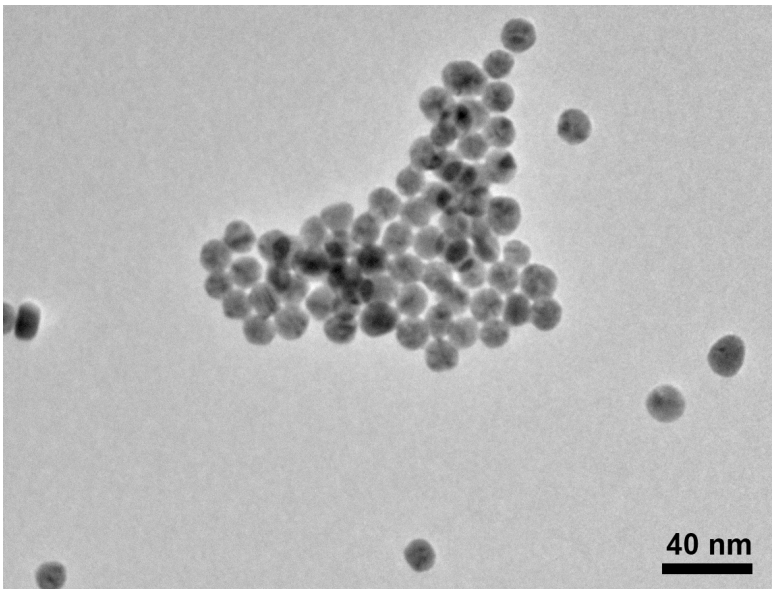

Figure 4.15: TEM image of colloidal gold nanoparticles deposited on carbon film grid. Mean particle size for the gold nanoparticles was evaluated to be 15 nm.

beyond two deposition layers (see Section 4.1.4), only two layers of SnO_2 dispersions were added before the sputtered layer was deposited.

The following process was used to prepare the sputter-doped SnO_2 sensors. The sputtered layer was deposited after two layers of SnO_2 had been deposited and dried at ambient conditions. The sputtering step was performed using two instruments with gold and gold-palladium targets with ionized argon. For both the gold and gold-palladium sputtered layer, an approximately 2 nm thick layer of metal(s) was deposited, based on the calibration provided by the manufacturer. Following the sputtering step, the sensors were annealed in the furnace at 500 ^{o}C for 1.5 hrs. The gold sputtered layer appeared golden after the sputtering step; however, the sensor transformed to a pink surface following the annealing. It is assumed that the gold sputtered film coalesced into gold nanoparticles because of the annealing step. The same observations were made on the glass slide that accompanied the sensor platform during the sputtering and the annealing process.

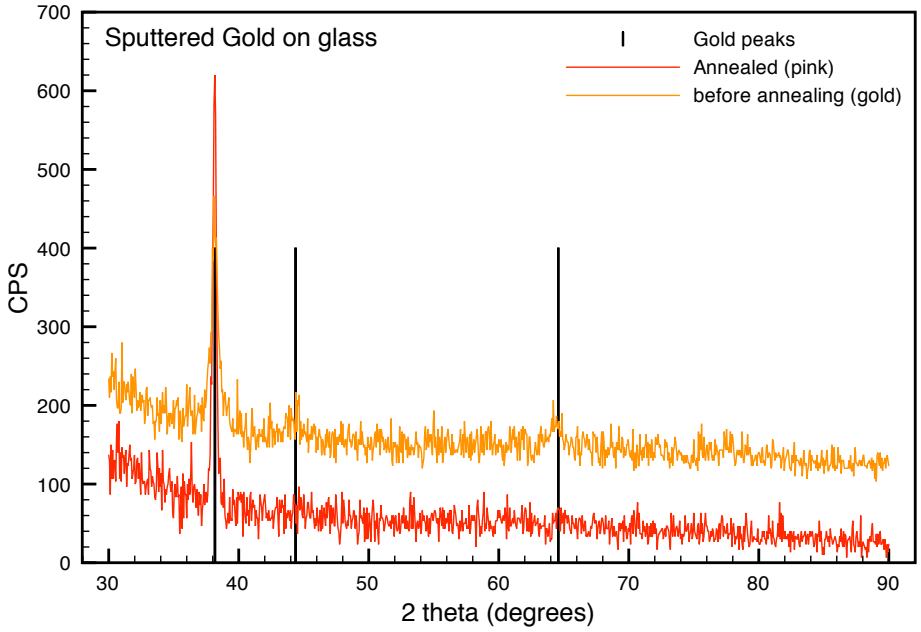

Figure 4.16: XRD spectra of sputtered gold layer on glass slide before and after the annealing step at 500 ^{o}C. Reference gold peaks (4-784) are provided to identify the dominant features.

Figure 4.16 shows XRD analysis performed on two glass slides that experienced the same processing, where one of the spectra is from before the annealing step while the other is after. As evident from the figure, the annealing step resulted into oriented structures of gold to the $\langle 111 \rangle$ feature. Figure 4.17 presents a high resolution scan of the XRD spectra with Scherrer analysis performed on the $\langle 111 \rangle$ feature of gold (shown as an inset). The average crystallite size obtained for the pink gold layer was evaluated to be 32 nm. This phenomenon was not observed for the Au-Pd sputtered layer sensor.

Figure 4.18 summarizes the sensor performance from the sputtered gold and sputtered gold-palladium layer added to the combustion synthesized SnO_2. The results from the undoped tin dioxide sensors are provided for comparison. It is clearly evident that the sputtered sensors perform better than the undoped sensors, while the gold sputtered sensor shows the greatest improvement. To provide a better perspec-

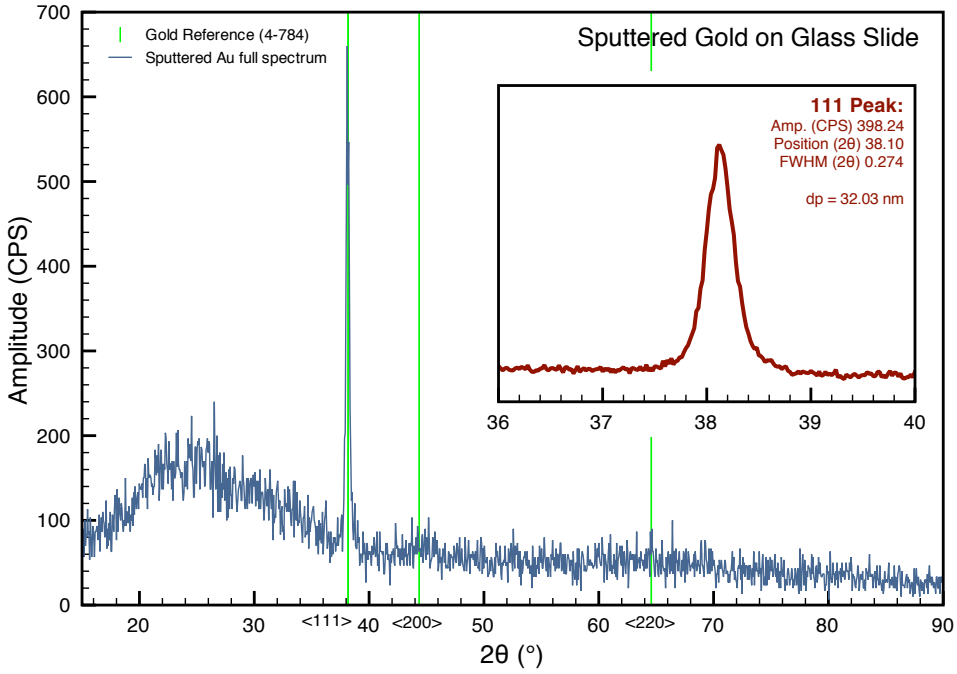

Figure 4.17: XRD of the sputtered gold film on glass slide with high resolution scan (inset) for crystallite size determination.

tive of the results obtained for the doped sensors, a commercially available tin dioxide based sensor was evaluated in the same testing facility as others with 500 ppm CO in dry air. The commercial sensor was purchased from AppliedSensors and yielded sensitivity comparable to the sputtered gold sensor with good time response. The commercial sensor was also doped; however, the dopant material is unknown. Considering the combustion synthesis tin dioxide based sensors are unoptimized; they hold considerable potential for further improving sensing applications, as evident by this comparison.

4.3 Sensor testing conclusions

The studies presented earlier in this chapter have established control over the deposition process and sensor testing procedure. Considering one of the primary goals of this study was to establish a platform for testing and as a result develop

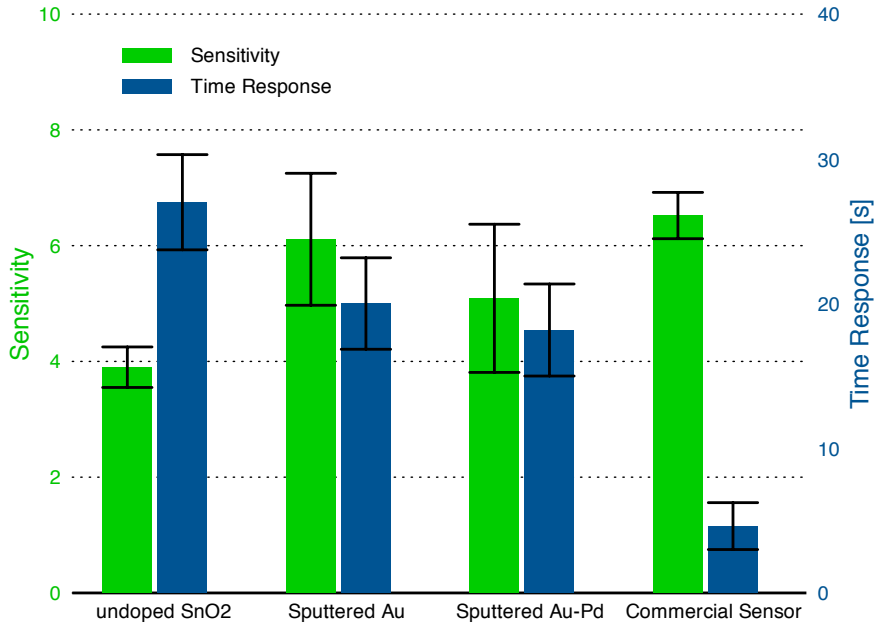

Figure 4.18: Comparison between undoped, sputtered gold- and palladium-doped SnO_2 sensor performance, along with a commercial gas sensor purchased from AppliedSensors. All the sensors were tested at an operating temperature of $\sim$ 330 ^{o}C, except for the sensor from AppliedSensors which operated at $\sim$ 270 ^{o}C.

an understanding of the microstructure and material composition links, the results clearly indicate a successful methodology for sensor testing. The deposition procedure developed avoids the use of binders to achieve competitive sensor performance results with combustion synthesized tin dioxide particles.

The doped-SnO_2 results demonstrate the importance of uniformly distributing metal and metal oxide nanoparticles in the sensing films rather than focusing on the bulk dopant loadings. For instance with the colloidal gold suspension system, unless an effort is made to uniformly disperse the gold nanoparticles in the SnO_2 film, the added advantage of using a well controlled and narrow size distribution of gold particles may not be realized. The sputtering method avoids the challenge of uniform dopant distribution by keeping the dopant materials away from directly influencing the resistance near the electrodes. As a result, the sputtered gold sensors exhibit

a noticeable improvement in sensitivity and time response over undoped sensors, as expected based on previous studies.

CHAPTER V

Conclusions and Recommendations for Future Work

This chapter provides the key conclusions reached for each research area explored during this study. Recommendations for future research directions are also provided.

5.1 Combustion synthesis

The combustion synthesis studies conducted for this project demonstrated the versatility of the nanoparticle synthesis approach for gas sensing applications and other materials applications that require metal oxide nanoparticles to be produced in large quantities with high levels of control over the microsctructural properties. The methane-assisted combustion synthesis method demonstrated in this work greatly expanded the range of control possible over SnO_2 structure (including the first flame synthesis of high-aspect ratio single crystalline structures and encapsulated morphologies), additive composition (including good integration of the additives within the SnO_2 architecture and the versatility to use a wide variety of metals as additives) and average crystallite size. The simplified modeling approach, based on the characteristic times for the physical and chemical mechanisms important in flame synthesis systems, provided a new means to interpret the experimentally observed

nanoparticle phase, structure and composition. The simplified model captures the fundamental mechanisms with sufficient accuracy, that it can be used as a coarse predictive tool.

This work also revealed the processes important during metal acetate decomposition. The results of the gold acetate thermal decomposition experiments provided the first direct imaging of the violent fragmentation that occurs. The data provided further evidence that the grain dimensions of the metal acetate particles directly translate to the size of the resulting metal additives materials. This work provides quantitative data that are critical for refining existing and developing new synthesis applications.

5.2 Gas sensing

The results of the sensor performance studies yielded many insights into the relationships between the microstructure of the active sensing materials and gas-sensing performance. To make meaningful comparisons of sensor performance as a function of microstructure and composition, it is critical to create a sensor fabrication procedure that is consistent and repeatable. The screenings studies of the types of binder and film deposition revealed that the sensor response is highly dependent on the film/electrode connectivity and the inter-particle connectivity which varied widely based on the fabrication methods used. The novel dispersion-drop method developed during the course of this work was a relatively simple and reproducible technique for establishing a testing platform for a range of SnO_2 materials. The low film resistance in reference atmosphere proved to be a relevant parameter to monitor deposition quality between films. Excellent sensor performance in terms of

sensitivity and time response was observed for undoped-SnO_2 for carbon monoxide detection at levels as low as 10 ppm.

The results of the materials characterization (XRD, TEM and XEDS) provided key indicators of sensor performance. For example, gold and palladium additives did not improve sensor performance, as was expected. However, TEM studies of the films suggested highly localized dopant particles near the electrodes adversely affected sensor performance by reducing the film resistance.

5.3 Recommendations for future work

Controlling nanocomposite morphology is a vital step toward designing new and advanced materials with controlled microarchitectures. Sensors, surface coatings, pigments, photovoltaics, optics, semiconductors, and catalysts can each benefit from targeting optimized microstructures. For example, encapsulation of metals has yielded remarkable photonic properties, and nanorod SnO_2 structures have potential to improve solar cell performance. Combustion synthesis methods offer the potential to produce such high-value per-gram materials at high rates with excellent control of the nanocomposite properties.

Areas for future work include exploring new engineering applications which can benefit from improved understanding of the microstructural/performance links, such as the examples provided above. Additionally, the area of improving gas-sensors has tremendous potential. Here, combustion synthesis methods could be used to explore optimization strategies for improving selectivity and performance in harsh conditions.

In terms of model developing, the most promising area is in the development of

new mathematical models which can be used to develop probability-based approaches to simulating particle nucleation and growth. These methods can be used to both interpret experimental data and incorporated into advanced combustion models to predict particle formation and resulting morphologies.

Metal acetates have been demonstrated as excellent precursors for metal and metal oxide additives. However, it would be useful to explore other methods for incorporating metal additives into the flame synthesis system which can be used to achieve more uniform distributions of the metals. A uniform distribution may be achieved by aerosolizing and entraining a colloidal suspension of metal nanoparticles through the secondary fuel-tube of the burner. The added advantage of using colloidal metal particles is the narrow particle size distribution which can be used to clarify our understanding of the effects of dopant particle size on material performance properties.